Title
Investigating Cancer Sialylation in Embryonic Zebrafish

Author
Yee, Nathan Alexander

Publication Date
2017

Peer reviewed|Thesis/dissertation

Investigating Cancer Sialylation in Embryonic Zebrafish

By

Nathan Alexander Yee

A dissertation submitted in partial satisfaction of the

requirements for the degree of

Doctor of Philosophy

in

Chemistry

in the

Graduate Division

of the

University of California, Berkeley

Committee in charge:

Professor Carolyn R. Bertozzi, Chair
Professor Matthew B. Francis
Professor Gerard Marriott

Spring 2017

Investigating Cancer Sialylation in Embryonic Zebrafish

By Nathan Alexander Yee

Abstract

Investigating Cancer Sialylation in Embryonic Zebrafish

by

Nathan Alexander Yee

Doctor of Philosophy in Chemistry

University of California, Berkeley

Professor Carolyn R. Bertozzi, Chair

Changes in glycosylation have been well-documented with regard to the onset and progression of cancer. Pervasive amongst these is the overexpression of cell surface sialic acid, a shared characteristic of myriad cancer types. Hypersialylation has been noted as a defining feature of the malignant phenotype, playing numerous functional roles in promoting cancer cell survival and invasivity, and a great body of research has sought to unravel its multifaceted contributions to metastatic advancement.

A complete understanding of the impact elevated sialic acid has on cancer progression has been hindered by a lack of tools for its direct study. Glycan biosynthesis is not genomically encoded, disqualifying commonplace molecular biology techniques such as mutagenesis and fluorescent protein fusions. This has motivated the development of novel chemical approaches to fill this void. In particular, bioorthogonal chemical methods have accomplished the direct tagging and imaging of sialylated glycans, enabling precise tracking within complex cellular milleu. As an additional challenge, the cancer disease state comprises intimate interactions between tumor and host cells; a comprehensive grasp of sialic acid's involvement in cancer must be obtained through the use of animal models to recapture the physiological environment. Current *in vivo* models, primarily mice, are severely limited in their ability to observe cancer behavior at the cellular scale. An alternative model, the embryonic zebrafish, surmounts this barrier and permits the real-time detailed observation of cancer cell dynamics *in vivo*. Utilization of the zebrafish model's imaging capabilities may deepen our mechanistic understanding of sialic acid's role in cancer. The work presented in this dissertation constitutes efforts to study cancer sialylation in zebrafish using bioorthogonal chemistry and other approaches.

The first chapter reviews advancements made in the field of *in vivo* bioorthogonal cancer labeling. Recent years have seen the emergence of varied approaches to target cancer in mouse models for imaging and therapy, using both metabolic incorporation and antibody-pretargeting strategies. This survey of the literature highlights the potential for continually evolving bioorthogonal

technology to play a role in human health, and also illuminates the challenges associated with bioorthogonal chemistry-based approaches within mice, creating a framework for discussion of bioorthogonal labeling as applied to a zebrafish model of cancer.

Chapter 2 describes the development of methods for the bioorthogonal labeling of cancer-associated sialic acid in a zebrafish xenograft model. Through the use of metabolic incorporation of modified sialic acid precursors and two widely popular bioorthogonal reactions, copper-free click chemistry and the tetrazine ligation, selective labeling of the cancer cell surface was achieved with greater sensitivity and spatial resolution than has been demonstrated in mouse tumor models. These efforts lay groundwork for the application of bioorthogonal chemistry to monitor sialic acid distribution on the subcellular scale in zebrafish throughout different stages of cancer progression.

Chapter 3 investigates the interplay between cancer cells and the innate immune system in zebrafish. Sialic acid-mediated interactions between cancer and immune cells have been observed previously and their biochemical basis is beginning to be understood. How these interactions impact the behavior of cancer and immune cells *in vivo* is an ongoing area of research. Embryonic zebrafish are a powerful tool in this regard, as they enable the facile monitoring of cancer and immune cell dynamics through real-time imaging. Through sialidase-treatment of cancer xenografts, we examined the role sialic acid plays in cancer cell survival and recruitment of macrophages and neutrophils. Sialic acid was found to have a significant influence on these processes, the mechanisms of which are currently being deciphered.

Finally, Chapter 4 represents an excursion outside the realm of zebrafish cancer biology. Genetically encodable self-labeling protein tags are an invaluable tool for protein imaging, and offer greater temporal control over traditional fluorescent protein tags. However, their large size, often in excess of 20 kDa, can interfere with native interactions. Described herein is a 10 kDa riboflavin-binding protein rationally engineered from riboflavin synthase. This protein undergoes a self-labeling reaction with novel acrylamide-modified flavin fluorophores, creating a covalently bound fluorescent protein tag. Preliminary results indicate that this system is suitable for labeling within cellular environments with a potential application as a small, genetically encodable tag for fluorescence anisotropy measurements of protein hydrodynamics.

This dissertation is dedicated to my family.

Table of Contents

Chapter 2. Bioorthogonal Imaging of Cancer-Associated Sialic Acid in Embryonic Zebrafish

Chapter 3. Elucidating the Role of Sialic Acid in Cancer Cell Survival in a Zebrafish Model

Chapter 4. An Engineered Riboflavin-binding Protein for Self-labeling with Acrylamidoflavin Fluorophores

List of Figures

List of Schemes

List of Tables

Acknowledgements

Graduate school has been a period of momentous personal and professional growth for me, and also one of the greatest challenges I've faced. Doubtless, I could not have made it through this experience without the help of many people, and I am enormously grateful for their guidance and support.

First, I thank my advisor, Carolyn Bertozzi. Without her support, this dissertation would not have been possible. Her contagious enthusiasm and skillfulness as a communicator have been sources of inspiration ever since our first meeting. Working in the environment of independence she has fostered has been a singular learning experience that has helped me to develop immensely has a scientist.

I've been fortunate to work alongside wonderful colleagues whose contributions to my life I won't soon forget. Anthony Baldridge has been a fantastic friend and collaborator. His mentorship was vital to my graduate career and I grew tremendously as a person through our friendship. Brendan Beahm, where do I start? Thank you for imparting your vast zebrafish knowledge, and all the extracurriculars that came with it. I appreciate you keeping the lab perpetually off the rails. Lissette Andrés has been a close friend and confidant, and I'm very grateful for our conversations about science and life, which were essential for my sanity. Marjoke Debets was always happy to share her insight whenever I was unsure about science, careers, etc. Thanks for that and all the fun chats we had in Latimer 805. CJ Cambier's generosity with his wealth of expertise has been invaluable. Throughout my career, I will continue to aspire to his standard of scientific excellence. I thank Steve Canham, Sloan Siegrist, Chelsea Gordon, Gaby de Almeida, and Pam Thompson for their advice on all things grad school.

Elliot Woods, Neil Rumachik, Fred Tomlin, Justin Kim, and Yisu Han have been delightful friends and coworkers. The laughs we shared made working in lab so much more tolerable. Zach Smith is one of the funniest individuals I've met, and I learned a lot from working together. To Zach and Arjun Aditham, thank you for so many memorable conversations! I thank Sam Keyser for her much appreciated sarcasm and always helpful scientific feedback. Alex Hoepker, thank you for the opportunity to work on a challenging yet stimulating collaborative project and for showing me great food places in Berkeley. My podmates, Rachel Willand-Charnley, Junwon Choi, and Ulla Gerling-Driessen, have been amazing company and I can't imagine a better group to have shared a pod with. I will forever cherish our countless and hilarious discussions.

I owe a huge amount of gratitude to the entire support staff. Meridee Mannino and Sia Kruschke keep the lab running, and I've been very privileged to have their help at the ready. Thank you, Maryann Koopman, for always providing the lab with delicious baked goods. Olga Martinez has been a dear friend and her assistance and propensity to go above and beyond were instrumental to my time at Berkeley. Asia Avelino has always had my back in traversing various perils of the graduate experience; I cannot thank her enough for her help and friendship.

Next, I acknowledge my classmates, Mason Appel, Ioannis Mountziaris, Frances Rodríguez-Rivera, and David Spiciarich, who have been my closest friends and staunch supporters throughout this journey. I credit them for the most enjoyable moments I had in grad school. I am eternally grateful for their uncompromising encouragement and friendship, and it's been an honor to go through grad school with them.

I am immeasurably thankful to my family for their care and support that has sustained me for the past five and a half years. Thanks especially to my parents, Teresa and Jim; my brother, Nicky; my grandma, Nying Nying; my stepdad, Mike; Brandon, Stacey, Holly, Nichole, Michael, Lisa and Chas, Joey and Jessica, and my niece and nephews for giving me a much needed escape whenever I visited home. Thank you also, Nicky and Vivian, for your greatly appreciated visits to me in the Bay Area. I thank the Keo family for their encouragement and endless positivity. A special thanks to Teddy, Frosti, and Casey for their unmatched companionship and cheering me up whenever I needed it.

Finally and foremostly, I must express my deep gratitude to my girlfriend, Soka Keo. She has been my strongest supporter through the highs and lows of grad school, and her unrelenting love and encouragement have pushed me to become a better scientist and person. Our relationship has taught me more than grad school ever could, and I'm excited for our next adventure!

Chapter 1

Targeting Cancer *In Vivo* Using Bioorthogonal Chemistry

Chapter 1. Targeting Cancer *In Vivo* Using Bioorthogonal Chemistry

Introduction

The field of bioorthogonal chemistry is primarily focused on the development of chemical ligation reactions that proceed selectively and efficiently under physiologically relevant conditions. The ever-expanding catalog of bioorthogonal reactions represents a dynamic arsenal of chemical tools that have been used to investigate biological systems not readily amenable to well-established genetic strategies, e.g., non-genetically encoded biomolecules such as lipids and glycans. In a typical bioorthogonal labeling experiment, a reactive chemical reporter group is first incorporated into a given biomolecule using a variety of methods. A secondary step involving a covalent ligation between the reporter and a complementarily reactive functional group equipped with a probe or other molecular cargo, enables the imaging, enrichment, or manipulation of the biomolecule of interest (Figure 1.1). Bioorthogonal reactive partners are chosen to fulfill a number of chemical criteria, including stability and inertness to endogenous biological functionalities, being non-perturbative to the system under study, and ideally possessing fast reaction kinetics such that low concentrations of reagents can be used.

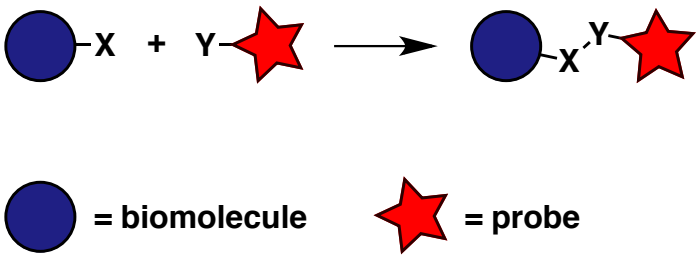

Figure 1.1. Bioorthogonal reaction between functional groups X and Y.

The pinnacle of bioorthogonality is often a reaction's utility within a living organism. To date, a number of different research groups have implemented bioorthogonal reactions for use in live animals. In particular, there has been special attention to using bioorthogonal approaches to the imaging of cancer in mouse tumor models using two predominant strategies to introduce a chemical reporter. Metabolic oligosaccharide engineering has enabled the incorporation of unnatural azide-containing sugars onto the cancer cell surface, allowing for the labeling of modified sialic acid residues on tumors through the use of azide-reactive chemical probes. Due to the prevalence of sialic acid overexpression in many different cancer types,[1] tools to assay tumor sialylation *in vivo* may deepen the understanding of its role in cancer progression. An alternative is a pretargeted approach using cancer epitope-specific antibodies armed with a reactive handle. Secondary reaction with a small molecule bioorthogonal probe

can overcome the unfavorable pharmacokinetic properties of antibodies alone (long serum half-life resulting in high levels of background), with such methods accomplishing the robust targeting of tumors *in vivo* through the delivery of imaging probes and therapeutic agents. The clinical relevance of antibody-based pharmaceuticals in concert with the continual development of increasingly efficient bioorthogonal reactions carries exciting implications for cancer diagnosis and therapy.

Along with the rapid evolution of bioorthogonal technology in recent years has emerged a wealth of unique approaches for labeling targets *in vivo*. This chapter chronicles the application of bioorthogonal chemistry in live animal models, with a specific focus on its use to image cancer in mice. Early work employing metabolic engineering of azidosugars to label tumors was hindered by poor reaction kinetics and probe pharmacokinetic qualities, necessitating the development of creative solutions to achieve selective labeling *in vivo*. Pretargeted labeling, based on its compatibility with the exceptionally fast tetrazine ligation, has experienced comparatively greater success in the selectivity of labeling and the scope of imaging probes utilized. In addition to the ongoing optimization of existing tumor imaging methods, current efforts involve the use of bioorthogonal chemistry for drug delivery, with many studies showing therapeutic efficacy in mouse tumor models.

Prevalent Bioorthogonal Reactions for Labeling in Live Animals

Staudinger Ligation

One of the earliest developed bioorthogonal reactions, the Staudinger ligation occurs between an organic azide and a triaryl phosphine to form a stable amide linkage via attack by an aza-ylide intermediate on an intramolecular ester trap (Figure 1.2).[2]

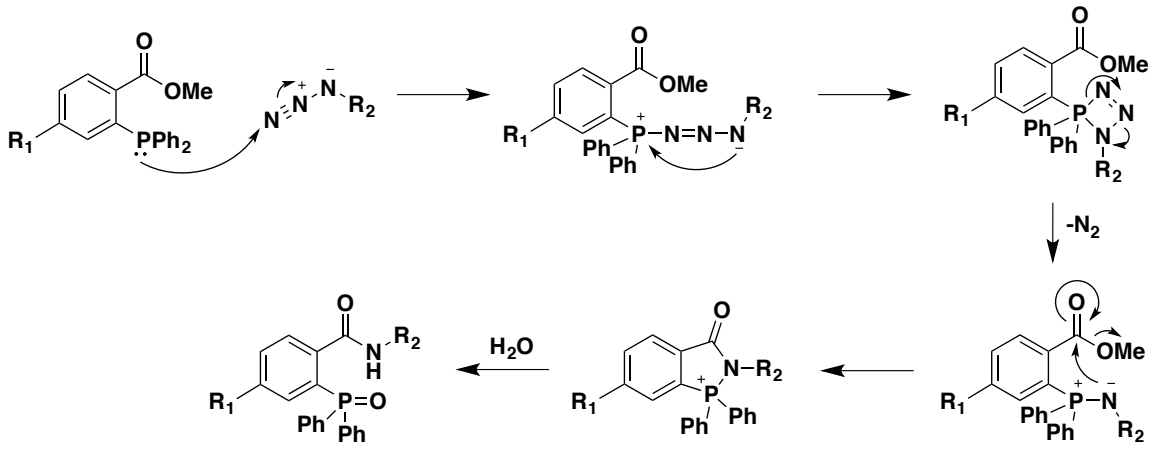

Figure 1.2. Mechanism of the Staudinger Ligation.

The Staudinger ligation was the first showcase of the azide as a bioorthogonal chemical reporter, which, due to its abiotic nature and small size, readily lends itself to facile incorporation into a variety of biomolecules. Unfortunately, the sluggish kinetics of the reaction (second order rate constant $k = 2 \times 10^{-3}$ M^{-1} s^{-1})[3] compared to subsequent generation bioorthogonal reactions hampered its performance in complex *in vivo* systems. Nonetheless, there are instances reported of the Staudinger ligation's use in animals.[4–6]

Azide-Alkyne Cycloadditions

Aside from their reactivity toward phosphines, azides also undergo 1,3-dipolar cycloadditions with alkynyl dipolarophiles for the rapid formation of triazoles (Figure 1.3).[7] The prototypical reaction involving a terminal alkyne requires the addition of a copper(I) catalyst (copper-catalyzed click reaction) to proceed appreciably at room temperature. Copper(I) cytotoxicity has generally relegated the copper-catalyzed click reaction to labeling of fixed cells, although the advent of biocompatible ligands to reduce toxicity has expanded its biological scope.[8–10] Still, the requisite for copper-chelating ligands as well as exogenous reducing agents to maintain the catalytically active copper(I) oxidation state complicates its use in live animals.

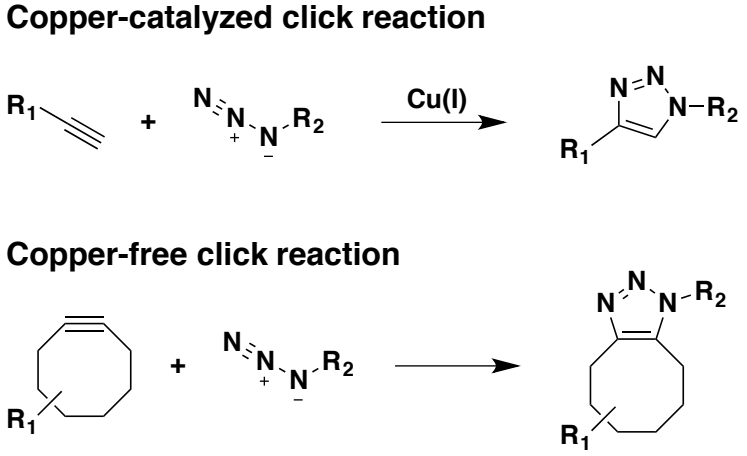

Figure 1.3. Azide-alkyne cycloadditions in bioorthogonal chemistry.

The introduction of ring strain can accelerate the rate of the azide-alkyne cycloaddition, obviating the need for a copper(I) catalyst. Bertozzi and coworkers accomplished this by constraining the alkyne in an eight-membered ring system.[11] Cyclooctynes undergo spontaneous reaction with azides to form triazoles in a reaction termed copper-free click chemistry. Since the initial discovery, numerous groups have increased the reactivity of cyclooalkynes

through electronic perturbation or the installation of additional strain, with second order rate constants spanning the gamut from 10^{-3} to 10^{0} M^{-1} s^{-1} (Figure 1.4).[12–20] As a result of this vast rate enhancement over the Staudinger ligation, cyclooctyne probes have seen widespread use for labeling azidosugars in live animals and tumor models, although poor pharmacokinetics and cross-reactivity with thiol nucleophiles limits their selectivity.[4,21]

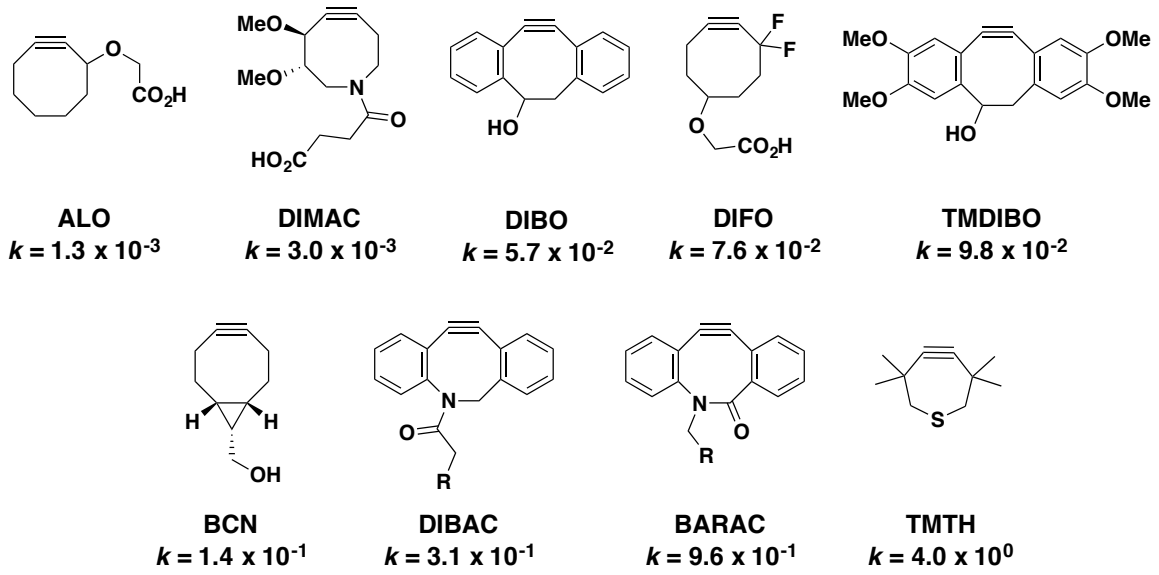

Figure 1.4. Reactivity of strained alkynes for copper-free click chemistry. Second-order rate constants for reaction with benzyl azide reported in units of M^{-1} s^{-1} and measured in acetonitrile. DIBO and DIBAC measured in methanol. BCN measured in 3:1 acetonitrile:water. TMDIBO measured in chloroform.

Tetrazine Ligation

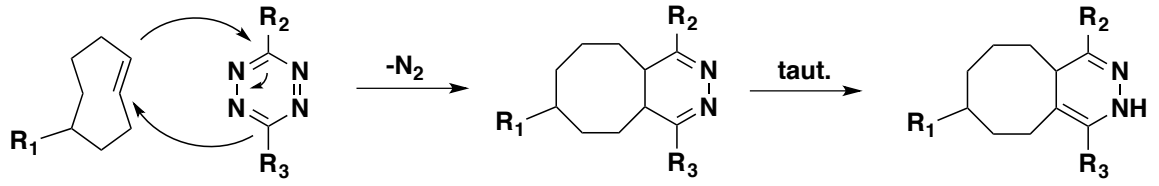

Figure 1.5. Mechanism of the tetrazine ligation with *trans*-cyclooctene.

The tetrazine ligation is an inverse electron-demand Diels-Alder reaction between a 1,2,4,5-tetrazine and a strained dienophile (Figure 1.5).[22] The tetrazine ligation is noteworthy because of its extraordinarily fast reaction rate compared to other commonly used bioorthogonal reactions, with the second

order rate constant for the reaction between tetrazines and *trans*-cyclooctenes (TCO) ranging from 10^2 to 10^6 M^{-1} s^{-1} depending on tetrazine and TCO substitution, with the fastest practically usable species falling in the 10^3 to 10^4 range.[23] As well, tetrazines undergo ligation with a number of other strained dienophiles, albeit at lower reaction rates. A potential hindrance to the reaction's usefulness *in vivo* is the inherent instability of both tetrazines (due to hydrolysis) and *trans*-cyclooctenes (due to metalloenzyme-mediated isomerization to the less reactive *cis* configuration)[24] within the physiological environment. Despite these drawbacks, the tetrazine ligation has been utilized for the successful high contrast imaging of tumors in mice, particularly in pretargeted methods featuring TCO-modified antibodies.

Metabolic Engineering of Tumors *In Vivo*

Metabolic Incorporation of Unnatural Sugars in Animals

The cell surface is decorated with polymers of sugars, termed glycans, which play vital roles in modulating extracellular recognition and cell membrane physical properties. Glycan identity and expression levels are known to fluctuate throughout organism development and cancer progression, motivating the advancement of tools to monitor changes in glycosylation. A prevalent chemical technique to study cell surface glycosylation *in vivo* has been metabolic oligosaccharide engineering, which takes advantage of the glycan biosynthetic machinery's tolerance for small structural perturbations to sugar starting materials, allowing for the incorporation of sugars bearing reactive chemical handles into glycans and subsequent labeling using bioorthogonal probes. Animal models have served as a testing ground for this strategy, with bioorthogonal reactions successfully labeling glycans in live organisms from worms to mice.

Seminal work by Laughlin et al. demonstrating the metabolic labeling of glycans *in vivo* utilized an embryonic zebrafish model.[25] It was shown that, as with cells in culture, zebrafish embryos will take up peracetylated *N*-azidoacetylgalactosamine (Ac_4GalNAz) added to their media and incorporate this unnatural sugar into cell surface glycans. Subsequent reaction with a fluorophore-conjugated difluorinated cyclooctyne (DIFO) probe effected the fluorescent labeling and tracking of GalNAz residues on the zebrafish enveloping layer in a time-resolved fashion. Follow up studies involving microinjection of various azidosugar analogs into embryos at the one-cell stage of development enabled the incorporation and imaging of GalNAz, FucAz, ManNAz, and XylAz in a similar manner (Figure 1.6).[26–29] Agarwal et al. expanded this approach with the synthesis of a bicyclononyne (BCN)-modified sialic acid, which, in combination with a tetrazine fluorescence turn-on probe reported by Devaraj et al.[30] injected intravenously (IV), accomplished the labeling and imaging of internal glycans, a feat previously unrealized due to high background resulting from the slow clearance rate of systemically administered fluorescent probes.[31]

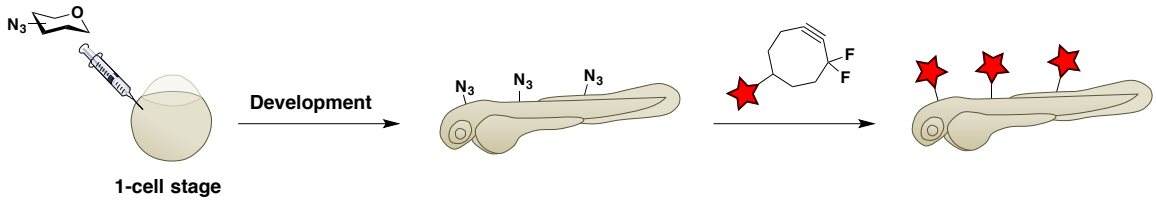

Figure 1.6. Microinjection of azidosugars for copper-free click labeling of zebrafish embryos.

The copper-catalyzed click reaction has also been used to label glycans in zebrafish. In an effort to render the copper(I) catalyst less toxic, Wu and coworkers screened a library of analogs of tris(benzyltriazolylmethyl)amine (TBTA), a common ligand for copper-catalyzed click chemistry, for their rate enhancement properties and observed that a water-soluble bis(*tert*-butyltriazolyl)ethanesulfonic acid (BTTES) variant dramatically accelerated the reaction.[8] Copper-catalyzed click labeling with BTTES exhibited significantly less toxicity than copper(I) alone on cells in culture, leading to its use for the labeling of the alkynyl sugar analog GDP-FucAl with an azidofluorophore in embryonic zebrafish. They further applied this system to image LacNAc residues in zebrafish using an engineered fucosyltransferase that, when administered exogenously, generates alkynyl LacNAc from GDP-FucAl.[9] Modifications to the structure of the azide proved fruitful as well – an electron-donating picolyl azide boosted the reaction kinetics by an order of magnitude, allowing for the imaging of zebrafish as early as the two-cell stage, albeit on fixed embryos.[10]

The nematode *Caenorhabditis elegans* has also served as a platform for metabolic bioorthogonal labeling. Laughlin et al. tested mixed-stage *C. elegans* for their uptake of Ac_4GlcNAz, Ac_4GalNAz, and Ac_4ManNAz and found robust incorporation of GalNAz into the glycome.[32] Treatment with DIFO-fluorophore yielded azide-dependent labeling in larval to adult hermaphrodite and male worms. Recently, copper-catalyzed click chemistry has been employed to tag GalNAl in *C. elegans* using “all-in one” azides, in which the azido group is directly linked to a copper-chelating motif, resulting in proximity-based rate enhancement.[33]

Zebrafish and nematodes aside, a necessary benchmark toward the use of metabolic bioorthogonal labeling for tumor imaging was to first establish its use in mice, as mice continue to be the most widely used animal model for human cancers. Chang et al. sought to apply metabolic bioorthogonal labeling tactics within mice.[34] Ac_4ManNAl or Ac_4ManNAz (analogs of ManNAc, the metabolic precursor to sialic acid) were injected intraperitoneally (IP) daily for seven days. Copper-catalyzed click chemistry with an azide- or alkyne-biotin probe, respectively, performed on harvested organ lysates allowed for the assessment of unnatural sugar incorporation via anti-biotin Western blot. Indeed, it was found that both sugars are incorporated into various organs in mice, particularly the

spleen, intestines, thymus and heart, with the alkynyl derivative showing more robust expression.

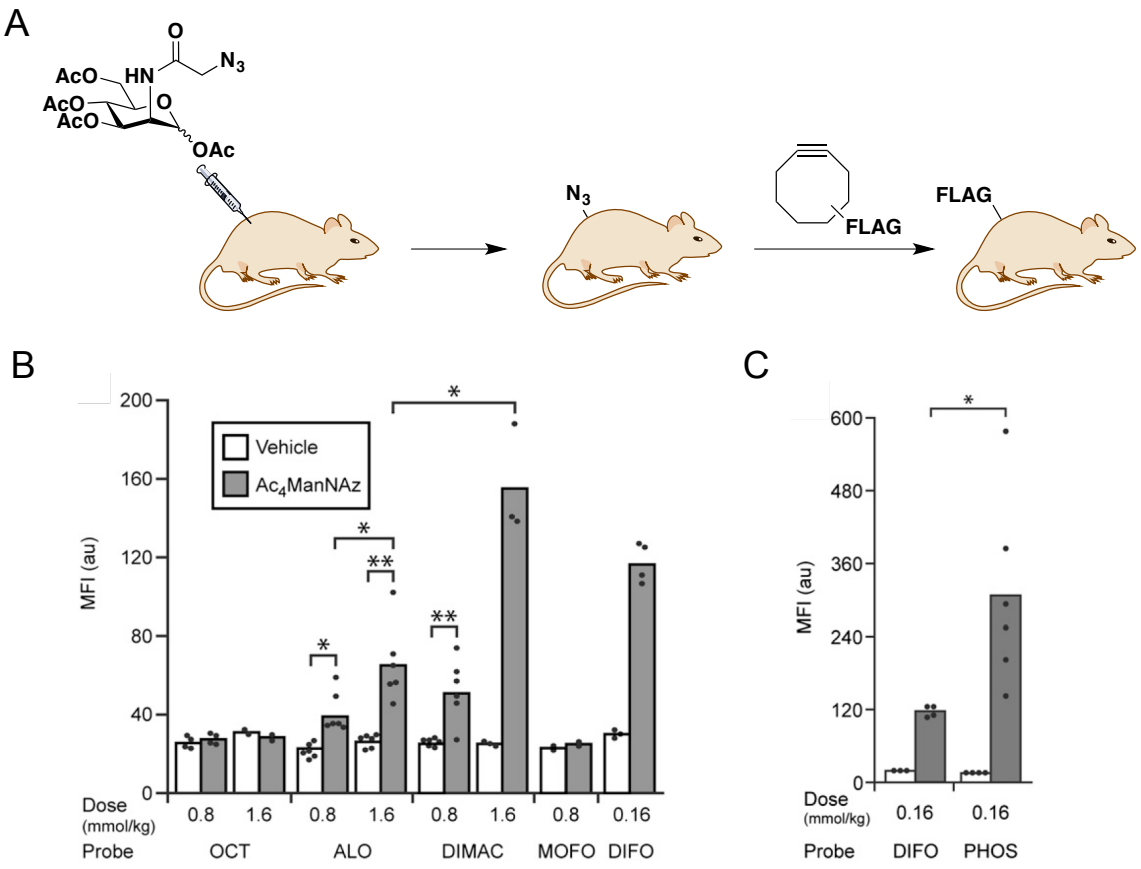

Figure 1.7. Copper-free click chemistry and Staudinger ligation in mice. A) Mice were administered (IP) $Ac_4ManNAz$ for 7 d, followed by IP injection of azide-reactive probe bearing FLAG tag of *ex vivo* analysis. B) *In vivo* labeling with a panel of cyclooctyne probes. C) *In vivo* comparison of the fastest reacting cyclooctyne tested, DIFO, with the Staudinger ligation. Labeling was quantified by treatment of harvested splenocytes with FITC-anti-FLAG and flow cytometry. Figure 1.7B-C adapted with permission from reference (4).

A follow-up study focused on conducting the bioorthogonal reaction step within the live mouse itself. After incorporation of ManNAz as before, mice were injected IP with FLAG peptide conjugates of a panel of azide-reactive probes (Figure 1.7A).[4] Treatment of homogenized mouse splenocytes with anti-FLAG-FITC and analysis by flow cytometry allowed for the quantitation of labeling (Figure 1.7B). It was observed that DIMAC, despite its slower intrinsic reaction kinetics and lower labeling efficiency *in vitro* compared to DIFO, nonetheless outperformed DIFO within the mouse. This was attributed to the increased water solubility of DIMAC imbuing it with more favorable pharmacokinetic properties.

Intriguingly, the triarylphosphine probe also exhibited better labeling than DIFO *in vivo* (Figure 1.7C). It was soon found through immunoprecipitation experiments that DIFO binds strongly to mouse serum albumin, which likely diminishes its bioavailability and labeling potency relative to other probes. Although the analysis was carried out *ex vivo*, this preliminary study established proof-of-concept for metabolic bioorthogonal labeling in a live mammalian organism and highlights the importance of pharmacokinetics for effectiveness *in vivo*.

Metabolic Bioorthogonal Labeling of Tumors

Metabolic labeling of tumors in mice has focused on the targeting of sialic acid, primarily through the incorporation of *N*-azidoacetylmannosamine (ManNAz), which is metabolized to cell surface azidosialic acid residues (Figure 1.8). Brindle and coworkers adopted this strategy in an LL2 murine Lewis lung carcinoma subcutaneous xenograft tumor model.[5] Following Ac_4ManNAz incorporation (IP injection daily for 7 days), IP-injected phos-biotin was used for Staudinger ligation labeling. IV injection of a tertiary probe, a NeutrAvidin-fluorophore, allowed for the assessment of tumor-specific labeling. Whole animal fluorescence imaging revealed a very modest increase in the tumor/healthy tissue ratio of ~1.4-fold for ManNAz-treated mice relative to vehicle only controls. This was consistent with *ex vivo* analysis which yielded only slightly elevated signals. Parallel experiments using a NeutrAvidin-[^{111}In] probe for SPECT/CT imaging produced similar results. This initial study was promising for the application of the metabolic approach for tumor imaging, although the level of contrast attained was well below the threshold for clinical relevance. The authors surmise that this may be caused by azide-independent accumulation of NeutrAvidin in the tumor via the enhanced permeability and retention (EPR) effect.

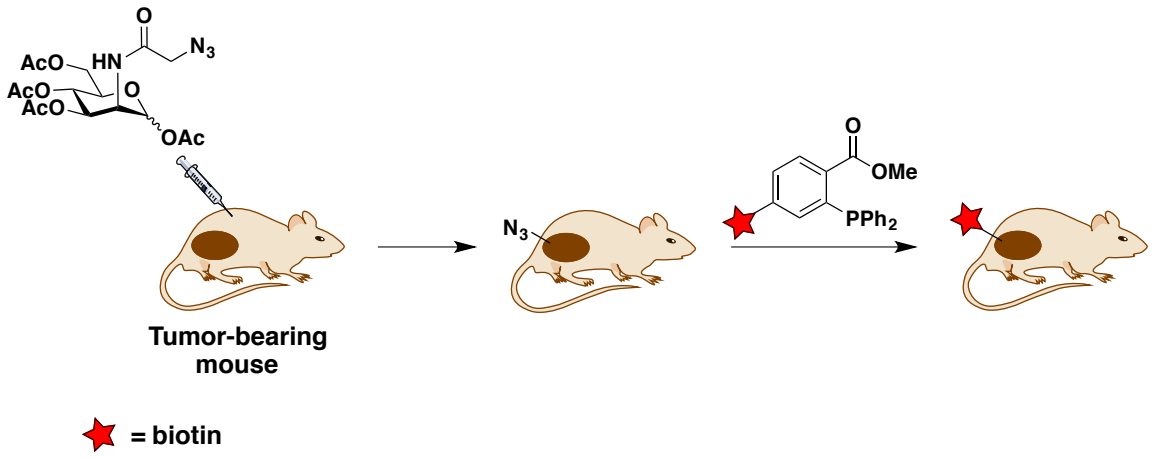

Figure 1.8. Metabolic bioorthogonal labeling of tumors in mice using the Staudinger Ligation.

These results were recapitulated through use of a “double click” design in an effort to surmount previously observed limitations.[35] Tumor-bearing mice treated with Ac_4GalNAz were reacted with bivalent conjugates of TMDIBO-TCO or phos-TCO. This allowed for a clearance period to eliminate unreacted probe prior to administration of a tetrazine-near-infrared (NIR) dye, which was expected to have intrinsically lower background signal thanks to its fast reaction kinetics. This hybrid metabolic labeling/pretargeted approach resulted in azide-specific tumor labeling of 1.4-fold for phos, as before, and 2-fold for TMDIBO, as determined *in vivo*. This enhancement of the copper-free click reaction over the Staudinger ligation was likely due to TMDIBO’s superior water-solubility and kinetics over phos. Direct reaction with TMDIBO- and phos-imaging probes did not produce significant labeling in live mice, although it was demonstrated later that tumor-specific signal could be detected *ex vivo*.[36]

A potential pitfall in using hydrophobic small molecules such as cyclooctynes and phosphines within mammalian systems is that their short serum half-lives are not properly synced to their slow reaction kinetics, the result being clearance and excretion of the probe before the ligation has time to occur. Several studies have tackled this barrier through the use of nanoparticles, which due to their large size have increased serum residence times that may be more suitable for slow-to-react probes. Additionally, nanoparticles and macromolecules have been observed to home to solid tumors by the EPR effect, whereby large particles accumulate in tumor tissue because of alterations to the normal vasculature. This could increase the local concentration of reactive probe within the tumor and lead to greater labeling efficiency, although it has been noted that clinical cancers exhibit EPR less consistently than subcutaneous mouse tumor models.[37]

Kim and coworkers attempted to take advantage of these properties through the production of liposomal nanoparticles armed with DIBAC reactive handles and Cy5 NIR dyes (Figure 1.9).[38] Subcutaneous tumors in mice were directly loaded with azidosugar through injection of a high concentration of Ac_4ManNAz intratumorally. DIBAC-liposomes delivered IV preferentially accumulated at the site of the azidosugar-injected tumor with over tumors on the opposing flank that were injected with vehicle alone. Fluorescence imaging of both live mice and excised tumors showed a 2-fold increase over the control. This represented an improvement over non-liposomal DIBAC-Cy5, which showed no discernible tumor labeling *in vivo* or *ex vivo* in the same study, but was still insufficient from a clinical perspective.

Efforts to improve their system involved the use of Ac_4ManNAz-loaded glycolyl chitosan nanoparticles (CNPs) to deliver azidosugars to tumors via EPR, as opposed to direct injection.[39] Following four daily doses of Ac_4ManNAz-CNPs, an imaging probe consisting of CNPs carrying a Cy5 payload and surface-modified with BCN was given. As before, the nanoparticle probe showed accumulation within the tumor, with *ex vivo* measurements revealing a 1.5-2-fold increase over the control. Despite this meager labeling, BCN-CNPs were applied for the tumor delivery of a photosensitizing agent for photodynamic therapy. These studies suggest that bioorthogonal labeling based on EPR effects may be

ineffectual at increasing imaging contrast in tumors, likely to due high degrees of nonspecific accumulation.

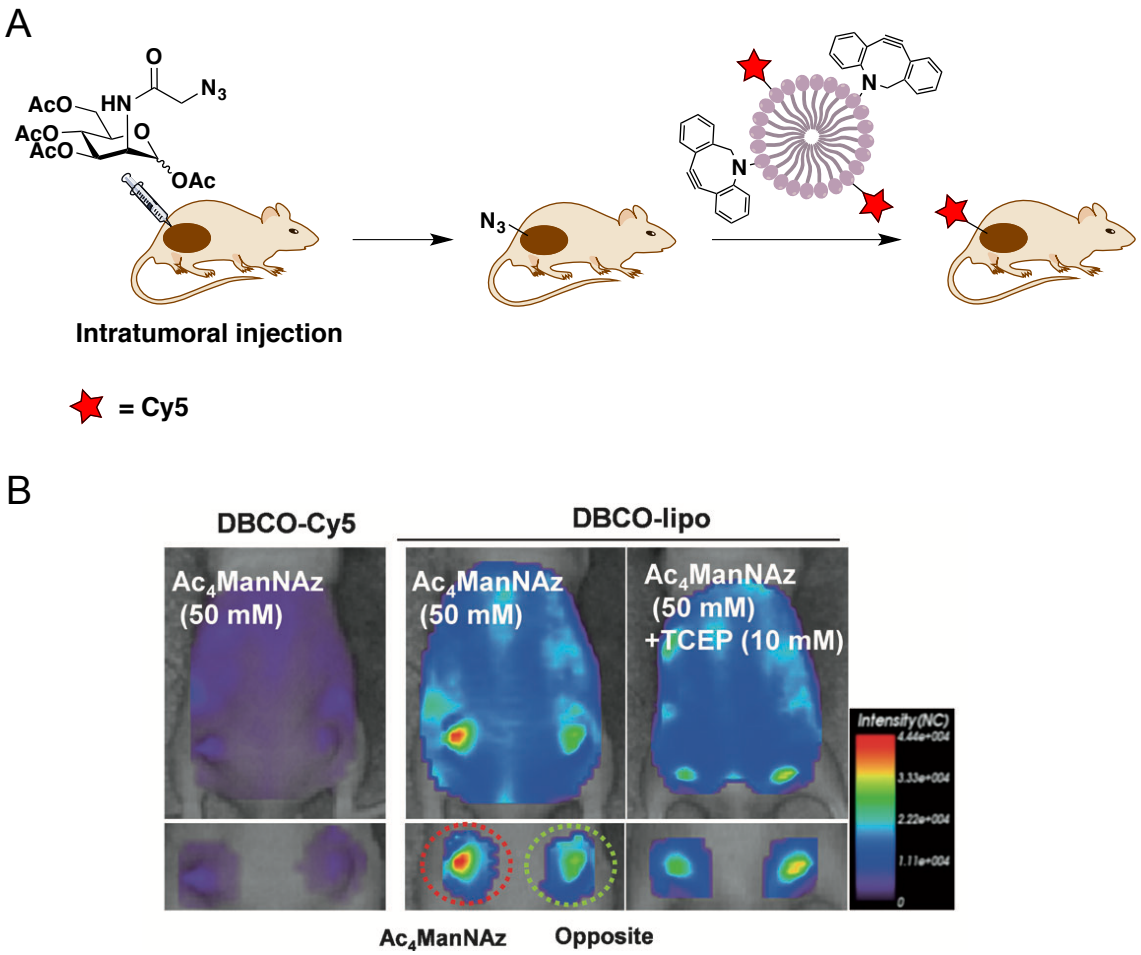

Figure 1.9. Labeling mouse tumors using DIBAC-modified liposomes. A) Azidosugar is injected directly into the tumor followed by IV injection of fluorescent DIBAC-modified liposomes. B) Fluorescence images obtained using DIBAC (DBCO)-Cy5 or DIBAC-liposomes, and after TCEP reduction of azides, compared to opposite flank vehicle control tumor. Figure 1.9B adapted with permission from reference (38), copyright 2012 WILEY-VCH Verlag GmbH & Co. KGaA, Weinheim.

In a similar vein to Kim, Xie et al. also utilized nanoparticles for azidosugar delivery, this time in mice bearing B16-F10 murine melanoma subcutaneous xenografts.[40] Rather than relying on EPR alone, they synthesized liposomes displaying a cyclic RGD-containing peptide for targeting to integrin $\alpha_v\beta_3$, which is overexpressed on the surface of B16-F10 cells. The cRGD-liposomes were used to deliver encapsulated 9-azidosialic acid to tumors through daily IV injection for

7 days (Figure 1.10A). In stark contrast to previous studies using small molecule cyclooctynes, significant labeling was observed after IV injection of a DIBAC-Cy5 probe – B16-F10 tumors labeled with 6-fold intensity over an opposite flank negative control tumor of MCF-7, which does not express integrin $\alpha_v\beta_3$ (Figure 1.10B). This significant *in vivo* labeling improvement over prior attempts may be testament to a greater efficiency of azidosugar incorporation resulting from a targeted delivery method, although it is worth noting that the nanoparticle delivery was accompanied by high systemic background. The tumor labeling enhancement was found to be strictly dependent on cRGD targeting rather than EPR, with cRGD-lacking liposomes carrying 9-azidosialic acid showing no enhancement over the free sugar alone. This method allowed for the enrichment of cancer-associated sialylated peptides through *ex vivo* reaction of azidosugar-labeled tumors with alkyne-biotin, enabling glycoproteomic profiling at different timepoints throughout tumor growth and progression.

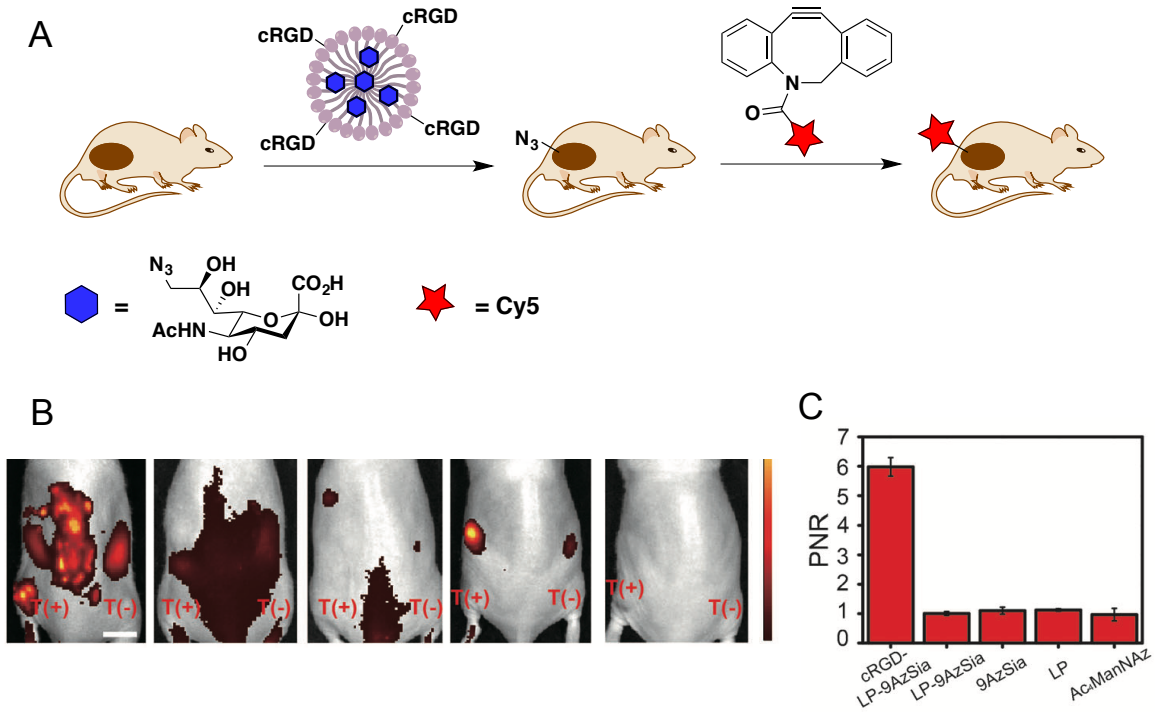

Figure 1.10. Targeted delivery of azidosugars to cancer *in vivo*.
A) Encapsulated 9-azidosialic acid (9-AzSia) is delivered to tumors by tumor targeting cRGD-modified liposomes, enabling copper-free click labeling. B) Fluorescence images of mice injected with (left to right): , cRGD-liposomal 9-AzSia, untargeted liposomal 9-AzSia, 9-AzSia, Ac_4ManNAz, and liposomes. C) Fluorescence intensity ratio of positive tumor to opposite flank negative control tumor (integrin $\alpha_v\beta_3$ deficient) for each species injected. Figure 1.10B-C adapted with permission from reference (40), copyright 2014 WILEY-VCH Verlag GmbH & Co. KGaA, Weinheim.

In summary, various modes of azidosugar incorporation and bioorthogonal probe administration have been utilized for the metabolic labeling of tumors in mice. Most strategies to augment imaging contrast (e.g., “double click” using bioorthogonal partners with faster kinetics, nanoparticle delivery to capitalize on EPR) have yielded little improvement. A method using a liposome bearing a cRGD tumor-targeting motif for azidosugar delivery resulted in the highest gains. These studies underscore the importance of both steps involved in metabolic bioorthogonal labeling (introduction of the azidosugar and optimization of probe administration) and also exposes the challenges to using this approach for imaging tumors *in vivo*.

Bioorthogonal Pretargeted Labeling

Pretargeting with Monoclonal Antibodies

An alternative approach to introduce a reactive chemical reporter onto cancer cells *in vivo* is pretargeting. Pretargeted labeling relies on the use of an affinity tag, typically a monoclonal antibody (mAb), to recognize and accumulate in tumor tissue with exceptionally high specificity. A significant liability with this method is that antibodies typically have long serum half-lives, sometimes on the order of days, resulting in high levels of background signal in imaging studies and, in the case of nuclear imaging with radiolabeled antibodies, toxic doses of radiation released systemically.[41] Bioorthogonal chemistry provides a means to mitigate these issues. Antibodies possessing reactive handle are injected and allowed an appropriate amount of time to accumulate at the tumor and clear from non-target regions. A subsequently administered bioorthogonal probe bearing a fluorophore or radionuclide imaging probe collects at the pretargeted site, with unreacted probe clearing quickly due to the relatively short circulation time of small molecules, thus achieving high contrast signal and a localized radiation dose (Figure 1.11).

Figure 1.11. Bioorthogonal pretargeted labeling of tumors in mice.

Robillard and coworkers made efforts to deploy this strategy using the Staudinger ligation.[6] Chimeric mAbs bearing azide groups were administered to mice. Different phosphine probes appended with a variety of linkers and radionuclides were injected shortly thereafter, with HPLC analysis of serum

fractions showing no evidence of successful conjugation *in vivo*. This was thought to be due to a combination of slow reaction kinetics, short probe serum half-life ($t_{1/2}$ < 15 min), and instability of the phosphines, which were found to oxidize to the unreactive phosphine oxides in mouse serum. This was in contrast to a previous report by Bertozzi and coworkers in a study that utilized much higher concentrations of both azide and phosphine.[4] Similar results were obtained using a panel of cyclooctyne probes in an *in vivo* mAb pretargeting assay, with little to no azide-dependent enhancement observed.[42]

The shortcomings of the Staudinger ligation and copper-free click chemistry led to a focus on faster bioorthogonal reactions for pretargeted labeling. Devaraj et al. developed a pretargeting system based on the inverse electron-demand Diels-Alder reaction between norbornene and tetrazine, successfully imaging cells in culture using mAb-norbornene and a tetrazine fluorophore.[43] This was later improved by using *trans*-cyclooctene as the chemical reporter, which reacts with tetrazines hundreds to thousands of times faster than does norbornene.[44]

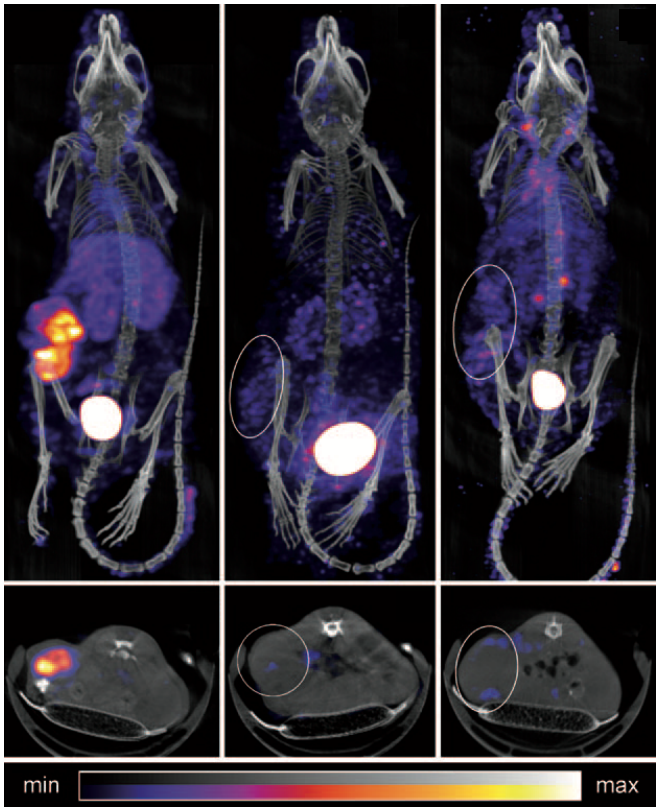

Figure 1.12. Tumor pretargeted labeling using the tetrazine ligation.
(Top) SPECT/CT images of mice administered (left to right) CC49-TCO, CC49, or Rtx-TCO (negative control) one day prior to tetrazine-[^{111}In] injection. (Bottom) Transverse tumor slices of the same. Figure 1.12 adapted with permission from reference (45), copyright 2010 WILEY-VCH Verlag GmbH & Co. KGaA, Weinheim.

In the wake of these developments, Robillard and coworkers aimed to apply tetrazine-TCO-based pretargeting in a mouse tumor model.[45] Mice bearing subcutaneous LS174T human colorectal cancer xenografts were treated with a TCO-modified CC49 mAb against the TAG72 antigen, which is overexpressed on solid tumors and has slow rates of internalization and shedding, creating optimal conditions for mAb pretargeting. After a clearance interval of 24 hours, IV-injected tetrazine-[^{111}In] and SPECT/CT imaging displayed tumor/muscle ratios of 13 and 0.5 for TCO-modified and unmodified mAbs, respectively, representing a TCO-dependent labeling enhancement of 26-fold (Figure 1.12). *Ex vivo* biodistribution studies confirmed this finding, with similar studies by other groups reporting the same.[46]

Even with this drastic improvement in labeling contrast over metabolic engineering approaches, Robillard and coworkers took several opportunities to progress their pretargeting method. As mentioned earlier, one pathway of TCO-deactivation is isomerization to the less reactive *cis*-cyclooctene. This was found to be mediated by copper-metalloproteins such as transcuprein and albumin present in mouse serum.[24] Simply shortening the linker between the TCO and mAb mitigated this effect through steric impedance of copper-bound proteins. Additionally, positioning the linker in an axial rather than equatorial conformation on the TCO core boosted its reactivity with tetrazine due to increased trans-annular interactions. Together, these modifications produced an outcome of higher pretargeted labeling efficiency.

For antibody-drug conjugates in the clinical setting, site-specific attachment sites are preferred to avoid heterogeneous mixtures of differentially potent constructs. Zeglis and coworkers devised a chemoenzymatic synthesis of site-specific mAb-TCO conjugates.[47] A galactosidase was used to trim off four terminal galactose residues on the heavy chain of humanized anti-A33 (huA33). Next, a promiscuous galatosyltransferase, Gal-T(Y289L) was used to install unnatural GalNAz residues. Finally, copper-free click with DIBO-TCO yielded huA33-TCO in a site-specific fashion. Analysis revealed a loading of 2.4 TCO/mAb out of a possible 4. Nonetheless, huA33-TCO performed adequately in tumor pretargeting experiments, although the authors note that there is no improvement over analogous studies using non-site-specifically modified mAbs. They later adopted this strategy to produce a modified huA33 for bimodal imaging, with NIR dyes added chemoenzymatically by the same route and TCOs attached nonspecifically to lysine residues via NHS-ester chemistry.[48]

As discussed before, an inherent deficiency in using antibodies for targeting is their prolonged serum residence times. This can be an obstacle even in pretargeted labeling because circulating antibodies can sequester bioorthogonal probes away from the region of interest. Robillard and coworkers circumvented this issue through the development of clearing agents consisting of a tetrazine conjugated to a galactose-coated albumin that could quench and shuttle circulating mAbs to the liver, but would be too large to extravasate into tumor tissue.[49] Indeed, clearing agents administered shortly before the injection of tetrazine probes accelerated the elimination of circulating antibody and

succeeded in reducing background signal, with a 15-fold improvement in the tumor/muscle ratio compared to the initial report (Figure 1.13). These clearing agents enabled the use of an mAb-TCO with heightened linker hydrophilicity and an extended serum half which allowed for greater accumulation with the tumor.[50]

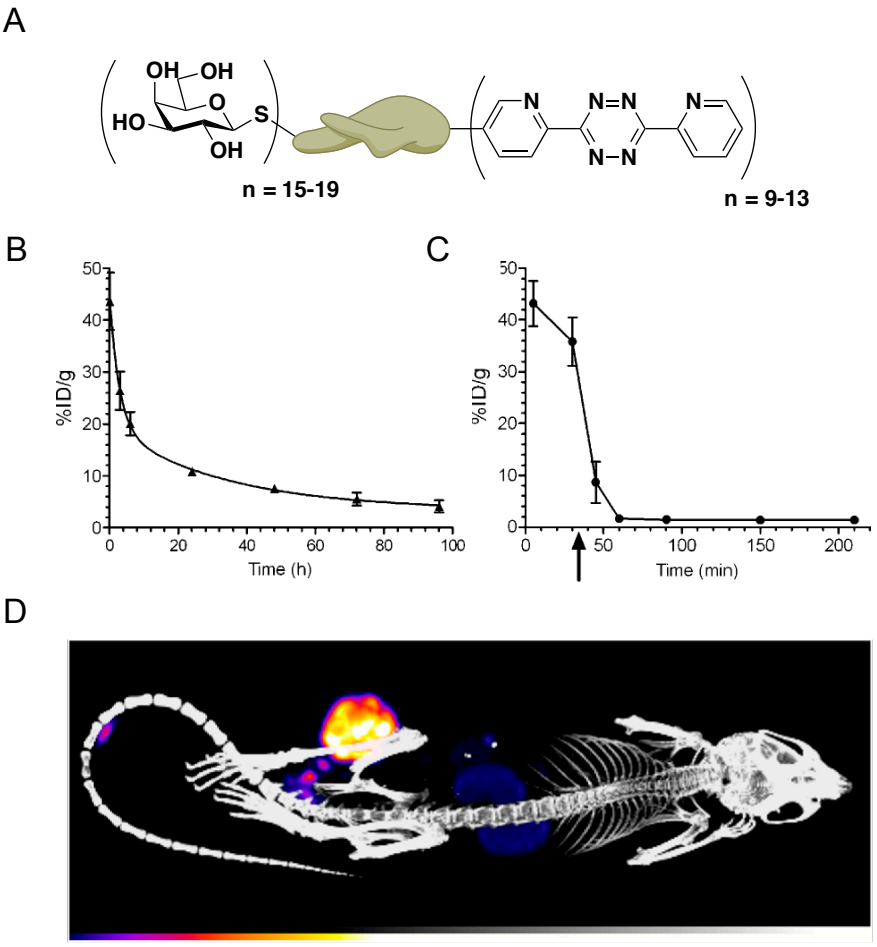

Figure 1.13. Clearing agent reduces circulating antibody and enhances signal. A) Clearing agent consisting of albumin decorated with an array of tetrazines and galactose residues. Serum residence of a radiolabeled antibody in the B) absence or C) presence of a clearing agent. Arrow indicates the time of clearing agent injection. D) SPECT/CT image of tumor-bearing mouse pretargeted with CC49-TCO and labeled with tetrazine-[^{111}In] after treatment with a clearing agent. Figure 1.13B-D adapted with permission from reference (49). This research was originally published in JNM, copyright by the Society of Nuclear Medicine and Molecular Imaging, Inc.

While clearing agents successfully amplified labeling intensity, the necessity for multiple injections of different species is undesirable in a clinical setting. This motivated the development of pretargeting tags with shorter half-

lives than those of mAbs. A TCO-modified diabody (55 kDa versus 150 kDa for a typical mAb) proved to be effective for clearing agent-free pretargeted imaging in tumor-bearing mice, with tumor/kidney ratios approaching those achieved in the mAb/clearing agent system.[51] Likewise, an mAb-mimicking TCO-affibody 7.5 kDa in size performed in a similar manner, with pretargeting generating a more favorable tumor/kidney ratio than a directly radiolabeled affibody.[52] These results suggest that affinity tags with more favorable pharmacokinetic properties can be effective at reducing off-target radiation exposure using bioorthogonal pretargeted labeling, although the advancement of these agents is still in the nascent stage.

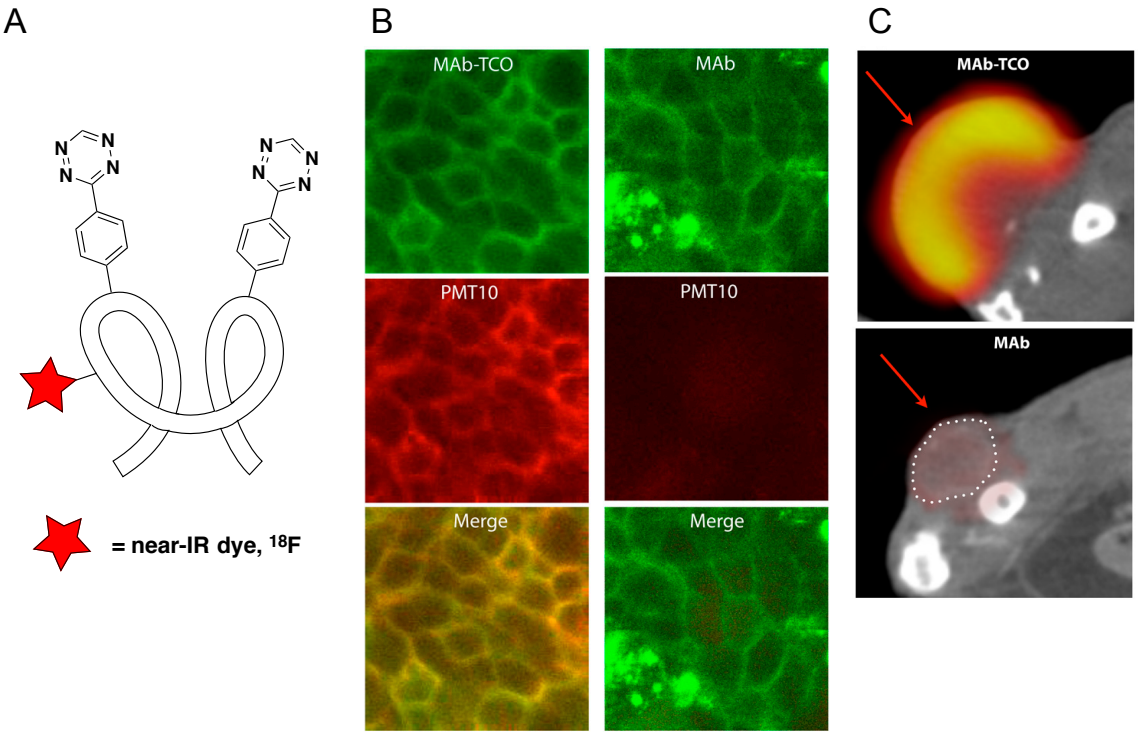

Figure 1.14. Polymer-modified tetrazines label tumors in mice. A) Tetrazines conjugated to a 10 kDa dextran polymer bearing either a near-IR dye or ^{18}F radionuclide. B) Fluorescence microscopy in dorsal window-chambered mice pretargeted using a green fluorescent mAb-TCO conjugate. C) PET/CT images in mice tagged with TCO-functionalized or unmodified mAb. Figure 1.14B-C adapted with permission from reference (55).

Amid optimizations to the TCO-mAb component, many groups recognized that structural changes to the tetrazine core could profoundly influence its activity and biodistribution. Zeglis et al. noted that a tetrazine armed with an aryl sarcophagine chelator showed exclusively renal clearance and no gastrointestinal accumulation compared to other chelators, making it ideal for imaging colorectal cancers.[53] Koo et al. observed that altering the hydrophilicity

and serum half-lives of tetrazine-Cy5s affected their *in vivo* labeling efficiencies, with longer-circulating probes having more robust labeling.[54] Similarly, Weissleder and coworkers found that attachment of pendant tetrazines to dextran polymers increased the serum half-life resulting in greater labeling compared to small molecule tetrazines, with polymer-modified tetrazines (PMTs) built using 10 kDa dextrans striking the optimal balance between increased reaction efficiency and elevated background.[55] PMTs proved useful for the imaging of mouse tumors by fluorescence microscopy in dorsal window-chambered mice and whole animal PET/CT using NIR fluorophore and ^{18}F-conjugated dextrans, respectively (Figure 1.14).

Weissleder and coworkers also expanded the portfolio of tetrazine probes with the development of a series of fluorogenic tetrazines that undergo fluorescence enhancement upon ligation (Figure 1.15).

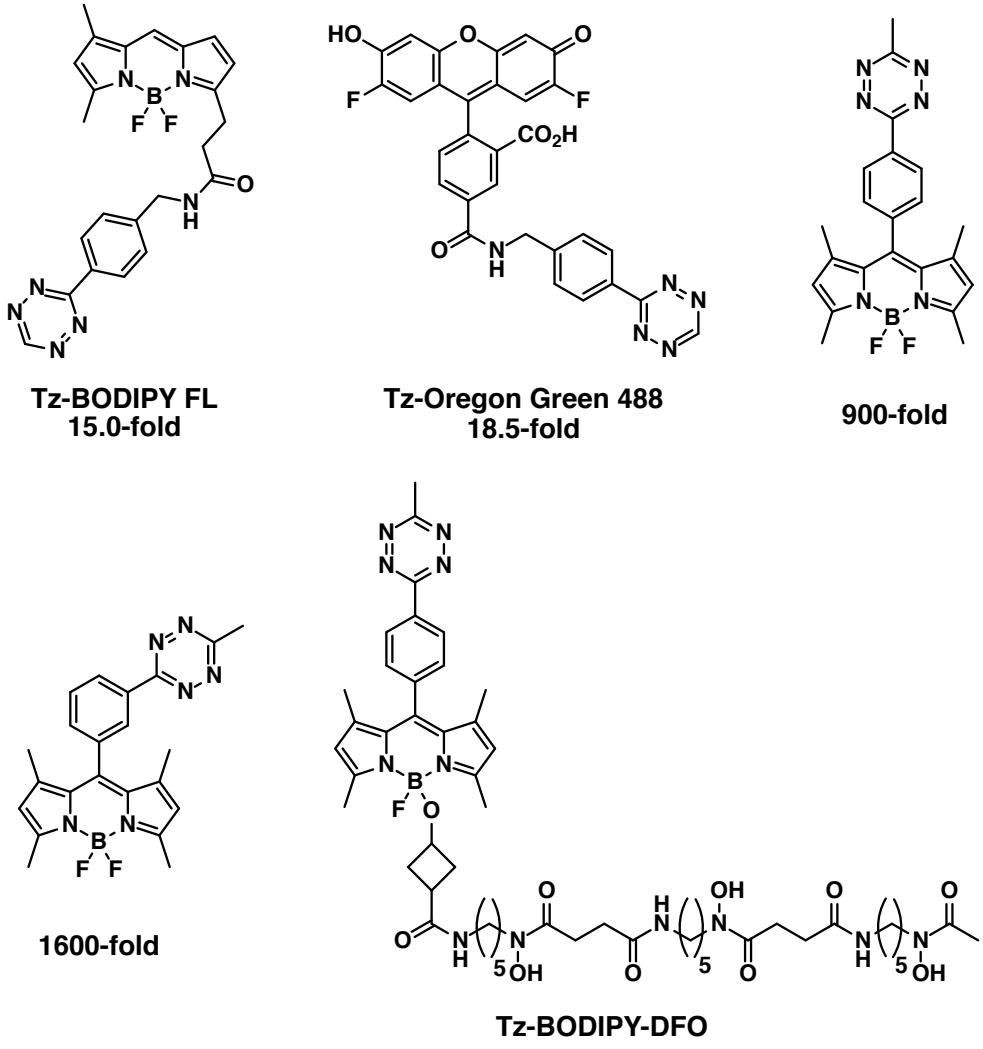

Figure 1.15. Turn-on properties of fluorogenic tetrazine probes.[56–58]

An initial report consisted of benzylaminotetrazine linked to various commercially available fluorophores through short molecular spacers.[56] Fluorescence quenching, proposed to be through FRET by virtue of tetrazine's absorbance maximum of 515 nm, was alleviated upon ablation of the tetrazine core by reaction with TCO. Probes of this nature exhibited turn-on magnitudes of up to 20-fold and enabled the intracellular labeling of TCO-modified Taxol. The following generation of probes utilized a through-bond energy transfer quenching mechanism in directly conjugated tetrazine-BODIPY π systems to achieve turn-on values of up to 1600-fold in aqueous media.[57] In subsequent work, a deferoxamine moiety was appended to the BODIPY BF_2 core via an alkoxy-linkage to afford tetrazine-BODIPY-DFO, and chelation of ^{89}Zr afforded a radiolabeled fluorescence turn-on probe which was used for multimodal fluorescence and PET imaging in a mouse tumor model.[58]

Pretargeted tumor labeling methods are primarily tested in idealized systems where antibody internalization and antigen shedding are negligible. This is frequently not the case in the actual disease state. CA19.9, a clinical biomarker of pancreatic ductal adenocarcinoma, is known to be shed into circulation and also to internalize the 5B1 mAb that recognizes it. Lewis and coworkers conducted pretargeting experiments using 5B1-TCO in an orthotopic model of pancreatic cancer using Capan-2 cells, which has been documented to shed CA19.9 at physiological levels.[59] PET imaging with a tetrazine-[^{64}Cu] probe was able to delineate tumor tissue by 6 hours post injection, albeit with less contrast than in BxPC3 cells, which are not known to shed CA19.9 and internalize 5B1 at a slower rate than Capan-2. Dosimetry compared with directly radiolabeled 5B1-[^{89}Zr] revealed a 25-fold reduction in total body radiation exposure using the pretargeted approach. This model was further used to evaluate a novel tetrazine-chelator Al-^{18}F complex for pretargeted PET imaging, thus applying bioorthogonal labeling in a more clinically relevant situation.[60]

Other Methods of Pretargeted Bioorthogonal Labeling

While antibody-based approaches have dominated the tumor imaging arena due to precedence for their use in cancer imaging and treatment, other avenues of pretargeting have been explored as well. Reiner and coworkers synthesized a tetrazine conjugated to a pH low insertion peptide (pHLIP), which undergoes a conformational change upon sensing an acidic environment, such as that of cancer cells, and imbeds into the plasma membrane.[61] Using intratumorally injected tetrazine-pHLIP and liposomes modified with TCO and ^{18}F, a 7-fold enhancement over control tumors was observed by PET amidst high systemic signal, likely resulting from the slow serum clearance of liposomes.

In an aberration from a landscape replete with tetrazine ligations and copper-free click reactions, Tang et al. endeavored to use an older bioorthogonal reaction for pretargeted labeling – the condensation of aldehydes and aminooxy compounds to form oximes.[62] Aminooxy-modified liposomes were directly injected into mouse flank tumors, where aminooxy uptake occurred through

membrane fusion. IV administration of polyethyleneglycol/polylactic acid polymers displaying surface aldehydes and carrying a radionuclide payload allowed for assessment of labeling through PET imaging (Figure 1.16). Compared with non-aminooxy-engineered tumors, aminooxy tumors labeled less than 2-fold above control at various timepoints (maximum of 1.75-fold 1 hour post injection), ostensibly the result of nonspecific accumulation of nanoparticle probes within the tumor.

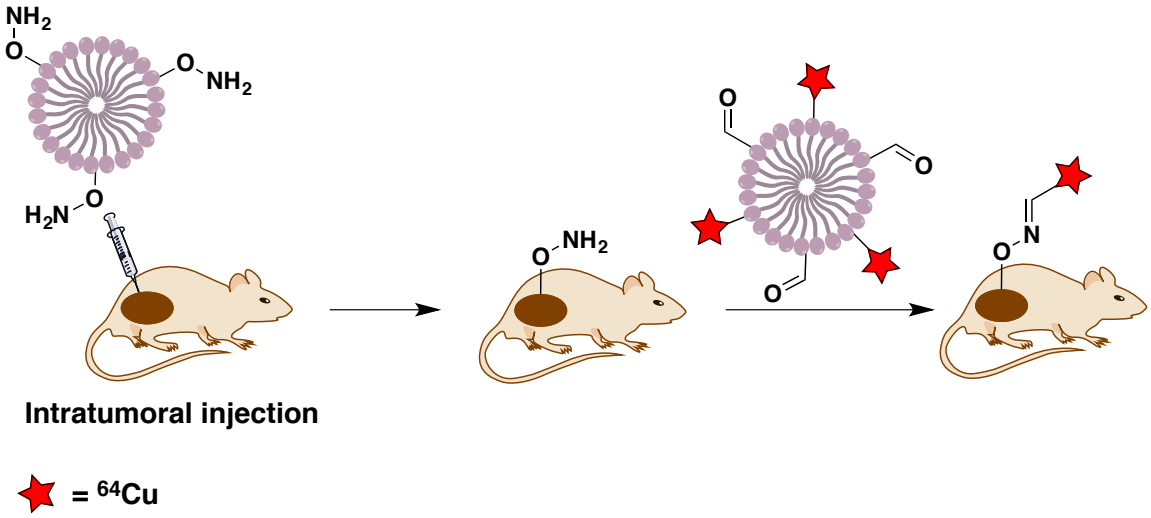

Figure 1.16. Liposomal pretargeting for the oxime ligation in mice.

In a manner similar to Kim and coworkers' chitosan nanoparticle delivery of azidosugar, Hou et al. aimed to use nanoparticles to deliver TCO to tumors via EPR.[63] TCO-modified supramolecular nanoparticles were constructed through the self-assembly of a number of dextran and lipid-based components and administered to tumor-bearing mice. Tetrazine-[^{64}Cu] delineated tumors in PET imaging, but *ex vivo* quantification suggested labeling enhancements of only 2.2-fold over the unfunctionalized nanoparticle control, and 6-fold over directly radiolabeled nanoparticles, the metric being tumor/liver ratio.

Comparable labeling was obtained through EPR pretargeting with mesoporous silica nanoparticles (MSNs). Lee et al. armed MSNs ~150 nm in size with reactive DIBAC moieties for copper-free click chemistry.[64] MSNs were introduced IV to mice bearing subcutaneous flank tumors prior to injection of an ^{18}F-azide probe. The amount of signal in the tumor for the highest amount of MSN tested was only 2-fold over mice given ^{18}F-azide. Curiously, MSNs seem to exhibit inconsistent biodistribution patterns in mice. Denk at al. reported TCO-modified MSNs injected into healthy mice accumulated almost exclusively in the lungs within minutes, as apparent by labeling with a tetrazine-[^{11}C] PET tracer.[65] By contrast, Oikonen et al. observed MSNs distributed throughout various organs, with preferential build-up in the spleen at early timepoints.[66] Taken

together, these studies utilizing nanoparticle delivery of chemical reporters indicate quite clearly that, as in the case with metabolic incorporation, EPR alone is an ineffective pretargeting method in the absence of other targeting mechanisms.

Applications for Drug Delivery and Therapy

The bulk of the literature surrounding bioorthogonal labeling of tumors focuses on imaging probes, but the ability to selectively tag cancer *in vivo* opens the door for the delivery of other types of molecular cargo, such as agents for therapy. Of particular interest are bioorthogonal prodrugs, in which an active chemotherapeutic is decaged only upon contact with its bioorthogonal reaction partner at the cancer cell surface. In this manner, a toxin can be activated selectively in the vicinity of the tumor, reducing the noxious adverse effects associated with traditional chemotherapies. Recent years have seen the development of varied bioorthogonal approaches to treat cancer in cell culture and animal models by delivery of prodrugs and agents for photodynamic and radiation therapy, and *in situ* drug assembly.

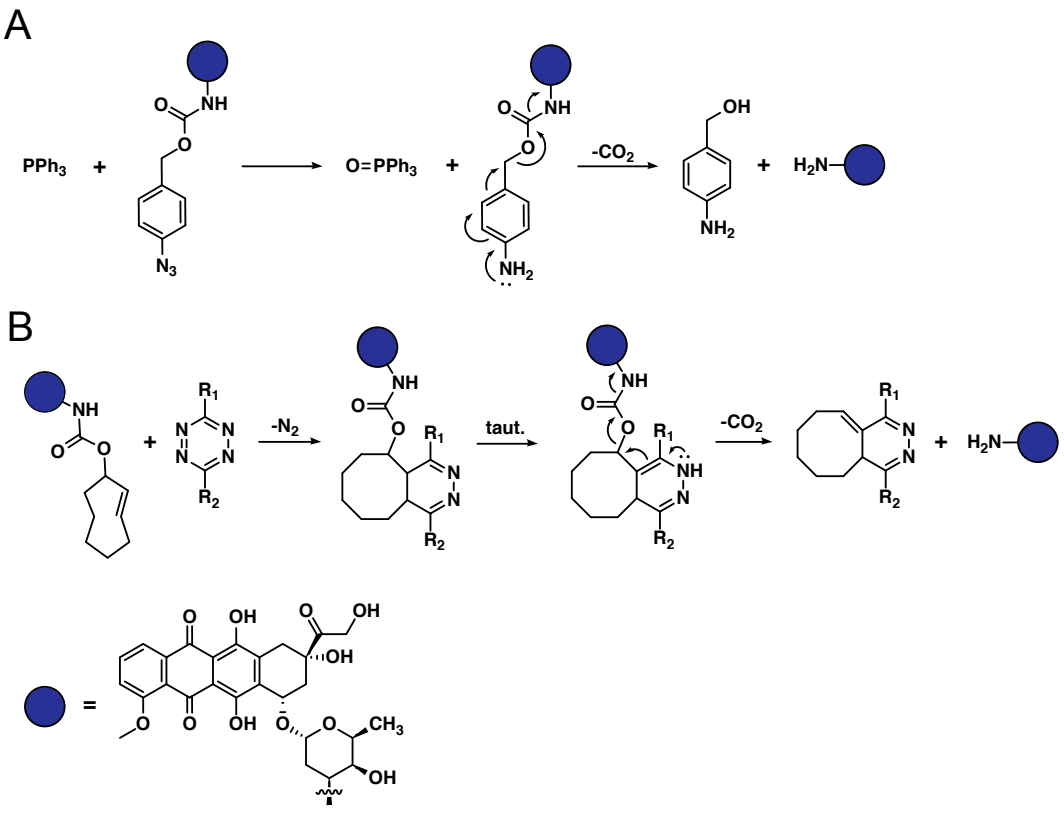

Figure 1.17. Bioorthogonal prodrug activation. Decaging of doxorubicin triggered by the A) Staudinger ligation and B) tetrazine-TCO ligation.

Some bioorthogonal reactions are amenable to the incorporation of self-immolative linkers, facilitating the construction of decagable prodrugs. Based on the Staudinger ligation's utility *in vivo*, Robillard and coworkers built a drug release system based on the classic Staudinger reduction of azides to amines.[67] Their design features the cancer drug doxorubicin attached to a benzyl azide through a carbamate linker. Upon phosphine-mediated reduction of the azide to an amine, free doxorubicin is released via a decarboxylation-elimination mechanism (Figure 1.17A). This proved effective at treating cancer cells in culture, with the azido-prodrug exhibiting far less toxicity than doxorubicin. An upgraded variant relied on the tetrazine ligation, the prodrug consisting of a carbamate-linked doxorubicin at the allylic position of TCO.[68] Increased electron density resulting from the reaction forces the traceless release of doxorubicin (Figure 1.17B). This arrangement was combined with *in vivo* tumor pretargeting using an mAb-TCO-doxorubicin conjugate in mice.[69] *Ex vivo* analysis showed a tetrazine-dependent release of doxorubicin into the tumor, although the authors did not characterize the effect on tumor growth.

Oneto and coworkers sought to apply these principles in a hydrogel-based mode of localized drug delivery. Initially, a TCO-conjugated alginate hydrogel was synthesized and implanted into mice.[70] Systemically administered tetrazine-[^{111}In] was observed to accumulate within the gel and surrounding tissue, suggesting that this method might be useful for local delivery of a therapeutic payload. A subsequent iteration exchanged the positions of the reactive partners, with tetrazine-modified hydrogels implanted peritumorally in a mouse xenograft model of soft-tissue sarcoma.[71] IV-injected TCO-doxorubicin was found to be effective at halting tumor growth compared to unmodified doxorubicin and notably averted the harmful side effects (lowered body weight and decimated reticulocyte count) observed with the free drug (Figure 1.18).

Bioorthogonal chemistry has also been used for the targeted delivery of therapeutic agents other than prodrugs. Kim and coworkers used their BCN-modified chitosan nanoparticles for delivery of Ce6, a photosensitizer, to azide-labeled tumors in mice.[39] Upon irradiation, Ce6 generates toxic reactive oxygen species that destroy tumors. Despite low levels of tumor contrast observed in preliminary imaging studies, BCN-CNP-delivered Ce6 showed efficacy in the photodynamic treatment of tumors over both free Ce6 and non-pretargeted BCN-CNP-Ce6.

Along with its basis in nuclear imaging, the radiation emitted by radionuclides is cytotoxic and can be harnessed as a means of anticancer therapy. The long circulation times of radiolabeled antibodies result in unwanted doses of off-target radiation, a liability that may be quelled by bioorthogonal pretargeting. Accordingly, Lewis and Zeglis used an mAb pretargeting approach for tumor radioimmunotherapy. Their previously developed 5B1-TCO mAb conjugates against pancreatic adenocarcinoma were used for the pretargeted delivery of tetrazine-[^{177}Lu] to subcutaneous pancreatic cancer xenografts in mice.[72] In monitoring tumor size up to 51 days post-treatment, the authors observed a dose-dependent response, with the highest radiation dose preventing cancer growth more effectively than both the lowest tested dose and untreated

control. While this result was promising, the study lacked a comparison to a directly radiolabeled 5B1, which would be more reflective of current clinical technology, as well as an evaluation of any reduction in radiation-induced side effects.

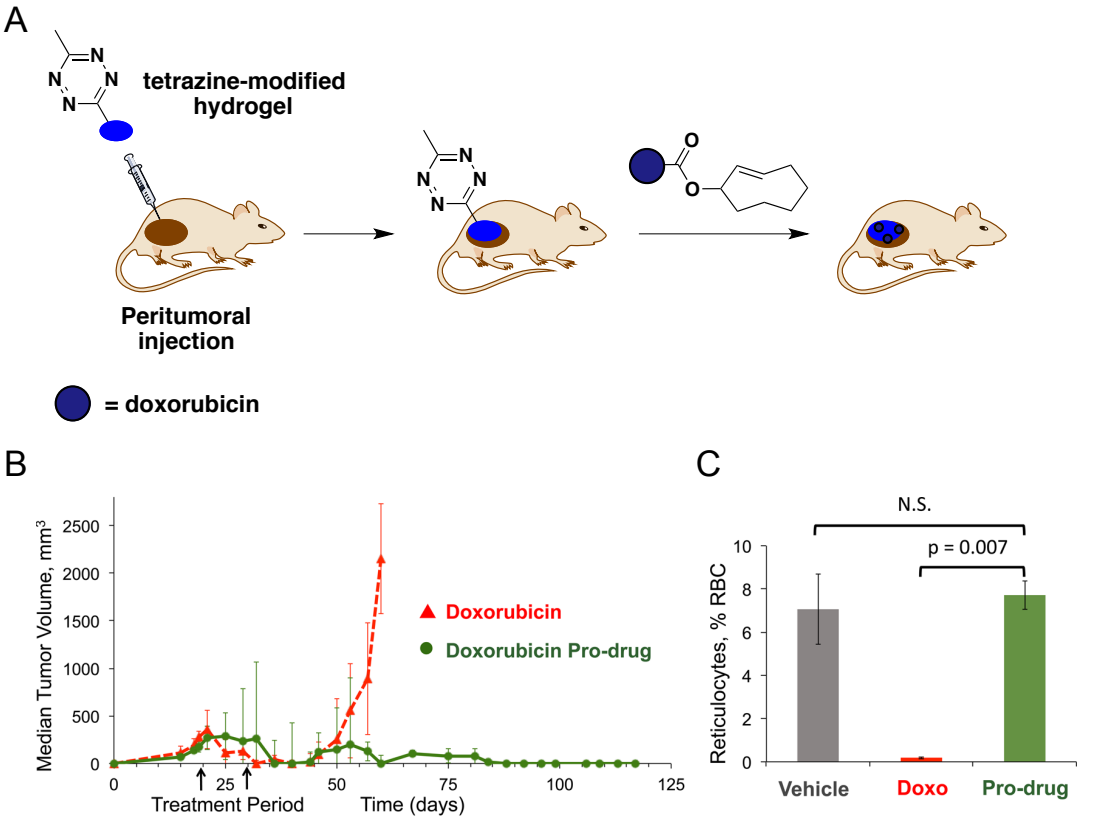

Figure 1.18. Bioorthogonal hydrogel for drug delivery. A) Hydrogel-modified tetrazine (HMT) induces localized doxorubicin release. B) Tumor growth in HMT-implanted mice after treatment with TCO-doxorubicin or free doxorubicin. C) Reticulocyte counts after treatment with TCO-doxorubicin, doxorubicin, or vehicle control. Figure 1.18B-C adapted with permission from reference (71). This is an unofficial adaptation of an article that appeared in an ACS publication. ACS has not endorsed the content of this adaptation or the context of its use.

Finally, bioorthogonal chemistry has shown promise for the *in vivo* assembly of drugs to treat disease. Clavadestcher et al. reported the incorporation of copper(I) into a TentaGel resin to produce nanoparticle catalysts for copper-catalyzed click chemistry.[73] These Cu-NPs were used for the *in situ* synthesis of a cytotoxic triazole analog of Combretastatin A4 from azide and alkyne precursors to kill cancer cells in culture (Figure 1.19). To assess performance *in vivo*, Cu-NPs were implanted into the yolks of embryonic

zebrafish, where it successfully catalyzed the assembly of a triazole containing fluorophore from starting materials added to the media, with fluorescent signal localized to the implantation site. While copper-catalyzed click remains unproven in mammalian systems, this study demonstrates that more exotic applications of bioorthogonal chemistry are still in development.

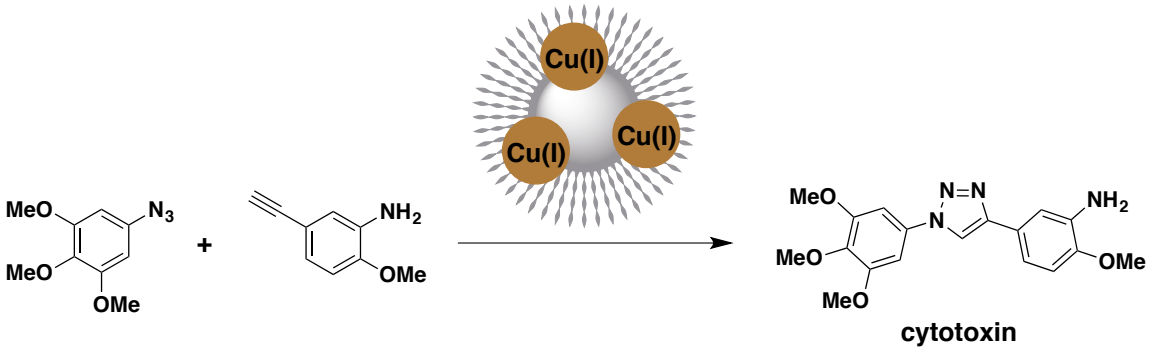

Figure 1.19 *In situ* drug assembly catalyzed by a copper(I) nanoparticle.

Conclusion

A great deal of the recent work regarding bioorthogonal labeling has focused on applications toward imaging cancer in mouse models, both as a result of cancer's pervasiveness in human disease and the viewpoint of mammalian systems as a true litmus test for illustrating bioorthogonality. Although there currently exists a plethora of unique bioorthogonal reactions, only a handful have seen widespread use for tumor targeting. As such, most of the research within this realm has been in optimizing the copper-free click reaction and tetrazine ligation for *in vivo* performance. A survey of the literature reveals that both modulation of reaction kinetics and tuning of probe pharmacokinetic properties have been employed to enhance the level of selectivity attained.

By virtue of the azide's versatility as a metabolically incorporated chemical reporter, the copper-free click reaction (and to a lesser degree, the Staudinger ligation) has generally been used to label azidosialic acid on the cell surface of metabolically engineered tumors. Originally proposed as a tool for diagnosing and monitoring the progression of cancer based on the observed overexpression of sialic acid by a variety of different cancers, the low levels of tumor labeling over controls precludes its clinical relevance. As a research tool for assaying the distribution of cancer sialylation *in vivo*, the copper-free click reaction also has limitations. Again, poor azide-specific labeling efficiency (2-fold in most cases, 6-fold optimally) may impede the detection of subtle changes in sialic acid expression. Still, a metabolic incorporation strategy has proven useful for the *in vivo* tagging of cancer-associated sialoglycoproteins, allowing for enrichment and proteomic characterization. Approaches such as this hold promise for better elucidating sialoglycan expression patterns and how they influence cancer

behavior. As well, the development of cyclooctyne probes with improved bioavailability and continual optimization of azidosugar delivery to tumors may upgrade the copper-free click reaction's utility for imaging.

The fast reaction kinetics of the TCO-tetrazine ligation enables it to be used at low, more clinically relevant concentrations of reagents, abetting its popularity for pretargeted labeling with mAbs. As a result, a host of groups submitted complementary additions to the tetrazine ligation pretargeting repertoire, optimizing such factors as mAb-conjugation strategy, TCO and tetrazine structure, and the use of clearing agents to reduce background. Indeed, tetrazine ligation-based pretargeting has proven effective for fluorescence and radionuclide labeling in a variety of tumor models, yielding less off-target signal than directly tagged antibodies alone. Barriers to its use in medicine may stem from tetrazine and TCO instability issues *in vivo*, which may be curtailed through structural modification, though at cost to reactivity.

Alongside applications in imaging have been advancements to using bioorthogonal chemistry for therapy. The most promising developments center around new modes of prodrug delivery and activation, although the field of bioorthogonal therapeutics is still in the emergent stage. While the clinical presence of bioorthogonal chemistry has yet to be realized, continual innovations on the front of drug delivery and nuclear imaging/radioimmunotherapy pave the way, and are testament to the power of using chemical technology to navigate biological landscapes.

References

(1) Büll, C.; Stoel, M. A.; Den Brok, M. H.; Adema, G. J. Sialic Acids Sweeten a Tumor's Life. *Cancer Res.* **2014**, *74*, 3199–3204.

(2) Saxon, E.; Bertozzi, C. R. Cell Surface Engineering by a Modified Staudinger Reaction. *Science* **2000**, *287*, 2007–2010.

(3) Lin, F. L.; Hoyt, H. M.; Van Halbeek, H.; Bergman, R. G.; Bertozzi, C. R. Mechanistic Investigation of the Staudinger Ligation. *J. Am. Chem. Soc.* **2005**, *127*, 2686–2695.

(4) Chang, P. V; Prescher, J. A.; Sletten, E. M.; Baskin, J. M.; Miller, I. A.; Agard, N. J.; Lo, A.; Bertozzi, C. R. Copper-Free Click Chemistry in Living Animals. *Proc. Natl. Acad. Sci. U. S. A.* **2010**, *107*, 1821–1826.

(5) Neves, A. a; Stöckmann, H.; Harmston, R. R.; Pryor, H. J.; Alam, I. S.; Ireland-Zecchini, H.; Lewis, D. Y.; Lyons, S. K.; Leeper, F. J.; Brindle, K. M. Imaging Sialylated Tumor Cell Glycans in Vivo. *FASEB J.* **2011**, *25*, 2528–2537.

(6) Vugts, D. J.; Vervoort, A.; Stigter-Van Walsum, M.; Visser, G. W. M.; Robillard, M. S.; Versteegen, R. M.; Vulders, R. C. M.; Herscheid, J. D. M.; Van Dongen, G. A. M. S. Synthesis of Phosphine and Antibody-Azide Probes for in Vivo Staudinger Ligation in a Pretargeted Imaging and Therapy Approach. *Bioconjug. Chem.* **2011**, *22*, 2072–2081.

(7) Hein, J. E.; Fokin, V. V. Copper-Catalyzed Azide-Alkyne Cycloaddition and beyond: New Reactivity of Copper Acetylides. *Chem Soc Rev.* **2011**, *39*, 1302–1315.

(8) Amo, D. S. Del; Wang, W. Biocompatible Copper (I) Catalysts for in Vivo Imaging of Glycans. *J. Am. Chem. Soc.* **2010**, *132*, 16893–16899.

(9) Zheng, T.; Jiang, H.; Gros, M.; Soriano Del Amo, D.; Sundaram, S.; Lauvau, G.; Marlow, F.; Liu, Y.; Stanley, P.; Wu, P. Tracking N-Acetyllactosamine on Cell-Surface Glycans in Vivo. *Angew. Chem. Int. Ed.* **2011**, *50*, 4113–4118.

(10) Jiang, H.; Zheng, T.; Lopez-Aguilar, A.; Feng, L.; Kopp, F.; Marlow, F. L.; Wu, P. Monitoring Dynamic Glycosylation in Vivo Using Supersensitive Click Chemistry. *Bioconjug. Chem.* **2014**, *25*, 698–706.

(11) Agard, N. J.; Prescher, J. A.; Bertozzi, C. R. A Strain-Promoted [3 + 2] Azide-Alkyne Cycloaddition for Covalent Modification of Biomolecules in Living Systems. *J. Am. Chem. Soc.* **2004**, *126*, 15046–15047.

(12) Agard, N. J.; Baskin, J. M.; Prescher, J. A.; Lo, A.; Bertozzi, C. R. A Comparative Study of Bioorthogonal Reactions with Azides. *ACS Chem. Biol.* **2006**, *1*, 644–648.

(13) Baskin, J. M.; Prescher, J. A.; Laughlin, S. T.; Agard, N. J.; Chang, P. V; Miller, I. A.; Lo, A.; Codelli, J. A.; Bertozzi, C. R. Copper-Free Click Chemistry for Dynamic in Vivo Imaging. *Proc. Natl. Acad. Sci. U. S. A.* **2007**, *104*, 16793–16797.

(14) Sletten, E. M.; Bertozzi, C. R. A Hydrophilic Azacyclooctyne for Cu-Free Click Chemistry. *Org. Lett.* **2008**, *10*, 3097–3099.

(15) Jewett, J. C.; Sletten, E. M.; Bertozzi, C. R. Rapid Cu-Free Click Chemistry

with Readily Synthesized Biarylazacyclooctynones. *J. Am. Chem. Soc.* **2010**, *132*, 3688–3690.
(16) Debets, M. F.; van Berkel, S. S.; Schoffelen, S.; Rutjes, F. P. J. T.; van Hest, J. C. M.; van Delft, F. L. Aza-Dibenzocyclooctynes for Fast and Efficient Enzyme PEGylation via Copper-Free (3+2) Cycloaddition. *Chem. Commun.* **2010**, *46*, 97–99.
(17) Dommerholt, J.; Schmidt, S.; Temming, R.; Hendriks, L. J. A.; Rutjes, F. P. J. T.; Van Hest, J. C. M.; Lefeber, D. J.; Friedl, P.; Van Delft, F. L. Readily Accessible Bicyclononynes for Bioorthogonal Labeling and Three-Dimensional Imaging of Living Cells. *Angew. Chem. Int. Ed.* **2010**, *49*, 9422–9425.
(18) Stöckmann, H.; Neves, A. a.; Stairs, S.; Ireland-Zecchini, H.; Brindle, K. M.; Leeper, F. J. Development and Evaluation of New Cyclooctynes for Cell Surface Glycan Imaging in Cancer Cells. *Chem. Sci.* **2011**, *2*, 932.
(19) Mbua, N. E.; Guo, J.; Wolfert, M. A.; Steet, R.; Boons, G. J. Strain-Promoted Alkyne-Azide Cycloadditions (SPAAC) Reveal New Features of Glycoconjugate Biosynthesis. *ChemBioChem* **2011**, *12*, 1912–1921.
(20) De Almeida, G.; Sletten, E. M.; Nakamura, H.; Palaniappan, K. K.; Bertozzi, C. R. Thiacycloalkynes for Copper-Free Click Chemistry. *Angew. Chem. Int. Ed.* **2012**, *51*, 2443–2447.
(21) Van Geel, R.; Pruijn, G. J. M.; Van Delft, F. L.; Boelens, W. C. Preventing Thiol-Yne Addition Improves the Specificity of Strain-Promoted Azide-Alkyne Cycloaddition. *Bioconjug. Chem.* **2012**, *23*, 392–398.
(22) Blackman, M. L.; Royzen, M.; Fox, J. M. Tetrazine Ligation: Fast Bioconjugation Based on Inverse-Electron-Demand Diels-Alder Reactivity. *J. Am. Chem. Soc.* **2008**, *130*, 13518–13519.
(23) Patterson, D. M.; Nazarova, L. A.; Prescher, J. A. Finding the Right (Bioorthogonal) Chemistry. *ACS Chem. Biol.* **2014**, *9*, 592–605.
(24) Rossin, R.; Van Den Bosch, S. M.; Ten Hoeve, W.; Carvelli, M.; Versteegen, R. M.; Lub, J.; Robillard, M. S. Highly Reactive Trans-Cyclooctene Tags with Improved Stability for Diels-Alder Chemistry in Living Systems. *Bioconjug. Chem.* **2013**, *24*, 1210–1217.
(25) Laughlin, S. T.; Baskin, J. M.; Amacher, S. L.; Bertozzi, C. R. In Vivo Imaging of Membrane-Associated. *Science* **2008**, *320*, 664–667.
(26) Baskin, J. M.; Dehnert, K. W.; Laughlin, S. T.; Amacher, S. L.; Bertozzi, C. R. Visualizing Enveloping Layer Glycans during Zebrafish Early Embryogenesis. *Proc. Natl. Acad. Sci.* **2010**, *107*, 10360–10365.
(27) Dehnert, K. W.; Beahm, B. J.; Huynh, T. T.; Baskin, J. M.; Laughlin, S. T.; Wang, W.; Wu, P.; Amacher, S. L.; Bertozzi, C. R. Metabolic Labeling of Fucosylated Glycans in Developing Zebrafish. *ACS Chem. Biol.* **2011**, *6*, 548–552.
(28) Dehnert, K. W.; Baskin, J. M.; Laughlin, S. T.; Beahm, B. J.; Naidu, N. N.; Amacher, S. L.; Bertozzi, C. R. Imaging the Sialome during Zebrafish Development with Copper-Free Click Chemistry. *ChemBioChem* **2012**, *13*, 353–357.
(29) Beahm, B. J.; Dehnert, K. W.; Derr, N. L.; Kuhn, J.; Eberhart, J. K.;

Spillmann, D.; Amacher, S. L.; Bertozzi, C. R. A Visualizable Chain-Terminating Inhibitor of Glycosaminoglycan Biosynthesis in Developing Zebrafish. *Angew. Chem. Int. Ed.* **2014**, *53*, 3347–3352.
(30) Wu, H.; Yang, J.; Šečkutė, J.; Devaraj, N. K. In Situ Synthesis of Alkenyl Tetrazines for Highly Fluorogenic Bioorthogonal Live-Cell Imaging Probes. *Angew. Chem. Int. Ed.* **2014**, *53*, 5805–5809.
(31) Agarwal, P.; Beahm, B. J.; Shieh, P.; Bertozzi, C. R. Systemic Fluorescence Imaging of Zebrafish Glycans with Bioorthogonal Chemistry. *Angew. Chem. Int. Ed.* **2015**, *54*, 11504–11510.
(32) Laughlin, S. T.; Bertozzi, C. R. In Vivo Imaging of Caenorhabditis Elegans Glycans. *ACS Chem. Biol.* **2009**, *4*, 1068–1072.
(33) Su, Y.; Li, L.; Wang, H.; Wang, X.; Zhang, Z. All-in-One Azides: Empowered Click Reaction for in Vivo Labeling and Imaging of Biomolecules. *Chem. Commun.* **2016**, *52*, 2185–2188.
(34) Chang, P. V; Chen, X.; Smyrniotis, C.; Xenakis, A.; Hu, T.; Bertozzi, C. R.; Wu, P. Metabolic Labeling of Sialic Acids in Living Animals with Alkynyl Sugars. *Angew. Chem. Int. Ed.* **2009**, *48*, 4030–4033.
(35) Neves, A.; Stöckmann, H.; Wainman, Y.; Kuo, J.; Fawcett, S.; Leeper, F.; Brindle, K. Imaging Cell Surface Glycosylation in Vivo Using “Double Click” Chemistry. *Bioconjug. Chem.* **2013**, *24*, 934–941.
(36) Neves, A. A.; Wainman, Y. A.; Wright, A.; Kettunen, M. I.; Rodrigues, T. B.; McGuire, S.; Hu, D. E.; Bulat, F.; Geninatti Crich, S.; Stöckmann, H.; Leeper, F. J.; Brindle, K. M. Imaging Glycosylation in Vivo by Metabolic Labeling and Magnetic Resonance Imaging. *Angew. Chem. Int. Ed.* **2016**, *55*, 1286–1290.
(37) Prabhakar, U.; Maeda, H.; K. Jain, R.; Sevick-Muraca, E. M.; Zamboni, W.; Farokhzad, O. C.; Barry, S. T.; Gabizon, A.; Grodzinski, P.; Blakey, D. C. Challenges and Key Considerations of the Enhanced Permeability and Retention Effect for Nanomedicine Drug Delivery in Oncology. *Cancer Res.* **2013**, *73*, 2412–2417.
(38) Koo, H.; Lee, S.; Na, J. H.; Kim, S. H.; Hahn, S. K.; Choi, K.; Kwon, I. C.; Jeong, S. Y.; Kim, K. Bioorthogonal Copper-Free Click Chemistry In Vivo for Tumor-Targeted Delivery of Nanoparticles. *Angew. Chem. Int. Ed.* **2012**, *51*, 11836–11840.
(39) Lee, S.; Koo, H.; Na, J. H.; Han, S. J.; Min, H. S.; Lee, S. J.; Kim, S. H.; Yun, S. H.; Jeong, S. Y.; Kwon, I. C.; Choi, K.; Kim, K. Chemical Tumor-Targeting of Nanoparticles Based on Metabolic Glycoengineering and Click Chemistry. *ACS Nano* **2014**, *8*, 2048–2063.
(40) Xie, R.; Dong, L.; Huang, R.; Hong, S.; Lei, R.; Chen, X. Targeted Imaging and Proteomic Analysis of Tumor-Associated Glycans in Living Animals. *Angew. Chem. Int. Ed.* **2014**, *53*, 14082–14086.
(41) van de Watering, F. C. J.; Rijpkema, M.; Robillard, M.; Oyen, W. J. G.; Boerman, O. C. Pretargeted Imaging and Radioimmunotherapy of Cancer Using Antibodies and Bioorthogonal Chemistry. *Front. Med.* **2014**, *1*, 1–11.
(42) Van den Bosch, S. M.; Rossin, R.; Renart Verkerk, P.; Ten Hoeve, W.; Janssen, H. M.; Lub, J.; Robillard, M. S. Evaluation of Strained Alkynes for

Cu-Free Click Reaction in Live Mice. *Nucl. Med. Biol.* **2013**, *40*, 415–423.
(43) Devaraj, N. K.; Weissleder, R.; Hilderbrand, S. A. Tetrazine-Based Cycloadditions : Application to Pretargeted Live Cell Imaging Tetrazine-Based Cycloadditions : Application to Pretargeted Live Cell Imaging. *Bioconjug. Chem.* **2008**, *19*, 2297–2299.
(44) Devaraj, N. K.; Upadhyay, R.; Haun, J. B.; Hilderbrand, S. A.; Weissleder, R. Fast and Sensitive Pretargeted Labeling of Cancer Cells through a Tetrazine/trans-Cyclooctene Cycloaddition. *Angew. Chem. Int. Ed.* **2009**, *48*, 7013–7016.
(45) Rossin, R.; Verkerk, P. R.; Van Den Bosch, S. M.; Vulders, R. C. M.; Verel, I.; Lub, J.; Robillard, M. S. In Vivo Chemistry for Pretargeted Tumor Imaging in Live Mice. *Angew. Chem. Int. Ed.* **2010**, *49*, 3375–3378.
(46) Zeglis, B. M.; Sevak, K. K.; Reiner, T.; Mohindra, P.; Carlin, S. D.; Zanzonico, P.; Weissleder, R.; Lewis, J. S. A Pretargeted PET Imaging Strategy Based on Bioorthogonal Diels – Alder Click Chemistry. *J. Nucl. Med.* **2013**, *54*, 1389–1396.
(47) Cook, B. E.; Adumeau, P.; Membreno, R.; Carnazza, K. E.; Brand, C.; Reiner, T.; Agnew, B. J.; Lewis, J. S.; Zeglis, B. M. Pretargeted PET Imaging Using a Site-Specifically Labeled Immunoconjugate. *Bioconjug. Chem.* **2016**, *27*, 1789–1795.
(48) Adumeau, P.; Carnazza, K. E.; Brand, C.; Carlin, S. D.; Reiner, T.; Agnew, B. J.; Lewis, J. S.; Zeglis, B. M. A Pretargeted Approach for the Multimodal PET/NIRF Imaging of Colorectal Cancer. *Theranostics* **2016**, *6*, 2267–2277.
(49) Rossin, R.; Läppchen, T.; Van Den Bosch, S. M.; Laforest, R.; Robillard, M. S. Diels–Alder Reaction for Tumor Pretargeting: In Vivo Chemistry Can Boost Tumor Radiation Dose Compared with Directly Labeled Antibody. *J. Mol. Med.* **2013**, *54*, 1989–1995.
(50) Rossin, R.; Van Duijnhoven, S. M. J.; Läppchen, T.; Van Den Bosch, S. M.; Robillard, M. S. Trans-Cyclooctene Tag with Improved Properties for Tumor Pretargeting with the Diels-Alder Reaction. *Mol. Pharm.* **2014**, *11*, 3090–3096.
(51) van Duijnhoven, S. M. J.; Rossin, R.; van den Bosch, S. M.; Wheatcroft, M. P.; Hudson, P. J.; Robillard, M. S. Diabody Pretargeting with Click Chemistry In Vivo. *J. Nucl. Med.* **2015**, *56*, 1422–1428.
(52) Altai, M.; Perols, A.; Tsourma, M.; Mitran, B.; Honarvar, H.; Robillard, M.; Rossin, R.; ten Hoeve, W.; Lubberink, M.; Orlova, A.; Karlström, A. K.; Tolmachev, V. Feasibility of Affibody-Based Bioorthogonal Chemistry-Mediated Radionuclide Pretargeting. *J. Nucl. Med.* **2016**, *57*, 431–436.
(53) Zeglis, B. M.; Brand, C.; Abdel-Atti, D.; Carnazza, K. E.; Cook, B. E.; Carlin, S.; Reiner, T.; Lewis, J. S. Optimization of a Pretargeted Strategy for the PET Imaging of Colorectal Carcinoma via the Modulation of Radioligand Pharmacokinetics. *Mol. Pharm.* **2015**, *12*, 3575–3587.
(54) Koo, H.; Lee, J. H.; Bao, K.; Wu, Y.; El Fakhri, G.; Henary, M.; Yun, S. H.; Choi, H. S. Site-Specific In Vivo Bioorthogonal Ligation via Chemical Modulation. *Adv. Healthc. Mater.* **2016**, *5*, 2510–2516.

(55) Devaraj, N. K.; Thurber, G. M.; Keliher, E. J.; Marinelli, B.; Weissleder, R. Reactive Polymer Enables Efficient in Vivo Bioorthogonal Chemistry. *Proc. Natl. Acad. Sci.* **2012**, *109*, 4762–4767.
(56) Devaraj, N. K.; Hilderbrand, S.; Upadhyay, R.; Mazitschek, R.; Weissleder, R. Bioorthogonal Turn-On Probes for Imaging Small Molecules inside Living Cells. *Angew. Chem. Int. Ed.* **2010**, *49*, 2869–2872.
(57) Carlson, J. C. T.; Meimetis, L. G.; Hilderbrand, S. A.; Weissleder, R. BODIPY–Tetrazine Derivatives as Superbright Bioorthogonal Turn-on Probes. *Angew. Chem. Int. Ed.* **2013**, *52*, 6917–6920.
(58) Meimetis, L. G.; Boros, E.; Carlson, J. C.; Ran, C.; Caravan, P.; Weissleder, R. Bioorthogonal Fluorophore Linked DFO - Technology Enabling Facile Chelator Quantification and Multimodal Imaging of Antibodies. *Bioconjug. Chem.* **2015**, *27*, 257–263.
(59) Houghton, J. L.; Zeglis, B. M.; Abdel-Atti, D.; Sawada, R.; Scholz, W. W.; Lewis, J. S. Pretargeted Immuno-PET of Pancreatic Cancer: Overcoming Circulating Antigen and Internalized Antibody to Reduce Radiation Doses. *J. Nucl. Med.* **2016**, *57*, 453–459.
(60) Meyer, J. P.; Houghton, J. L.; Kozlowski, P.; Abdel-Atti, D.; Reiner, T.; Pillarsetty, N. V. K.; Scholz, W. W.; Zeglis, B. M.; Lewis, J. S. 18F-Based Pretargeted PET Imaging Based on Bioorthogonal Diels-Alder Click Chemistry. *Bioconjug. Chem.* **2016**, *27*, 298–301.
(61) Emmetiere, F.; Irwin, C.; Viola-Villegas, N. T.; Longo, V.; Cheal, S. M.; Zanzonico, P.; Pillarsetty, N.; Weber, W. A.; Lewis, J. S.; Reiner, T. 18 F-Labeled-Bioorthogonal Liposomes for In Vivo Targeting. *Bioconjug. Chem.* **2013**, *24*, 1784–1789.
(62) Tang, L.; Yin, Q.; Xu, Y.; Zhou, Q.; Cai, K.; Yen, J.; Dobrucki, L. W.; Cheng, J. Bioorthogonal Oxime Ligation Mediated in Vivo Cancer Targeting. *Chem. Sci.* **2015**, *6*, 2182–2186.
(63) Hou, S.; Choi, J. S.; Garcia, M. A.; Xing, Y.; Chen, K. J.; Chen, Y. M.; Jiang, Z. K.; Ro, T.; Wu, L.; Stout, D. B.; Tomlinson, J. S.; Wang, H.; Chen, K.; Tseng, H.-R.; Lin, W.-Y. Pretargeted Positron Emission Tomography Imaging That Employs Supramolecular Nanoparticles with in Vivo Bioorthogonal Chemistry. *ACS Nano* **2016**, *10*, 1417–1424.
(64) Lee, S. B.; Kim, H. L.; Jeong, H. J.; Lim, S. T.; Sohn, M. H.; Kim, D. W. Mesoporous Silica Nanoparticle Pretargeting for PET Imaging Based on a Rapid Bioorthogonal Reaction in a Living Body. *Angew. Chem. Int. Ed.* **2013**, *52*, 10549–10552.
(65) Denk, C.; Svatunek, D.; Mairinger, S.; Stanek, J.; Filip, T.; Matscheko, D.; Kuntner, C.; Wanek, T.; Mikula, H. Design, Synthesis, and Evaluation of a Low-Molecular-Weight 11C-Labeled Tetrazine for Pretargeted PET Imaging Applying Bioorthogonal in Vivo Click Chemistry. *Bioconjug. Chem.* **2016**, *27*, 1707–1712.
(66) Keinänen, O.; Mäkilä, E. M.; Lindgren, R.; Virtanen, H.; Liljenbäck, H.; Oikonen, V.; Sarparanta, M.; Molthoff, C.; Windhorst, A. D.; Roivainen, A.; Salonen, J. J.; Airaksinen, A. J. Pretargeted PET Imaging of Trans-Cyclooctene-Modified Porous Silicon Nanoparticles. *ACS Omega* **2017**, *2*,

62–69.
(67) Van Brakel, R.; Vulders, R. C. M.; Bokdam, R. J.; Grüll, H.; Robillard, M. S. A Doxorubicin Prodrug Activated by the Staudinger Reaction. *Bioconjug. Chem.* **2008**, *19*, 714–718.
(68) Versteegen, R. M.; Rossin, R.; Ten Hoeve, W.; Janssen, H. M.; Robillard, M. S. Click to Release: Instantaneous Doxorubicin Elimination upon Tetrazine Ligation. *Angew. Chem. Int. Ed.* **2013**, *52*, 14112–14116.
(69) Rossin, R.; Van Duijnhoven, S. M. J.; Ten Hoeve, W.; Janssen, H. M.; Kleijn, L. H. J.; Hoeben, F. J. M.; Versteegen, R. M.; Robillard, M. S. Triggered Drug Release from an Antibody-Drug Conjugate Using Fast "Click-to-Release" Chemistry in Mice. *Bioconjug. Chem.* **2016**, *27*, 1697–1706.
(70) Mejía Oneto, J. M.; Gupta, M.; Leach, J. K.; Lee, M.; Sutcliffe, J. L. Implantable Biomaterial Based on Click Chemistry for Targeting Small Molecules. *Acta Biomater.* **2014**, *10*, 5099–5105.
(71) Mejia Oneto, J. M.; Khan, I.; Seebald, L.; Royzen, M. In Vivo Bioorthogonal Chemistry Enables Local Hydrogel and Systemic Pro-Drug To Treat Soft Tissue Sarcoma. *ACS Cent. Sci.* **2016**, *2*, 476–482.
(72) Houghton, J. L.; Membreno, R.; Abdel-Atti, D.; Cunanan, K. M.; Carlin, S.; Scholz, W. W.; Zanzonico, P. B.; Lewis, J. S.; Zeglis, B. M. Establishment of the In Vivo Efficacy of Pretargeted Radioimmunotherapy Utilizing Inverse Electron Demand Diels-Alder Click Chemistry. *Mol. Cancer Ther.* **2017**, *16*, 124–133.
(73) Clavadetscher, J.; Hoffmann, S.; Lilienkampf, A.; Mackay, L.; Yusop, R. M.; Rider, S. A.; Mullins, J. J.; Bradley, M. Copper Catalysis in Living Systems and In Situ Drug Synthesis. *Angew. Chem. Int. Ed.* **2016**, *55*, 15662–15666.

Chapter 2

Bioorthogonal Imaging of Cancer-Associated Sialic Acid in Embryonic Zebrafish

Chapter 2. Bioorthogonal Imaging of Cancer-Associated Sialic Acid in Embryonic Zebrafish

Introduction

Sialic acid is ubiquitous on the surface of vertebrate cells, where it typically occupies the terminal position of cell surface glycans and is well-poised for interaction in the extracellular domain.[1] Accordingly, sialylated glycans play crucial roles in mediating processes such as cell adhesion, extracellular recognition, and signaling.[2] These critical functions are often commandeered by cancer cells to enhance their survival and invasivity.[3–8] It is no surprise then, that of the many glycosylation changes that accompany cancer onset, overexpression of cell surface sialic acid is among the most widespread.[9] A number of recent reviews have documented the contribution of hypersialylation to malignant progression.[10–12] As a result, methods to target sialic acid are highly valued for cancer research and therapeutic development.[13–15]

Glycan biosynthesis is not directly encoded by the genome, barring the use of fluorescent protein tags to study sialylation.[16] Historically, sialic acid-binding lectin-based assays have been employed, though they often lack sensitivity and are not easily translatable to complex animal models, hindering studies in physiologically relevant environments.[17] Due to these shortcomings, novel chemical approaches have been adopted for the direct targeting of sialic acid. In particular, metabolic bioorthogonal labeling has achieved success in tagging sialic acid residues both in cell culture and in animal models.[18] Briefly, an azide-modified variant of *N*-acetylmannosamine (ManNac), is administered to cells. *N*-azidoacetylmannosamine (ManNAz) is converted by the cell's biosynthetic machinery to azidosialic acid and displayed on cell surface glycans, where it can undergo a copper-free click reaction with a fluorescent cyclooctyne probe (Figure 2.1). This and similar strategies have enabled the imaging of sialic acid on cancer cells in culture and even in mice.[19–22]

To accurately capture the cancer disease state, it is necessary to perform studies in animal models, where interactions with the host can be recreated. As mentioned, tumors in mice have been successfully labeled using metabolically incorporated azidosugars and bioorthogonal imaging probes (see Chapter 1 for an in-depth review). Unfortunately, due to a combination of low azidosugar incorporation efficiency and poor probe pharmacokinetic properties, studies in mice have been plagued by low selectivity and high background labeling.[20,23,24] Even more importantly, mouse models generally present obstructions to optical imaging. Absorption and scattering of light by tissue limits imaging depth to single millimeters and prevents sensitive imaging on the cellular scale,[25] which is required to observe potentially subtle changes in sialic acid distribution on individual cancer cells. Window chamber and intraoperative imaging techniques can combat these limitations, but require immense expertise and less accurately portray the natural physiological conditions.[26] Two-photon excitation increases imaging depth somewhat, but must often be employed in concert with surgical

techniques.[27] Nuclear imaging provides unlimited tissue penetrance, but lacks the spatial resolution for studies and on the cellular and subcellular scales.[28]

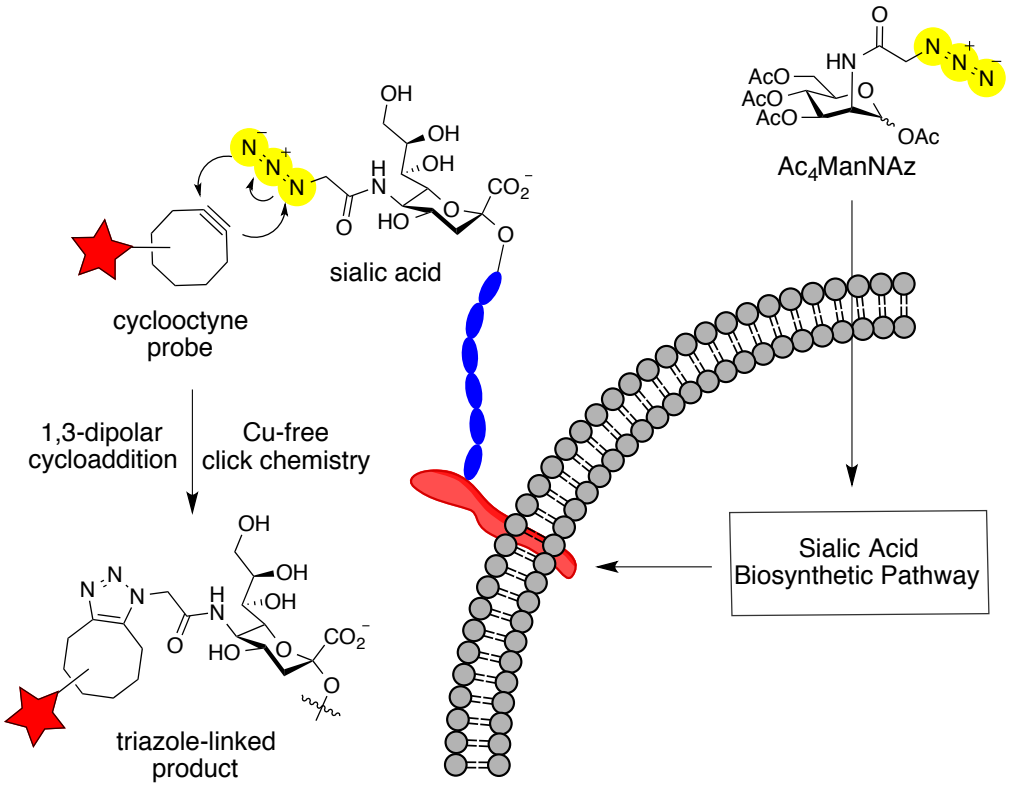

Figure 2.1. Metabolic bioorthogonal labeling of sialic acid using copper-free click chemistry.

The embryonic zebrafish provides an alternative to mouse models, especially with regard to imaging. Zebrafish can be kept optically translucent throughout early development, making them ideal for fluorescence microscopy. Advantageously, naturally occurring zebrafish cancers closely resemble human cancers on a genetic and histological level and recent years have seen embryonic zebrafish established as an increasingly utilized model for cancer.[29] Studies using both spontaneous and xenograft tumor models in zebrafish have reported the detailed observation of various aspects of cancer progression, including angiogenesis, migration, extravasation dynamics, and immune cell interactions, all on the cellular level.[30–35] To study cancer sialylation as it relates to disease, xenograft models using human cancer cell lines are particularly attractive, and a multitude of different cell lines have been applied for both systemic and localized tumor models in zebrafish. In addition, zebrafish embryos are highly amenable to study using a wide variety of fluorescent probes.[36] Metabolic bioorthogonal chemistry has accomplished the labeling and imaging of

sialic acid in zebrafish, both externally and systemically, through the incorporation of synthetic sugar analogs.[37,38]

Inspired by the tractability of the embryonic zebrafish for both bioorthogonal labeling and investigating cancer dynamics on a cellular basis, we sought to implement it as a model for the molecular imaging of cancer-associated sialylation. This chapter describes the use of different bioorthogonal chemistries to image sialic acid in a zebrafish xenograft model of cancer. This approach enabled the imaging of cancer on the subcellular scale with greater sensitivity than has been achieved in mice, and sets a foundation for the continued study of cancer sialylation in embryonic zebrafish.

Results and Discussion

Evaluation of ManNAz incorporation in cancer cell lines

Our principle aim was to establish methods for the bioorthogonal labeling of cancer-associated sialic acid in zebrafish. The ability to directly image sialylation with high sensitivity *in vivo* would provide an improved understanding of sialic acid distribution and dynamics throughout various stages of cancer progression. In a similar application, bioorthogonal labeling could be used to survey the overall sialic acid content of individual cells and how it impacts the behavior of differentially sialylated tumor cell subpopulations. Our experimental design is outlined in Figure 2.2. Cancer cells in culture are incubated with Ac_4ManNAz to ensure efficient incorporation into sialylated glycans. Cells are then transplanted into zebrafish embryos at 48 hours post fertilization (hpf) using a variety of injection sites to explore both localized and systemic xenografts. Subsequent administration of a cyclooctyne probe at various timepoints allows for the assessment of ManNAz-dependent labeling of cancer cells.

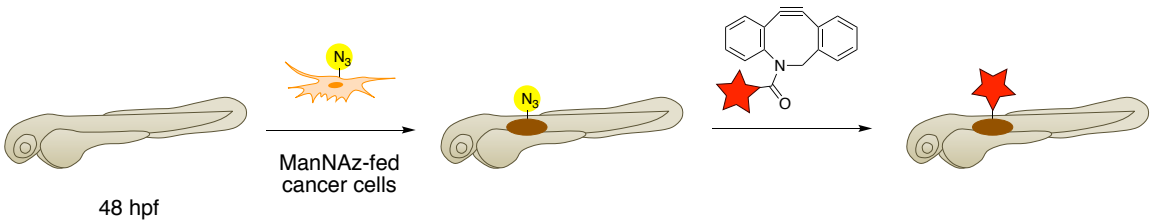

Figure 2.2. Copper-free click labeling of cancer-associated sialic acid in zebrafish.

First, several different human cancer cell lines were evaluated for ManNAz incorporation *in vitro* by reaction with DIBAC-Cy5 after azidosugar treatment. Prostate cancer cell lines PC3, DU145, and LNCaP, and leukemia cell lines Jurkat and K562, were chosen for their reported use in zebrafish xenografts.[39,40]

After incubation with 50 μM Ac_4ManNAz for three days, these cell lines were found to significantly incorporate azidosugar to varying degrees. Data for prostate cancer cell lines is presented in Figure 2.3.

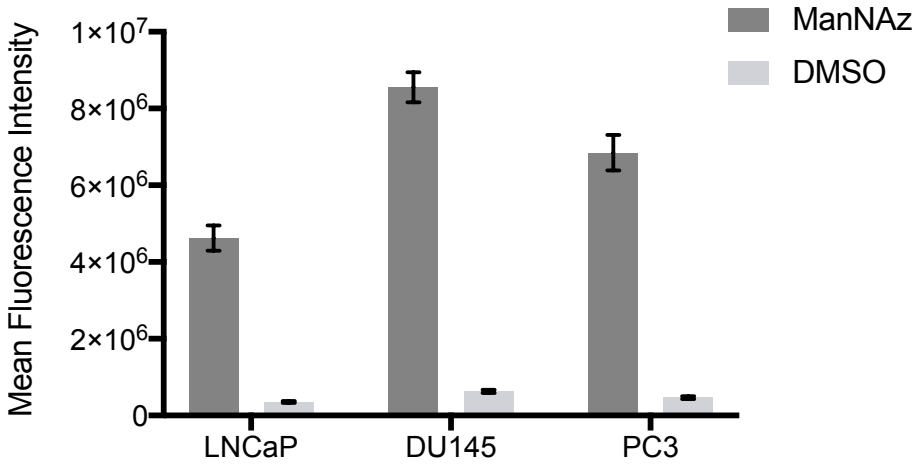

Figure 2.3. ManNAz incorporation in prostate cancer cell lines. Cells were incubated in media containing 50 μM Ac_4ManNAz or DMSO vehicle control for 3 d and labeled with DIBAC-Cy5. Errors bars represent SD (n=3).

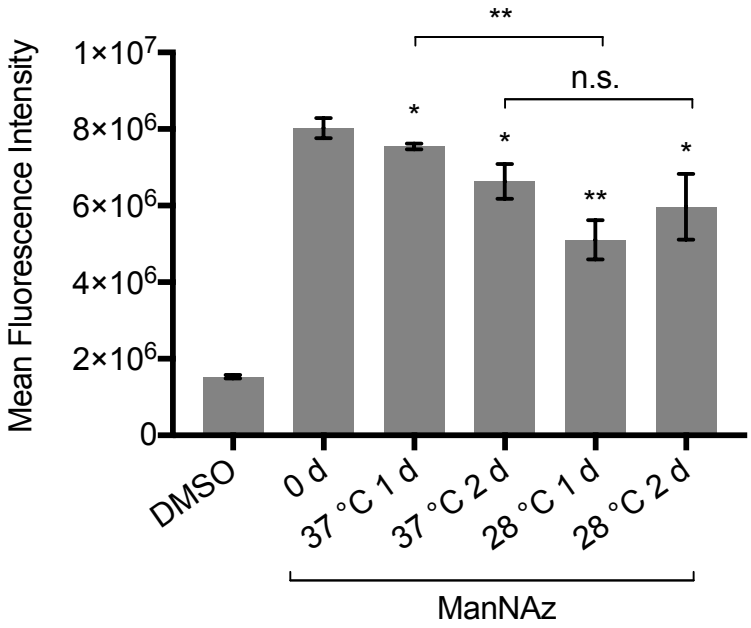

Figure 2.4. Cell surface residence time of ManNAz in DU145 cells. Cells were incubated in media containing 50 μM Ac_4ManNAz or DMSO vehicle control for 3 d prior to incubation in azidosugar-free media for 1 or 2 d, and labeled with DIBAC-Cy5. Errors bars represent SD (n=3). *p < 0.05, **p < 0.005.

The azidosugar duration on the cell surface was also measured to determine suitable timepoints for administration of cyclooctyne probes. After ManNAz-treatment, DU145 cells were incubated in azidosugar-free media for a two-day period and assayed for reactivity with DIBAC-Cy5 (Figure 2.4). Cells incubated at 37 °C exhibited only a modest decrease in labeling efficiency, retaining approximately 80% of the initial signal two days after azidosugar withdrawal, indicating that the loss of cell surface azide content is quite slow. Because cells within a zebrafish are subject to stresses including reduced temperature, this assay was also performed at 28 °C. Cells in this case initially displayed a greater loss of labeling, though still retained a significant amount ManNAz-depdendent signal over the vehicle control. Unsurprisingly, cells incubated at 28 °C showed compromised viability, which may account for differences in azidosugar residence time.

Bioorthogonal labeling in a systemic xenograft model of metastasis

With ManNAz-incorporation validated for several cell lines, preliminary studies focused on the choice of transplantation site in zebrafish. For visualization, cells were stained with CellTracker Green CMFDA immediately prior to injection. Many different sites can be used for injection, resulting in different distribution patterns throughout the embryo.[41] It has been observed that cancer cells injected into the yolk sac at 48 hpf can migrate to distal regions of the fish.[42] In contrast, the cell lines tested here remained restricted within the yolk, with very few instances of invasion into surrounding tissue (Figure 2.5). A systemic xenograft was adopted instead, in which cells injected ventral to the yolk sac near the sinus venosus disseminated throughout the embryo. This model was deemed more appropriate as cells within the vasculature would have superior access to reactive probes injected into the circulation. A similar result was noted for leukemic cells injected intravascularly into the caudal vein (Figure 2.6). To encourage cancer cell viability, zebrafish were maintained at 32 °C after transplantation, as this temperature allows for survival of both human cells and zebrafish in xenograft models.[40] In accordance with previous reports,[39] the persistence of cancer cell burden in the embryo correlated with metastatic potential (Figure 2.7), as observed with poorly metastatic LNCaP cells being cleared more rapidly than highly metastatic PC3 cells, and DU145 showing an intermediate distribution. On this basis, subsequent studies primarily utilized PC3 and DU145 cells.

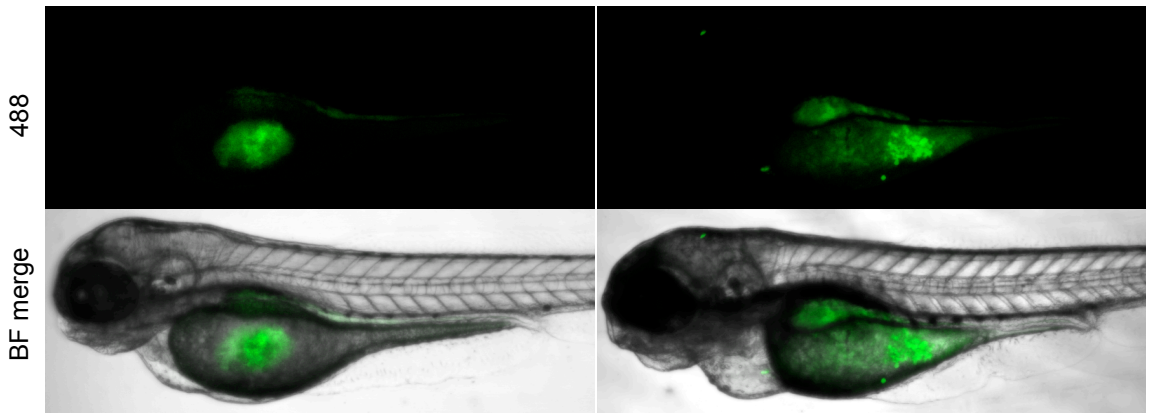

Figure 2.5. Yolk injection of DU145 cells. Representative images of zebrafish injected into the yolk at 48 hpf with DU145 cells (stained with CellTracker Green). Images were taken at 96 hpf.

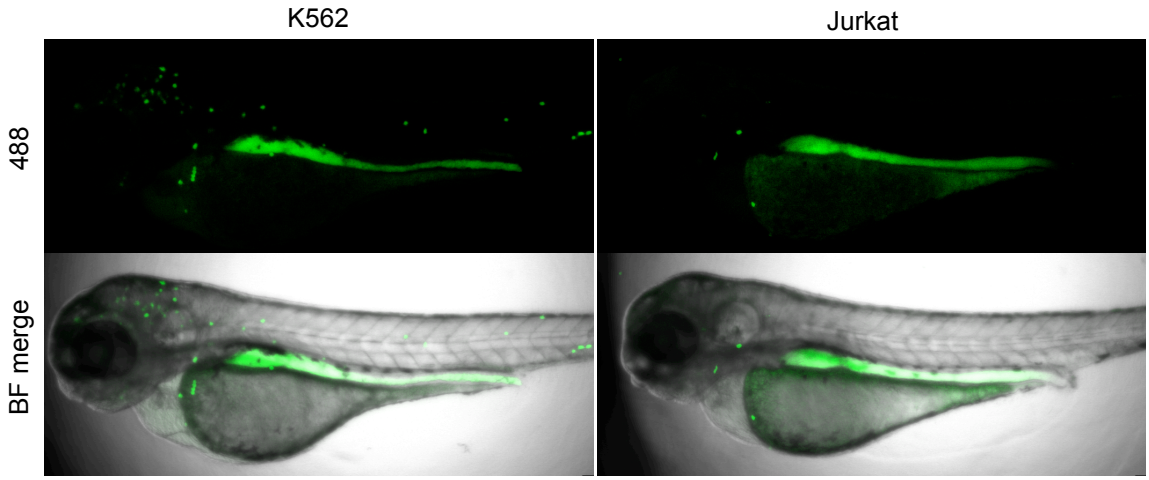

Figure 2.6. Caudal vein injection of leukemia cell lines. Representative images of zebrafish injected into the caudal vein at 48 hpf with K562 and Jurkat cells (stained with CellTracker Green). Images were taken at 96 hpf.

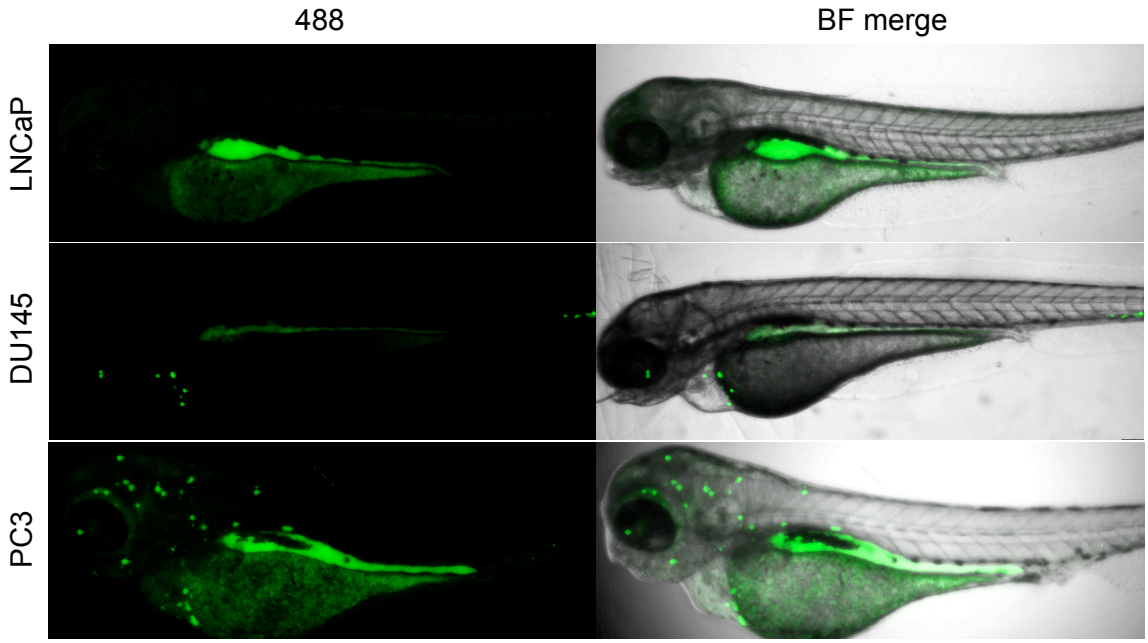

Figure 2.7. Zebrafish model of metastasis through systemic administration of prostate cancer cells. Representative images of zebrafish injected ventral to the yolk near the sinus venosus at 48 hpf with LNCaP, DU145, or PC3 cells (stained with CellTracker Green). Images taken at 96 hpf show cancer distribution.

With a suitable xenograft model in hand, we sought to assess bioorthogonal labeling *in vivo*. PC3 and DU145 cells were incubated with 50 μM Ac_4ManNAz and injected near the sinus venosus at 48 hpf, as before. After a 24 hour waiting period to ensure the clearance of cells that had died before or during the injection procedure, 500 μM DIBAC-Cy5 was administered by caudal vein injection. After another 24 hour interval to allow unreacted cyclooctyne probe to clear, fluorescence imaging detected no observable ManNAz-dependent labeling of cancer cells (Figure 2.8). Increasing or decreasing the concentration of cyclooctyne probe did not produce any selective labeling (data not shown). Similar results were obtained with DU145 and Jurkat cells (Figure 2.9). The lack of labeling can likely be attributed to a combination of multiple possible factors, e.g., insufficient azide incorporation, poor probe access to the cancer cell surface, and high background. High intensity Cy5 fluorescence signaling localized to the pronephric duct, the zebrafish premature kidney,[43] indicates that unreacted probe is indeed being cleared, though significant amounts remain systemically. Background fluorescence is particularly evident in the ventral tail.

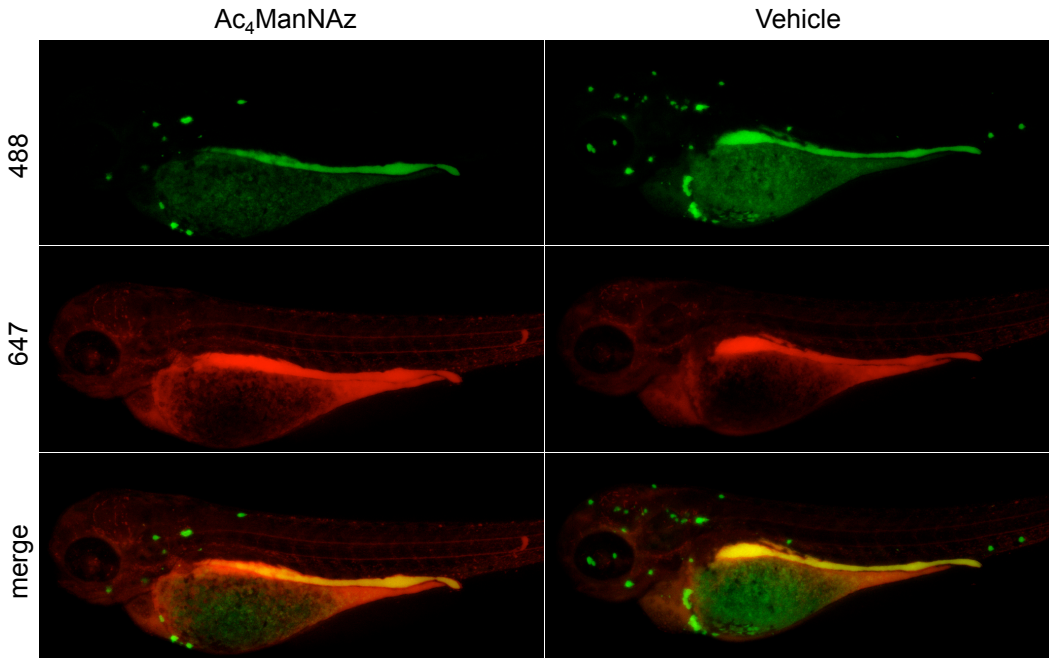

Figure 2.8. *In vivo* copper-free click labeling is not observed for cancer cells treated with 50 μM Ac_4ManNAz. PC3 cells (488) were incubated with 50 μM Ac_4ManNAz for 3 d prior to systemic injection at 48 hpf. DIBAC-Cy5 (647) was injected at 72 hpf. Imaging was performed at 96 hpf.

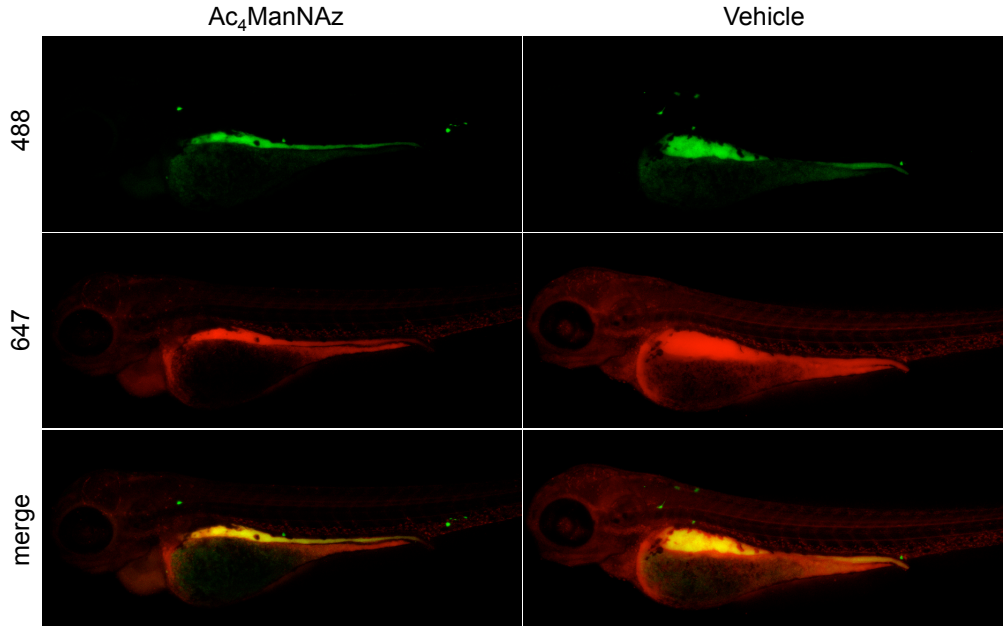

Figure 2.9. Copper-free click labeling in a leukemia xenograft. Jurkat cells (488) were incubated with 50 μM Ac_4ManNAz for 3 d prior to systemic injection at 48 hpf. DIBAC-Cy5 (647) was injected at 72 hpf. Imaging was performed at 96 hpf.

Optimization of ManNAz concentration enables selective copper-free click labeling in vivo

Although cells incubated with 50 μM Ac_4ManNAz in culture label robustly with cyclooctyne probes, high levels of nonselective background labeling appear to be an issue in zebrafish. To determine if contrast could be enhanced through greater azidosugar incorporation, PC3 cells treated with 200 μM Ac_4ManNAz were injected into zebrafish and labeled with DIBAC-Cy5 as before. Gratifyingly, injection of 1 mM DIBAC-Cy5 immediately following cancer cell transplantation resulted in detectable ManNAz-dependent labeling of cells in the head and tail region, as determined by imaging within an hour of probe administration (Figure 2.10). Imaging of the same embryos performed after a 24 hour clearance time revealed selective labeling that appeared to be higher in intensity at the cell surface (Figure 2.11). Fluorescence intensity measurement across the length of the cell confirms preferential labeling at the periphery (Figure 2.11B). The observed intracellular signal may arise from internalization of labeled cell surface sialylated proteins, as DIBAC-Cy5 itself is trisulfonated and unlikely to pass through cell membranes. Introduction of DIBAC-Cy5 24 hours after cancer cell injection also resulted in selective labeling, although a signal distribution resembling cell surface localization was not observed in this case (Figure 2.12).

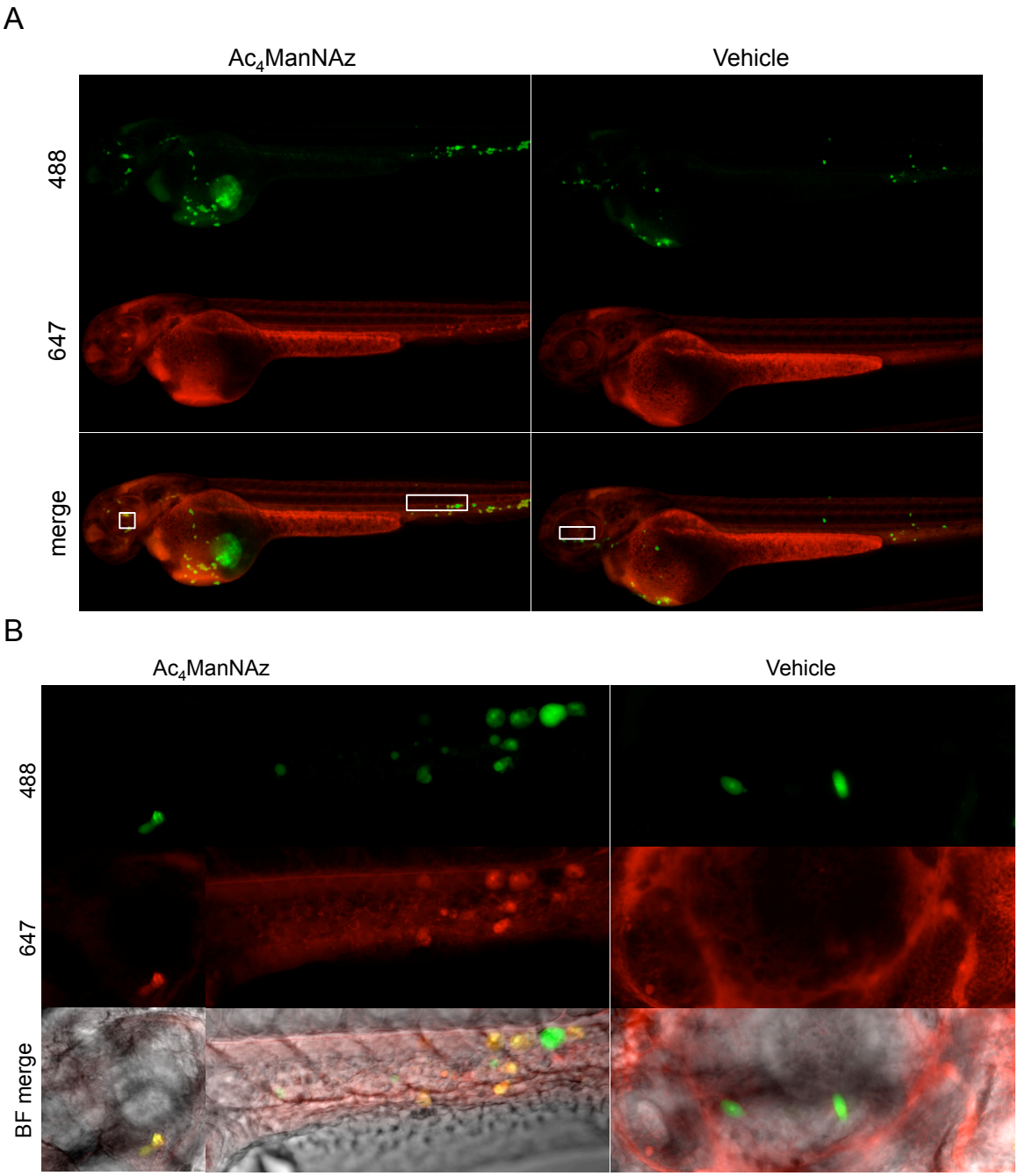

Figure 2.10. Higher concentrations of ManNAz enable copper-free click labeling *in vivo*. A) PC3 cells (488) treated with 200 μM Ac_4ManNAz 3 d injected at 48 hpf followed by DIBAC-Cy5 (647). Imaging performed immediately after DIBAC injection at 4x magnification. B) Zoom images of samples in A (white boxes) taken at 20x magnification.

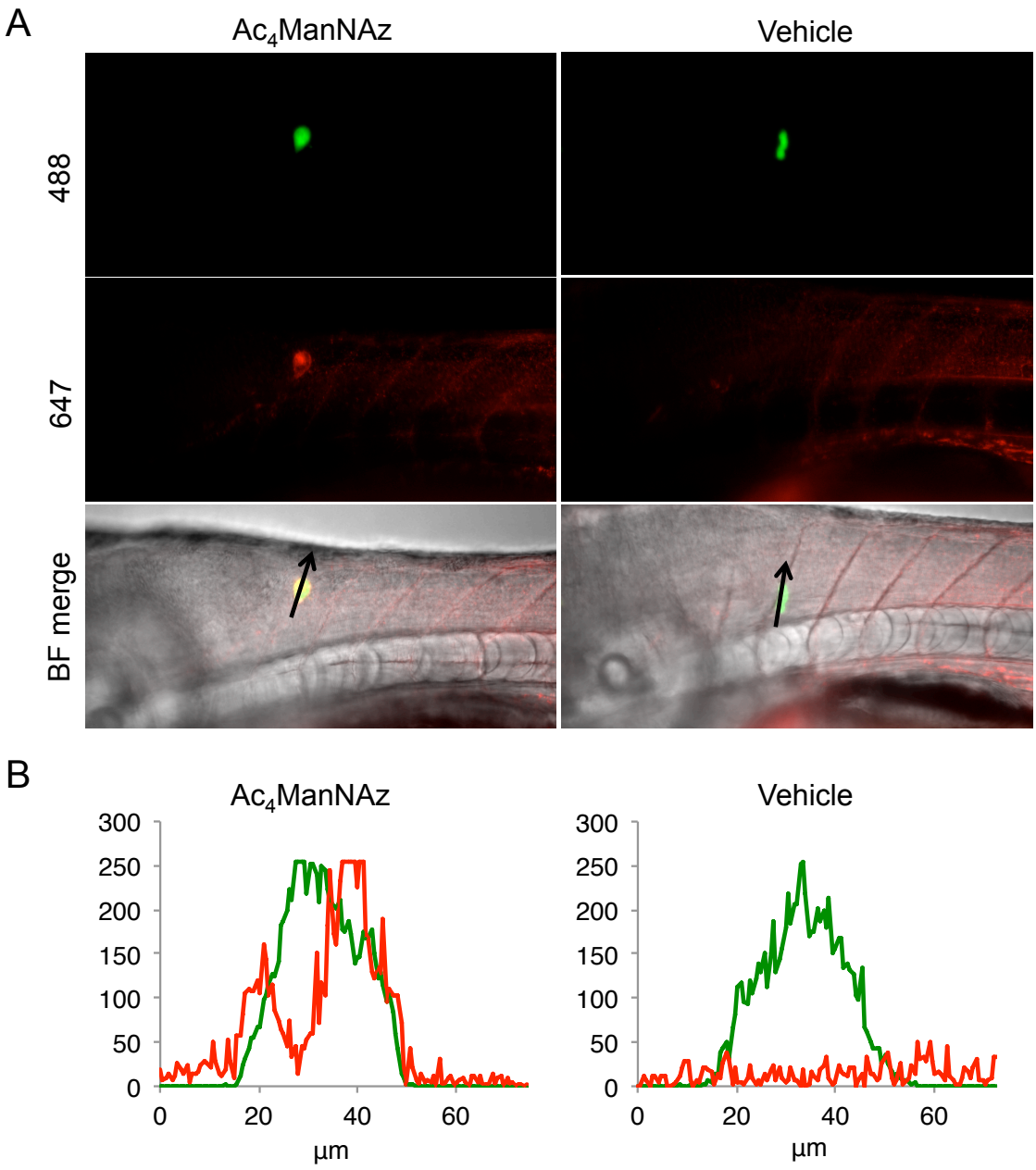

Figure 2.11. Copper-free click labeling in zebrafish is localized to the cell surface. A) PC3 cells (488) treated with 200 µM Ac_4ManNAz 3 d injected at 48 hpf followed by DIBAC-Cy5 (647). Imaging performed at 84 hpf. B) Fluorescence intensity (y-axis) of a single Z-slice correlated with distance across the arrow indicated in A. Green, CellTracker Green signal; red, DIBAC-Cy5 signal.

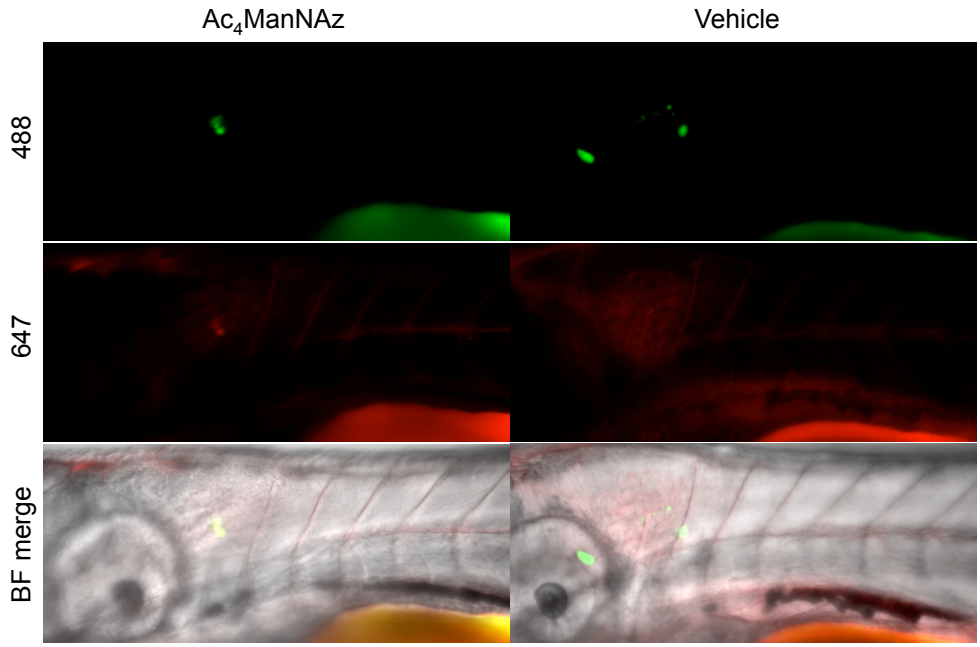

Figure 2.12. Copper-free click enables labeling 24 h after cancer cell introduction. PC3 cells (488) treated with 200 μM Ac_4ManNAz 3 d injected at 48 hpf. DIBAC-Cy5 (647) injected at 72 hpf. Imaging performed at 84 hpf.

The same approach was applied to DU145 xenografts, where it was found that 100 μM Ac_4ManNAz was sufficient to achieve highly robust cell surface labeling (Figure 2.13). Approximately a 20-fold enhancement in Cy5 signal was observed for ManNAz-treated cells compared to vehicle controls in the eye and tail regions. We noted that labeling was only observed for a small portion of total cells present (Figure 2.14), impeding a thorough statistical analysis. High levels of background, particularly in the caudal vein, may obfuscate labeling.

Aside from high background, we surmised that the lack of consistent levels of labeling amongst different cells within the same embryo might also be due to differential probe access, where certain cells might be more advantageously positioned within the vasculature for interaction with cyclooctyne probes. To address this concern, we pursued a localized xenograft model where probe access should be more uniform. Cancer cells injected into the hindbrain at 48 hpf remained there for the duration of the study, where they were labeled with systemically administered DIBAC-Cy5 (Figure 2.15). Two concentrations, 1 mM and 0.5 mM, of DIBAC-Cy5 were tested to determine if a lower amount would reduce background and create a more favorable signal-to-noise ratio. On the contrary, a higher concentration yielded more robust labeling overall as well as higher signal over background (Figure 2.15B). ManNAz incorporation enabled the detection of apparent cell surface localized signal, and the observation of projections stemming from individual cancer cells, the nature of which has yet to be elucidated. Taken together, these results establish proof-of-principle for labeling cancer cells in zebrafish using copper-free click chemistry.

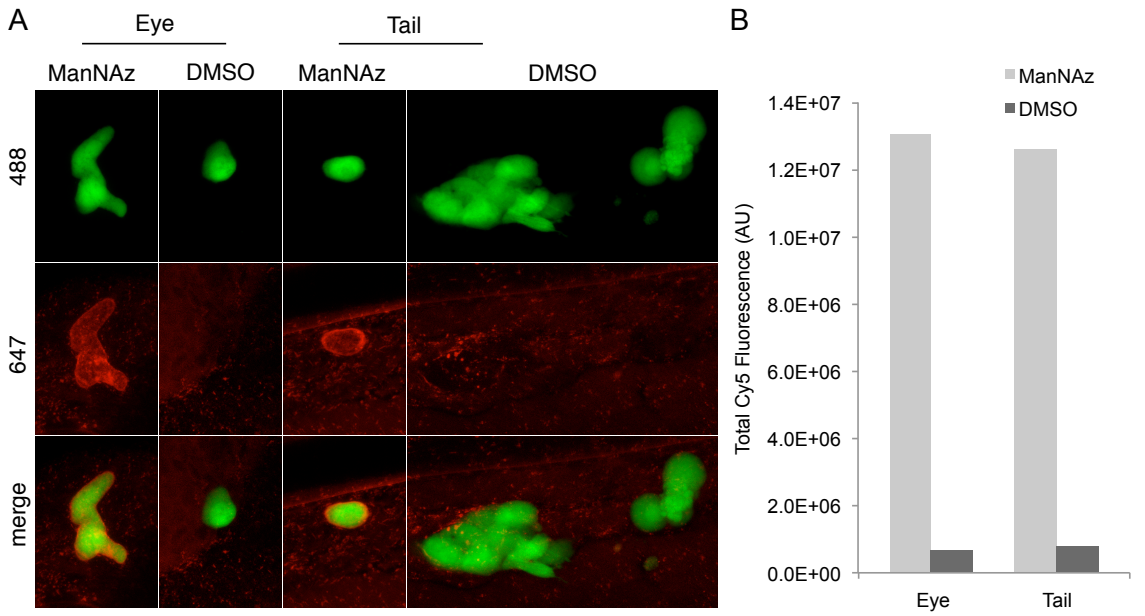

Figure 2.13. Robust cell surface labeling is observed in DU145 cells *in vivo*. A) Images of the eye and tail regions for DU145 cells (488) treated with 100 μM Ac_4ManNAz 3 d. DIBAC-Cy5 (647) was injected at 72 hpf followed by imaging. B) Quantification of labeling determined by the total Cy5 fluorescence localized to cancer cells as calculated using Imaris x64.

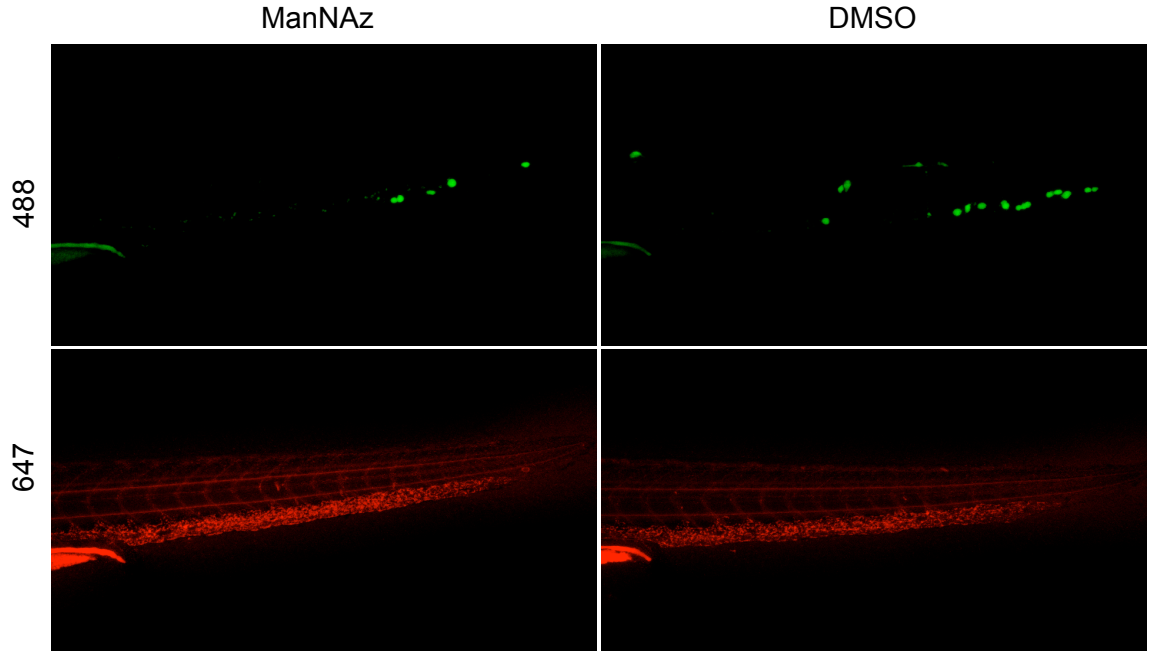

Figure 2.14. Copper-free click chemistry yields high background and low labeling consistency. Tail images of embryos injected and imaged as in Figure 2.13.

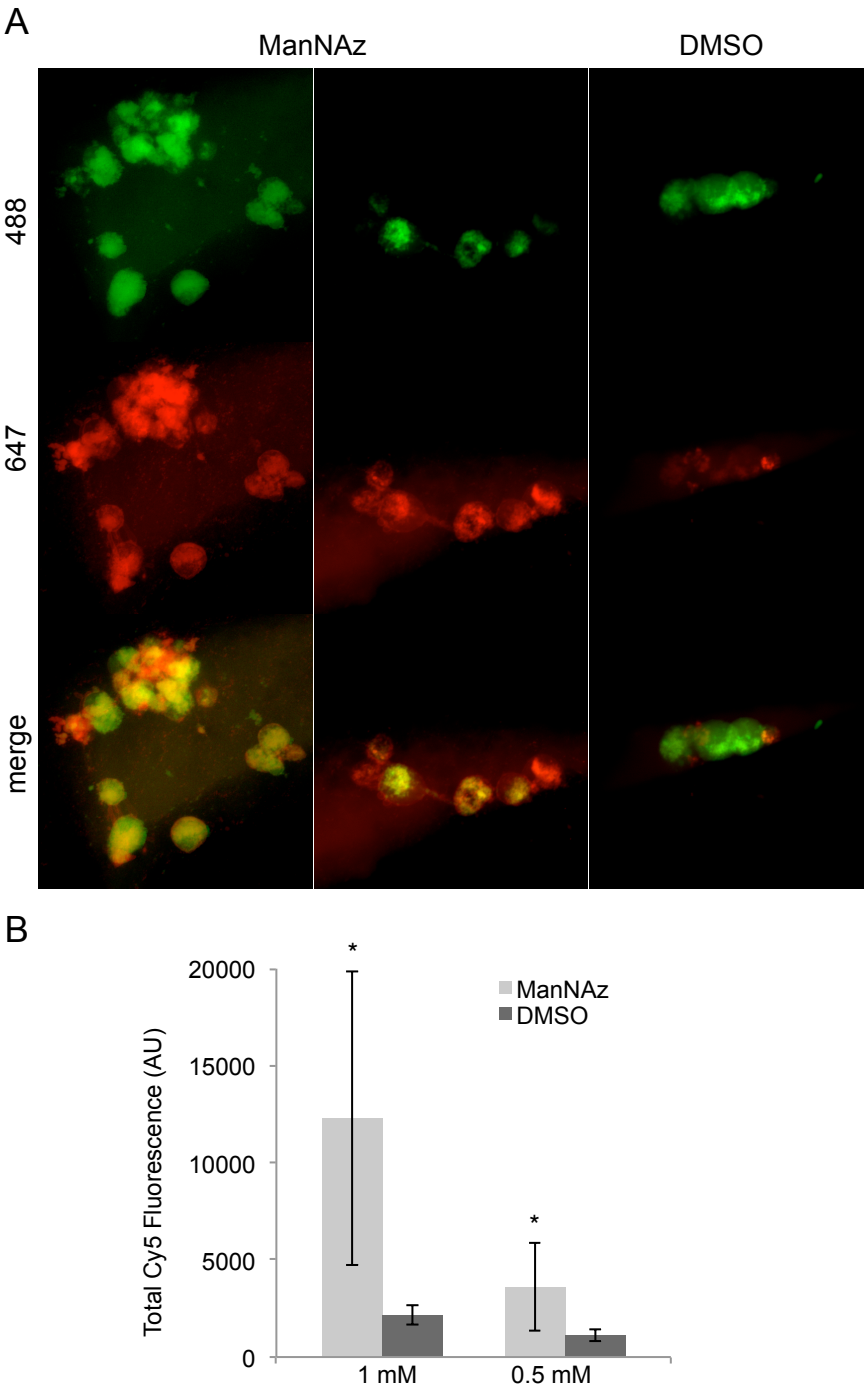

Figure 2.15. Copper-free click labeling in a hindbrain xenograft. A) Hindbrain images of fish injected with DU145 cells incubated with 100 μM Ac_4ManNAz. DIBAC-Cy5 was administered systemically at 72 hpf prior to imaging. B) Quantification of labeling determined by the total Cy5 fluorescence localized to cancer cells as calculated using Imaris x64. Error bars represent SD (n=4-6). *$p < 0.05$.

ManNAz lowers cancer cell viability in zebrafish

While copper-free click accomplished the selective cell surface labeling of cancer cells in a zebrafish model, this approach faces noteworthy limitations. Aside from high levels of background observed, we noted qualitatively in various studies that ManNAz-treated cells show attenuated viability *in vivo* compared to vehicle-treated cells. To better characterize this phenomenon, the effect of ManNAz on PC3 viability was investigated. In culture, ManNAz exhibited slight dose-dependent toxicity, with 100 μM resulting in a 10% decrease in viability (Figure 2.16). For a comparison with the *in vivo* effect, PC3 cells incubated with 100 μM Ac_4ManNAz were injected systemically at 48 hpf and monitored for persistence over a 2 day period (Figure 2.17). Our findings indicate that ManNAz-treatment induces a sizeable reduction in cell survival of about half by 1 day post injection (dpi). The difference is exacerbated by day 2. Interestingly, no change in survival was observed for control cells between days 1 and 2. This suggests that the initial drop in viability (control cells exhibit only 43% survival by 1 dpi) may be due to stresses experienced during the microinjection protocol. In contrast, the observation of continued clearance through 2 dpi for ManNAz-treated cells indicates that this cell death is mediated by a different mechanism. In mammalian systems, sialic acid contributes to cancer cell survival both by disrupting programmed cell death pathways and suppressing the host immune response.[3,4,7,8,44] It is feasible that similar mechanisms exist within zebrafish, and that azide-modifications to sialic acid residues might interfere with native sialic acid-recognition processes. This is a topic of ongoing research. Given that cells in culture did not display the same magnitude of viability loss, it is likely that this effect was not caused by nonspecific ManNAz cytotoxicity alone.

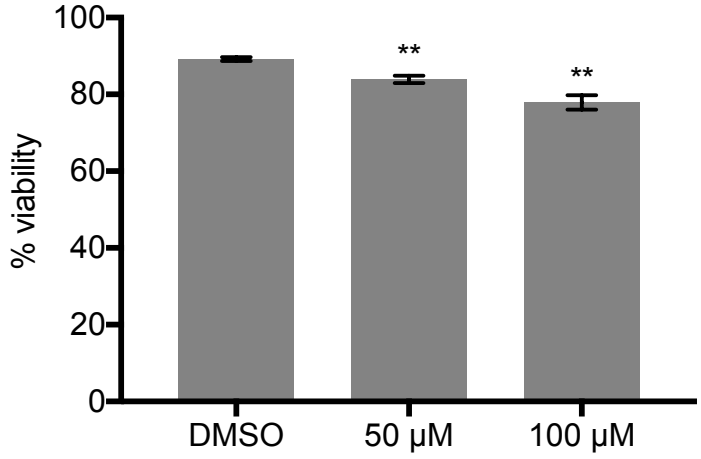

Figure 2.16. *In vitro* viability of ManNAz-treated PC3 cells. PC3 cells were incubated with Ac_4ManNAz for 3 d at the indicated concentrations. Viability was determined by a calcein AM/ethidium homodimer-1 live/dead cell assay. **p < 0.005.

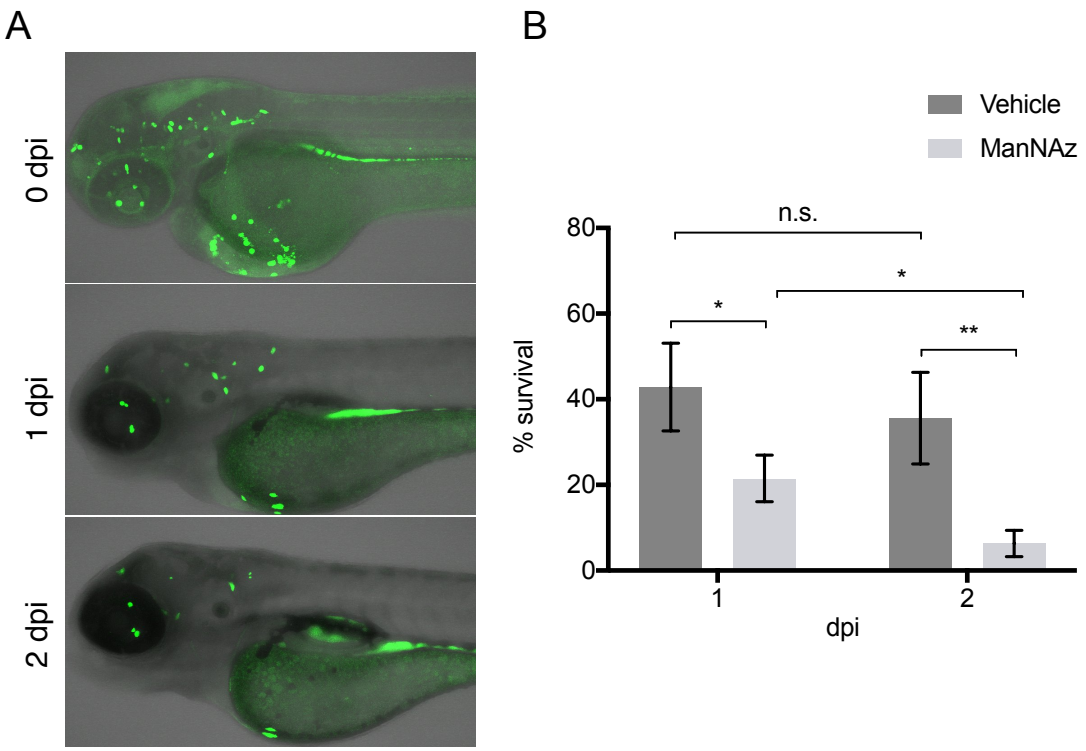

Figure 2.17. ManNAz-dependent survival of PC3 cells in zebrafish. A) Representative images of cancer cell distribution up to 2 dpi. Shown are DMSO vehicle samples. B) Percent survival is relative to initial cell count at 0 dpi for ManNAz and DMSO-treated cells. Error bars represent SD (n=4-6). *p < 0.05, **p < 0.005.

BCN-sialic acid enables labeling with fluorogenic tetrazine probes

To circumvent the challenges presented by copper-free click chemistry within the fish, other bioorthogonal reactions were explored. Agarwal et al. recently reported a bicyclononyne-modified sialic acid (BCNSia) and its incorporation into zebrafish embryos.[38] BCNSia, despite the relatively large structural perturbation of the reactive reporter, was found to be installed onto cell surface sialoglycans, allowing for labeling via the tetrazine ligation (Figure 2.18). Use of a fluorogenic tetrazine probe enabled the selective labeling of glycans inside of the fish, a feat that had not been achieved previously due to high background resulting from systemically present unreacted cyclooctyne probes. The probe used, tetrazine-Oregon Green, developed by Devaraj et al.,[45] undergoes fluorescence turn-on upon reaction with BCN (Scheme 2.1). Thus, background signal stemming from unreacted probe should be greatly diminished, enhancing imaging contrast at the tumor site.

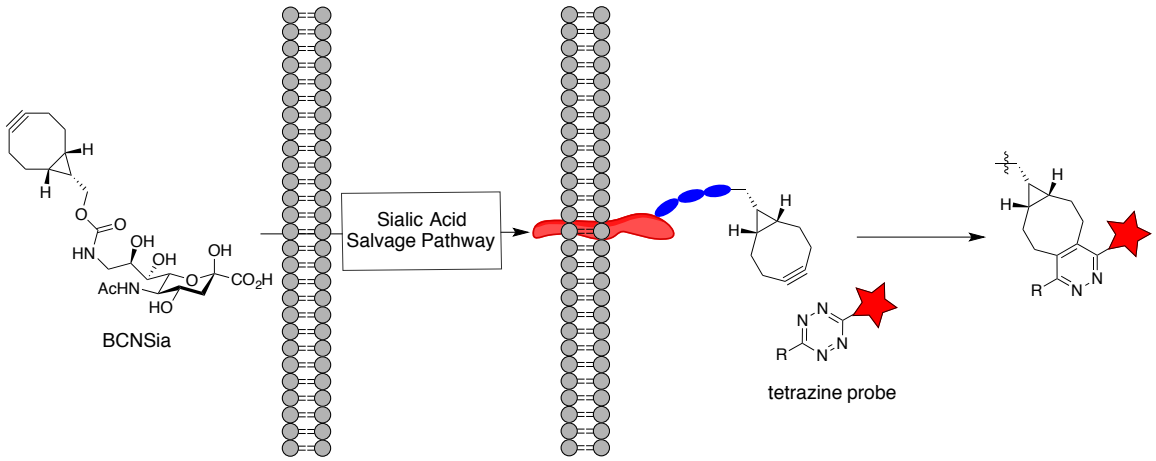

Figure 2.18. Tetrazine ligation labeling of metabolically incorporated BCN-sialic acid.

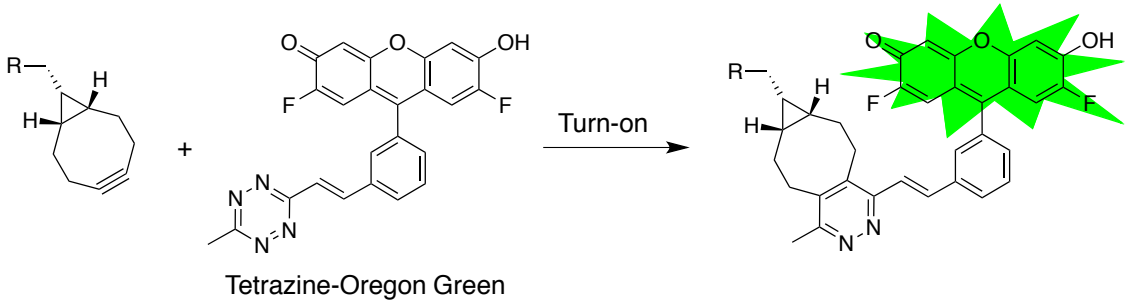

Scheme 2.1. Tetrazine ligation with a fluorogenic tetrazine probe.

The incorporation efficiency of BCNSia was evaluated in DU145 and PC3 cells. Overall incorporation, as determined by reaction with tetrazine-Cy5, was less efficient than observed for ManNAz, necessitating higher concentrations of BCNSia added to cell culture. Empirically, DU145 cells labeled more robustly with BCNSia than did PC3 cells (Figure 2.19) and were therefore selected for xenograft studies.

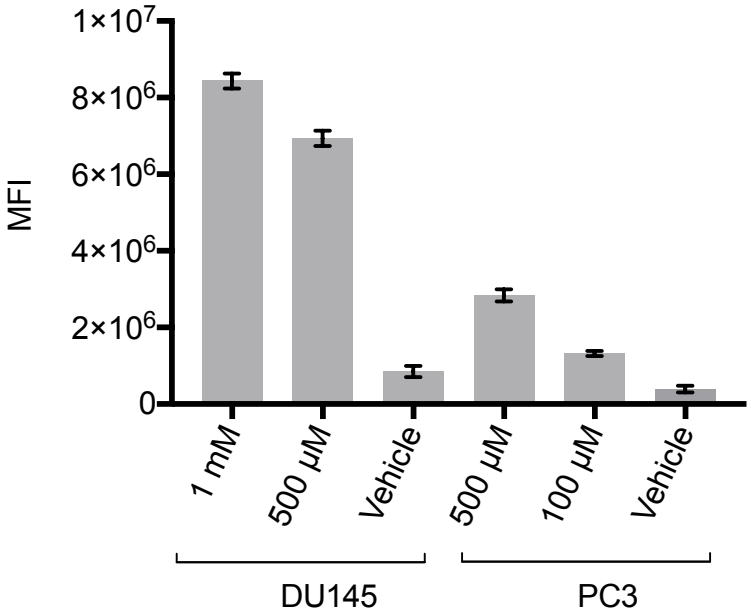

Figure 2.19. BCNSia incorporation in prostate cancer cell lines. DU145 and PC3 cells were incubated with the indicated concentrations of BCNSia for 3 d and reacted with tetrazine-Cy5. Error bars represent SD (n=3).

DU145 cells, incubated with 500 µM BCNSia and stained with CellTracker Deep Red, were injected into the sinus venosus as before. Immediately after transplantation, injection of 1 mM tetrazine-Oregon Green resulted in robust BCNSia-dependent labeling of cells throughout the embryo tail (Figure 2.20). The contrast attained was approximately 10-fold over the control, which constitutes an improvement over copper-free click chemistry as it represents all cells observed, not just a sparing few. Encouragingly, the labeling distribution appears to be cell surface-localized in many cases. Similar findings were observed in the hindbrain (Figure 2.21), although the levels of background were higher, possibly a result of increased cell death as determined by cell morphology. Notably, corresponding experiments utilizing a non-fluorogenic tetrazine-Cy5 resulted in selective labeling as well, albeit with inferior levels of contrast. (Figure 2.22).

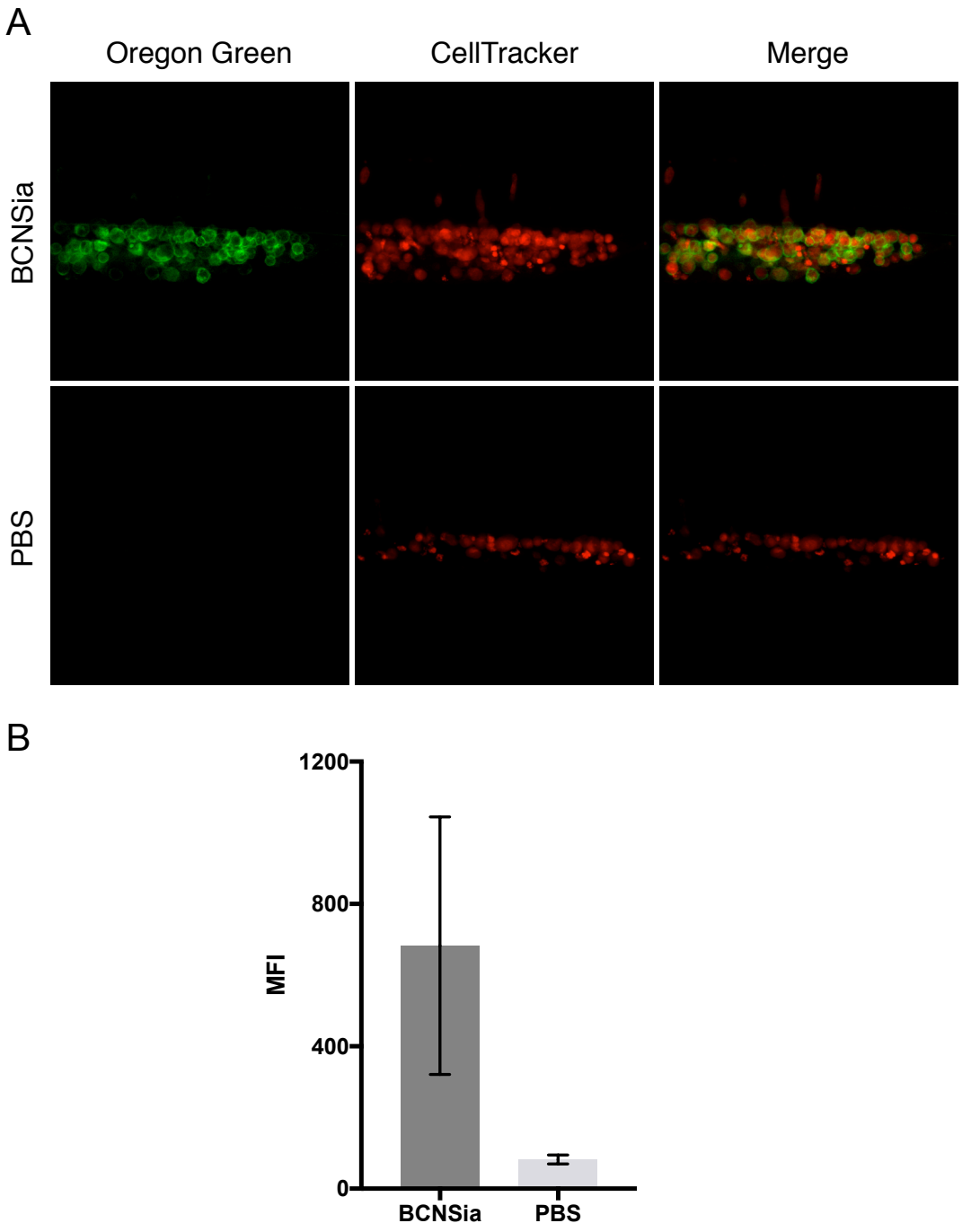

Figure 2.20. Fluorogenic tetrazine enables robust labeling of BCNSia-treated cells in the caudal vein. A) Tail images of fish injected with DU145 cells (incubated with 500 μM BCNSia) followed by tetrazine-Oregon Green administered systemically immediately prior to imaging. B) Quantification of labeling determined by the total 488 fluorescence localized to cancer cells as calculated using Imaris x64. Error bars represent SD (n=3).

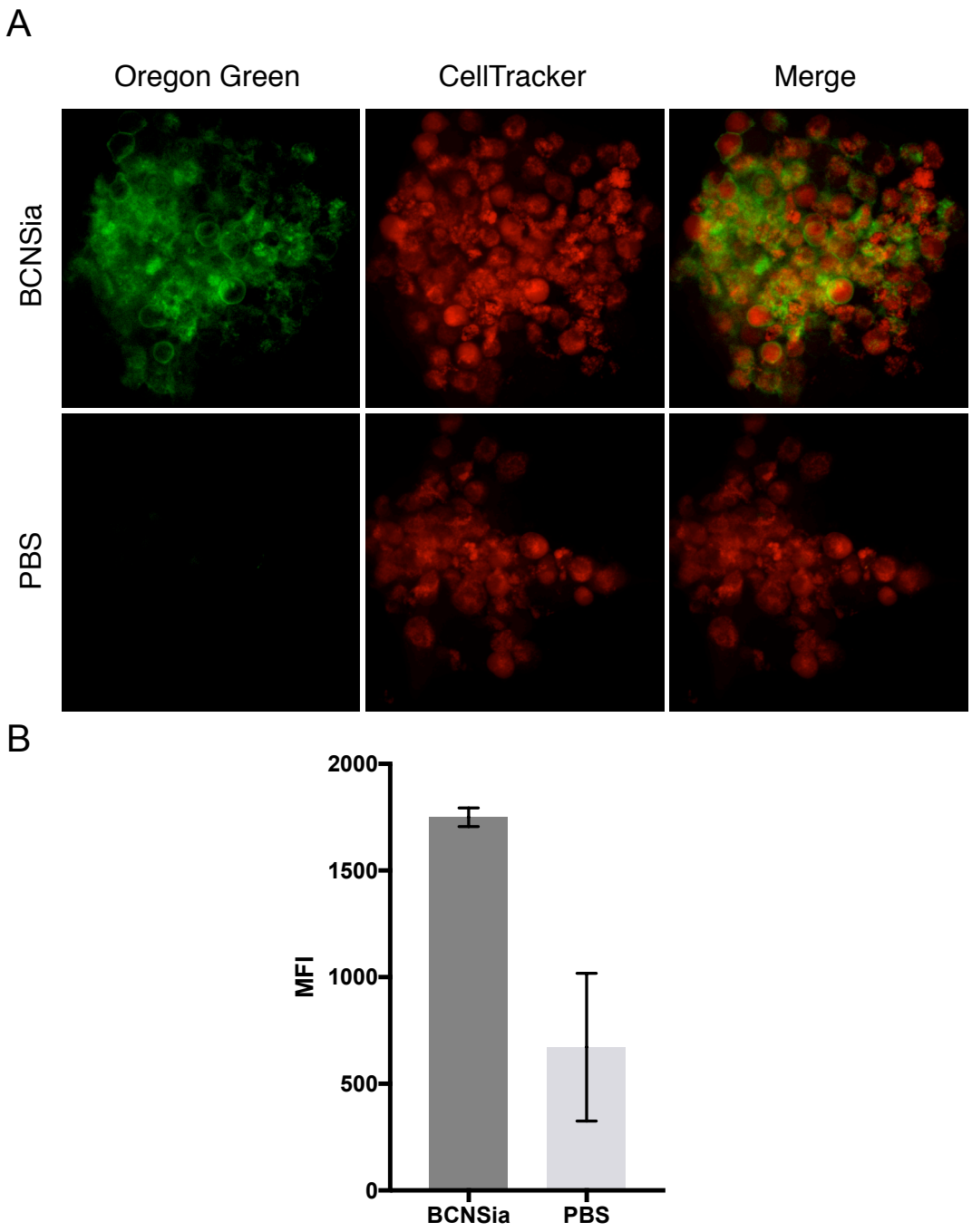

Figure 2.21. Fluorogenic tetrazine labels cancer cells in the hindbrain. A) Hindbrain images of fish injected with DU145 cells (incubated with 500 μM BCNSia) followed by tetrazine-Oregon Green administered systemically immediately prior to imaging. B) Quantification of labeling determined by the total 488 fluorescence localized to cancer cells as calculated using Imaris x64. Error bars represent SD (n=3).

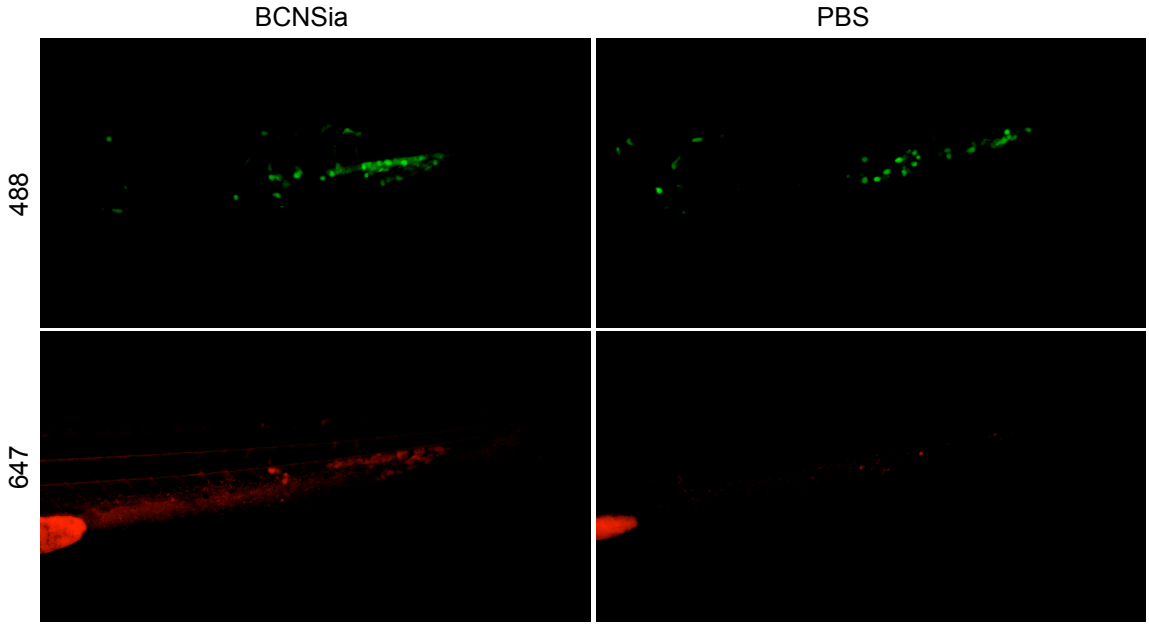

Figure 2.22. Labeling of BCNSia-treated cells in zebrafish with a non-fluorogenic tetrazine. Tail images of fish injected with DU145 cells (incubated with 500 μM BCNSia) followed by tetrazine-Cy5 administered systemically 12 h prior to imaging.

Conclusion

Herein is reported the development of methods for the metabolic bioorthogonal labeling of cancer-associated sialic acid in a zebrafish model of cancer. Selective labeling was achieved through use of the copper-click reaction to tag azidosugars on cancer cells, although these efforts were met with challenges including high background labeling and *in vivo* ManNAz-induced toxicity. These shortcomings present many opportunities to optimize this labeling system for future studies. The imaging of sialic acid was also accomplished using the tetrazine ligation with a metabolically incorporated BCN-sialic acid. The employment of a fluorogenic tetrazine probe enhanced cancer labeling consistency and level of contrast. These methods add to the expansive tool box of chemical approaches to study sialic acid *in vivo*. Future objectives focus on the application of bioorthogonal labeling to survey and track sialic acid on the cellular scale in real-time throughout different stages of metastatic progression. This will aid in our understanding of sialylation dynamics and how they influence the malignant phenotype.

Materials and Methods

General Materials

DBCO-Cy5 (DIBAC-Cy5 in this text) and tetrazine-Cy5 were obtained from Click Chemistry Tools. CellTracker Green CMFDA, CellTracker Deep Red, calcein AM, and ethidium homodimer-1 were obtained from Thermo Fisher Scientific. Ac_4ManNAz and Ac_4ManNAc were prepared as described previously.[46] BCNSia and tetrazine-Oregon Green were prepared as described previously.[38]

Tissue Culture

PC3, DU145, LNCaP, Jurkat, and K562 cells were obtained from American Type Culture Collection. PC3 cells were cultured in Ham's F-12 medium. DU145 and K562 cells were culture in Eagle's Minimum Essential Medium. LNCaP and Jurkat cells were cultured in RPMI-1640 medium. All media was supplemented with 10% fetal bovine serum (FBS), 100 units/mL penicillin and 100 µg/mL streptomycin. Cells were maintained at 37 °C and 5% CO_2 in a water-saturated incubator.

Evaluation of Artificial Sugar Incorporation into Cell Lines

Cells were passaged in appropriate media and solutions of Ac_4ManNAz in DMSO, or BCNSia in 500 mM Na_3PO_4 pH 10 buffer were added to the final aforementioned concentrations of sugar and 0.5% DMSO (for ManNAz) and allowed to incubate for 3 d. Cells were lifted using a cell scraper and suspended in 0.5 mL DBCO-Cy5 or tetrazine-Cy5 10 µM solution in PBS, and allowed to incubate at 37 °C for 1 h. Cells were washed three times and analyzed by flow cytometry.

Cell Surface Residence of ManNAz

DU145 cells were incubated with 50 µM Ac_4ManNAz or 0.5% DMSO vehicle as described. After 3 d, ManNAz or DMSO-containing media was exchanged for normal media. For the following 2 d, cells were incubated at either 37 °C or 28 °C. Cells were reacted with DBCO-Cy5 as described at indicated timepoints and analyzed by flow cytometry.

In Vitro Viability of ManNAz-treated Cells

PC3 cells were labeled with Ac_4ManNAz or DMSO vehicle control as described. Cells were stained with calcein AM and ethidium homodimer-1 according to manufacturer instructions and analyzed by flow cytometry. Cells positive for calcein AM staining and negative for ethidium homodimer-1 staining were considered viable.

Zebrafish Husbandry

Wild type AB zebrafish were obtained from Zebrafish International Resource Center. Adult zebrafish were kept at 28.5 °C on a 14-h light/10-h dark cycle. Embryos were obtained from natural spawning and maintained at 28.5 °C in embryo medium (EM; 150 mM NaCl, 0.5 mM KCl, 1.0 mM $CaCl_2$, 0.37 mM KH_2PO_4, 0.05 mM Na_2HPO_4, 2.0 mM $MgSO_4$, 0.71 mM $NaHCO_3$ in deionized water, pH 7.4) containing N-phenylthiourea (PTU; 0.2 mM). At 24 hours post fertilization (hpf), embryos were dechorionated manually using forceps. Embryos were developmentally staged according to Kimmel and coworkers.[47] Experiments involving zebrafish were performed in accordance with UC Berkeley Animal Care and Use Committee under Animal Use Protocol #R234 or Stanford University Institutional Animal Care and Use Committee under APLAC protocol #30262.

Preparation of Cells for Microinjection

Cells were labeled with artificial sugar or vehicle as above or untreated. Adherent cells were lifted with a cell scraper and washed with PBS. Suspension cells were washed with PBS. Cells were labeled with 25 μM CellTracker Green CMFDA or CellTracker Deep Red according to manufacturer instructions. Cells were washed three times and suspended in a minimal amount of PBS for injection.

Human Cancer Cell Xenotransplantation

At 48 hpf, zebrafish embryos were anesthetized in EM containing PTU (0.2 mM) and tricaine (2.4 mM). Cell suspensions prepared as described were loaded into a borosilicate (yolk or hindbrain injections) or aluminosilicate (caudal vein injections) needle and approximately 50-150 cells were injected into the hindbrain, caudal vein, yolk, or proximal to the sinus venosus. After injection of cells, embryos were incubated at 28.5 °C in EM containing PTU (0.2 mM) for 1 h and subsequently transferred to an incubator maintained at 32 °C.

Microinjection of Fluorescent Probes
At 48-96 hpf, zebrafish embryos were anesthetized in EM containing PTU (0.2 mM) and tricaine (2.4 mM). A solution of fluorescent probe in PBS was loaded into an aluminosilicate needle and approximately 3 nL were injected into the caudal vein.

In vivo Viability of ManNAz-treated Cells

PC3 cells were labeled with Ac_4ManNAz or DMSO vehicle control as described. Cells were stained with CellTracker Green CMFDA and injected near the sinus venosus of embryos at 48 hpf. Imaging was performed on both the head/trunk and tail of each embryo immediately after injection and 1 and 2 d after.

Confocal Microscopy and Image Analysis

Embryos were anesthetized in EM containing PTU (0.2 mM) and tricaine (2.4 mM) and mounted glass slides or glass-bottom well plates in 0.75% agarose. Fluorescence imaging was performed using a Zeiss LSM 780 NLO AxioExaminer, Zeiss LSM 710 AxioObserver, or Nikon A1R confocal microscrope. For longitudinal studies, embryos were demounted after imaging and maintained at 32 °C in EM containing PTU (0.2 mM). Subsequent imaging was performed according to the same procedure. Fluorescence microscopy images were analyzed using Imaris x64 v8.4.0 (Bitplane).

References

(1) Varki, A.; Esko, R. D. C. J. D.; Stanley, H. H. F. P.; Etzler, C. R. B. G. W. H. M. E. *Essentials of Glycobiology*; 2010.

(2) Varki, A. Glycan-Based Interactions Involving Vertebrate Sialic-Acid-Recognizing Proteins. *Nature* **2007**, *446*, 1023–1029.

(3) Swindall, A. F.; Bellis, S. L. Sialylation of the Fas Death Receptor by St6Gal-I Provides Protection against Fas-Mediated Apoptosis in Colon Carcinoma Cells. *J. Biol. Chem.* **2011**, *286*, 22982–22990.

(4) Sanchez-Ruderisch, H.; Detjen, K. M.; Welzel, M.; André, S.; Fischer, C.; Gabius, H.-J.; Rosewicz, S. Galectin-1 Sensitizes Carcinoma Cells to Anoikis via the Fibronectin Receptor α5β1-Integrin. *Cell Death Differ.* **2011**, *18* (5), 806–816.

(5) Läubli, H.; Borsig, L. Selectins Promote Tumor Metastasis. *Semin. Cancer Biol.* **2010**, *20*, 169–177.

(6) Macauley, M. S.; Crocker, P. R.; Paulson, J. C. Siglec-Mediated Regulation of Immune Cell Function in Disease. *Nat. Rev. Immunol.* **2014**, *14*, 653–666.

(7) Jandus, C.; Boligan, K. F.; Chijioke, O.; Liu, H.; Dahlhaus, M.; Démoulins, T.; Schneider, C.; Wehrli, M.; Hunger, R. E.; Baerlocher, G. M.; et al. Interactions between Siglec-7 / 9 Receptors and Ligands Influence NK Cell – Dependent Tumor Immunosurveillance. *J. Clin. Invest.* **2014**, *124*, 1810–1820.

(8) Hudak, J. E.; Canham, S. M.; Bertozzi, C. R. Glycocalyx Engineering Reveals a Siglec-Based Mechanism for NK Cell Immunoevasion. *Nat. Chem. Biol.* **2014**, *10*, 69–75.

(9) Stowell, S. R.; Ju, T.; Cummings, R. D. Protein Glycosylation in Cancer. *Annu Rev Pathol* **2015**, *10*, 473–510.

(10) Büll, C.; Stoel, M. A.; Den Brok, M. H.; Adema, G. J. Sialic Acids Sweeten a Tumor's Life. *Cancer Res.* **2014**, *74*, 3199–3204.

(11) Schultz, M. J.; Swindall, A. F.; Bellis, S. L. Regulation of the Metastatic Cell Phenotype by Sialylated Glycans. *Cancer Metastasis Rev.* **2012**, *31*, 501–518.

(12) Pearce, O. M. T.; Läubli, H. Sialic Acids in Cancer Biology and Immunity. *Glycobiology* **2015**, *26*, 111–128.

(13) Dube, D. H.; Bertozzi, C. R. Glycans in Cancer and Inflammation--Potential for Therapeutics and Diagnostics. *Nat. Rev. Drug Discov.* **2005**, *4*, 477–488.

(14) Büll, C.; Boltje, T. J.; Wassink, M.; de Graaf, A. M. A.; van Delft, F. L.; den Brok, M. H.; Adema, G. J. Targeting Aberrant Sialylation in Cancer Cells Using a Fluorinated Sialic Acid Analog Impairs Adhesion, Migration, and In Vivo Tumor Growth. *Mol. Cancer Ther.* **2013**, *12*, 1935–1946.

(15) Büll, C.; Heise, T.; Adema, G. J.; Boltje, T. J. Sialic Acid Mimetics to Target the Sialic Acid – Siglec Axis. *Trends Biochem. Sci.* **2016**, *41*, 519–531.

(16) Park, S.; Lee, M.-R.; Shin, I. Chemical Tools for Functional Studies of Glycans. *Chem. Soc. Rev.* **2008**, *37*, 1579–1591.

(17) Haab, B. B. Using Lectins in Biomarker Research: Addressing the Limitations of Sensitivity and Availability. *Proteomics Clin Appl* **2012**, *6*, 346–350.
(18) Du, J.; Meledeo, M. A.; Wang, Z.; Khanna, H. S.; Paruchuri, V. D. P.; Yarema, K. J. Metabolic Glycoengineering: Sialic Acid and beyond. *Glycobiology* **2009**, *19*, 1382–1401.
(19) Chang, P. V; Prescher, J. A.; Sletten, E. M.; Baskin, J. M.; Miller, I. A.; Agard, N. J.; Lo, A.; Bertozzi, C. R. Copper-Free Click Chemistry in Living Animals. *Proc. Natl. Acad. Sci. U. S. A.* **2010**, *107*, 1821–1826.
(20) Koo, H.; Lee, S.; Na, J. H.; Kim, S. H.; Hahn, S. K.; Choi, K.; Kwon, I. C.; Jeong, S. Y.; Kim, K. Bioorthogonal Copper-Free Click Chemistry In Vivo for Tumor-Targeted Delivery of Nanoparticles. *Angew. Chemie Int. Ed.* **2012**, *51*, 11836–11840.
(21) Xie, R.; Dong, L.; Huang, R.; Hong, S.; Lei, R.; Chen, X. Targeted Imaging and Proteomic Analysis of Tumor-Associated Glycans in Living Animals. *Angew. Chemie Int. Ed.* **2014**, *53*, 14082–14086.
(22) Xiao, H.; Woods, E. C.; Vukojicic, P.; Bertozzi, C. R. Precision Glycocalyx Editing as a Strategy for Cancer Immunotherapy. *Proc. Natl. Acad. Sci. U. S. A.* **2016**, *113*, 10304–10309.
(23) Neves, A. a; Stöckmann, H.; Harmston, R. R.; Pryor, H. J.; Alam, I. S.; Ireland-Zecchini, H.; Lewis, D. Y.; Lyons, S. K.; Leeper, F. J.; Brindle, K. M. Imaging Sialylated Tumor Cell Glycans in Vivo. *FASEB J.* **2011**, *25*, 2528–2537.
(24) Neves, A.; Stöckmann, H.; Wainman, Y.; Kuo, J.; Fawcett, S.; Leeper, F.; Brindle, K. Imaging Cell Surface Glycosylation in Vivo Using “Double Click” Chemistry. *Bioconjug. Chem.* **2013**, *24*, 934–941.
(25) Leblond, F.; Davis, S. C.; Valdés, P. A.; Pogue, B. W. Pre-Clinical Whole-Body Fluorescence Imaging: Review of Instruments, Methods and Applications. *J. Photochem. Photobiol. B Biol.* **2010**, *98*, 77–94.
(26) Ellenbroek, S. I. J.; van Rheenen, J. Imaging Hallmarks of Cancer in Living Mice. *Nat. Rev. Cancer* **2014**, *14*, 406–418.
(27) Koga, S.; Oshima, Y.; Honkura, N.; Iimura, T.; Kameda, K.; Sato, K.; Yoshida, M.; Yamamoto, Y.; Watanabe, Y.; Hikita, A.; et al. In Vivo Subcellular Imaging of Tumors in Mouse Models Using a Fluorophore-Conjugated Anti-Carcinoembryonic Antigen Antibody in Two-Photon Excitation Microscopy. *Cancer Sci.* **2014**, *105*, 1299–1306.
(28) Massoud, T. F.; Gambhir, S. S. Molecular Imaging in Living Subjects: Seeing Fundamental Biological Processes in a New Light. *Genes Dev.* **2003**, *17*, 545–580.
(29) White, R.; Rose, K.; Zon, L. Zebrafish Cancer: The State of the Art and the Path Forward. *Nat. Rev. Cancer* **2013**, *13*, 624–636.
(30) Nicoli, S.; Ribatti, D.; Cotelli, F.; Presta, M. Mammalian Tumor Xenografts Induce Neovascularization in Zebrafish Embryos. *Cancer Res.* **2007**, *67*, 2927–2931.
(31) de Boeck, M.; Cui, C.; Mulder, A. A.; Jost, C. R.; Ikeno, S.; ten Dijke, P. Smad6 Determines BMP-Regulated Invasive Behaviour of Breast Cancer

Cells in a Zebrafish Xenograft Model. *Sci. Rep.* **2016**, *6*, 24968.
(32) Stoletov, K.; Kato, H.; Zardouzian, E.; Kelber, J.; Yang, J.; Shattil, S.; Klemke, R. Visualizing Extravasation Dynamics of Metastatic Tumor Cells. *J. Cell Sci.* **2010**, *123* (Pt 13), 2332–2341.
(33) He, S.; Lamers, G. E. M.; Beenakker, J. W. M.; Cui, C.; Ghotra, V. P. S.; Danen, E. H. J.; Meijer, A. H.; Spaink, H. P.; Snaar-Jagalska, B. E. Neutrophil-Mediated Experimental Metastasis Is Enhanced by VEGFR Inhibition in a Zebrafish Xenograft Model. *J. Pathol.* **2012**, *227*, 431–445.
(34) Yang, X. J.; Chen, G. L.; Yu, S. C.; Xu, C.; Xin, Y. H.; Li, T. T.; Shi, Y.; Gu, A.; Duan, J. J.; Qian, C.; et al. TGF-β1 Enhances Tumor-Induced Angiogenesis via JNK Pathway and Macrophage Infiltration in an Improved Zebrafish Embryo/xenograft Glioma Model. *Int. Immunopharmacol.* **2013**, *15*, 191–198.
(35) Wang, J.; Cao, Z.; Zhang, X. M.; Nakamura, M.; Sun, M.; Hartman, J.; Harris, R. A.; Sun, Y.; Cao, Y. Novel Mechanism of Macrophage-Mediated Metastasis Revealed in a Zebrafish Model of Tumor Development. *Cancer Res.* **2015**, *75*, 306–315.
(36) Ko, S.-K.; Chen, X.; Yoon, J.; Shin, I. Zebrafish as a Good Vertebrate Model for Molecular Imaging Using Fluorescent Probes. *Chem. Soc. Rev.* **2011**, *40*, 2120–2130.
(37) Dehnert, K. W.; Baskin, J. M.; Laughlin, S. T.; Beahm, B. J.; Naidu, N. N.; Amacher, S. L.; Bertozzi, C. R. Imaging the Sialome during Zebrafish Development with Copper-Free Click Chemistry. *ChemBioChem* **2012**, *13*, 353–357.
(38) Agarwal, P.; Beahm, B. J.; Shieh, P.; Bertozzi, C. R. Systemic Fluorescence Imaging of Zebrafish Glycans with Bioorthogonal Chemistry. *Angew. Chemie Int. Ed.* **2015**, *54*, 11504–11510.
(39) Teng, Y.; Xie, X.; Walker, S.; White, D. T.; Mumm, J. S.; Cowell, J. K. Evaluating Human Cancer Cell Metastasis in Zebrafish. *BMC Cancer* **2013**, *13*, 453.
(40) Pruvot, B.; Jacquel, A.; Droin, N.; Auberger, P.; Bouscary, D.; Tamburini, J.; Muller, M.; Fontenay, M.; Chluba, J.; Solary, E. Leukemic Cell Xenograft in Zebrafish Embryo for Investigating Drug Efficacy. *Haematologica* **2011**, *96*, 612–616.
(41) Konantz, M.; Balci, T. B.; Hartwig, U. F.; Dellaire, G.; André, M. C.; Berman, J. N.; Lengerke, C. Zebrafish Xenografts as a Tool for in Vivo Studies on Human Cancer. *Ann. N. Y. Acad. Sci.* **2012**, *1266*, 124–137.
(42) Veinotte, C. J.; Dellaire, G.; Berman, J. N. Hooking the Big One: The Potential of Zebrafish Xenotransplantation to Reform Cancer Drug Screening in the Genomic Era. *Dis Model Mech* **2014**, *7*, 745–754.
(43) Swanhart, L. M.; Cosentino, C. C.; Diep, C. Q.; Davidson, A. J.; de Caestecker, M.; Hukriede, N. A. Zebrafish Kidney Development: Basic Science to Translational Research. *Birth Defects Res. C* **2011**, *93*, 141–156.
(44) Zhuo, Y.; Bellis, S. L. Emerging Role of α2,6-Sialic Acid as a Negative Regulator of Galectin Binding and Function. *J. Biol. Chem.* **2011**, *286*,

5935–5941.
(45) Wu, H.; Yang, J.; Seckute, J.; Devaraj, N. K. In Situ Synthesis of Alkenyl Tetrazines for Highly Fluorogenic Bioorthogonal Live-Cell Imaging Probes. *Angew. Chemie Int. Ed.* **2014**, *53*, 5805–5809.
(46) Laughlin, S. T.; Bertozzi, C. R. Metabolic Labeling of Glycans with Azido Sugars and Subsequent Glycan-Profiling and Visualization via Staudinger Ligation. *Nat. Protoc.* **2007**, *2*, 2930–2944.
(47) Kimmel, C. B.; Ballard, W. W.; Kimmel, S. R.; Ullmann, B.; Schilling, T. F. Stages of Embryonic Development of the Zebrafish. *Dev. Dyn.* **1995**, *203*, 253–310.

Chapter 3

Elucidating the Role of Sialic Acid in Cancer Cell Survival in a Zebrafish Model

Chapter 3. Elucidating the Role of Sialic Acid in Cancer Cell Survival in a Zebrafish Model

Introduction

Changes in glycosylation with the onset and progression of cancer have been well catalogued, with the overexpression of cell surface sialic acid observed as a pervasive characteristic of a multitude of cancer types.[1] Indeed, hypersialylation is often considered a hallmark of the malignant phenotype and is correlated with a poor clinical prognosis.[2,3] As such, a great deal of research has focused on illuminating the functional role of sialic acid in cancer progression, and it has been documented that elevated levels of sialic acid contribute to the survival and proliferation of transformed cells through various mechanisms.[4–6] Aberrant sialylation has been shown to disrupt native cell signaling interactions, allowing cancerous cells to elude normal cell death pathways, thereby enhancing persistence and dissemination within the host.[7–9] Additionally, cancer-associated sialosides facilitate extravasation by binding to selectins on the vascular endothelium, augmenting cell motility and invasiveness.[10] Finally, and of particular interest, cancer cells capitalize on the immunoregulatory functions of sialic acid to escape destruction by the host immune system.[6]

Recent years have provided detailed insight into sialic acid-mediated cancer immune evasion. Sialic acid modulates the host immune response through recognition by sialic acid-binding immunoglobulin-type lectins (Siglecs), which primarily reside on the surface of cells of the immune system.[11,12] Through cytosolic domains containing immunoreceptor tyrosine-based inhibitory or activation motifs (ITIMs or ITAMs), Siglecs can dampen or heighten an immune cell's response upon binding a sialylated ligand. It is believed that this tuning of activity prevents immune cells from damaging naturally sialylated healthy cells. This creates an opportunity for cancer cells rich in sialic acid to engage inhibitory siglecs, e.g., Siglec-7 and Siglec-9 expressed on natural killer cells, suppressing the immune response and avoiding detection.[13,14] This realization has led to the development of methods to selectively desialylate cancer cells and render them susceptible to immunorecognition.[15] While the biochemical basis of sialic acid-mediated immunomodulation is becoming deciphered, how it impacts cancer-immune cell dynamics *in vivo* is less understood.

Current mouse models of cancer cell progression are limited by the inability to observe the interactions of immune cells with cancer cells in real time. The embryonic zebrafish, by virtue of its optical translucency, offers an optimal *in vivo* model for visualizing cancer-immune cell interactions.[16] Additionally, adaptive immunity remains immature through the first several weeks of development,[17] allowing for focused studies on innate immune cells, macrophages and neutrophils, which also display Siglec-mediated regulation of the immune response in humans.[11] Interactions between cancer cells and both macrophages and neutrophils have been observed in xenograft and spontaneous tumor models in zebrafish embryos at the single cell level, shedding light on how

these processes influence metastasis and neoangiogenesis.[18–22] These studies have been aided by the availability of transgenic zebrafish lines bearing fluorescent markers of innate immune cells.[23,24] Thus, the zebrafish model enables focused observations not feasible in mice.

To date, cancer sialylation has yet to be examined in zebrafish. While most of the immunoregulatory Siglecs present in humans have not been characterized in zebrafish, the zebrafish genome does contain an ortholog of human Siglec-15.[25] In mammalian systems, Siglec-15 shows binding specificity for the sialyl Tn antigen, a glycan commonly observed in cancer, and is expressed predominantly in macrophage subsets where it appears to be vital for osteoclast differentiation.[25–30] Siglec-15 has also been found on tumor-associated macrophages where its binding triggers the release of immunosuppressive cytokines.[31] Though it lacks a signaling domain of its own, Siglec-15 associates with adapter molecules bearing ITAMs. The zebrafish genome also bears a second Siglec-like protein containing a putative ITIM, which may allude to an immunoregulatory role for paired receptors in zebrafish.[25]

It is important to note that the absence of well-characterized Siglecs in zebrafish does not preclude the existence of functionally similar modes of sialic acid-mediated immunomodulation. As well, there are other routes by which sialic acid contributes to cancer progression (vide supra). This chapter summarizes efforts to understand how sialic acid influences cancer cell survival in a zebrafish xenograft model, with primary focus on the interplay with innate immune cells. Sialidase pretreatment reveals that sialic acid affects cancer cell survival and immune recruitment in zebrafish, though the mechanisms by which these occur remain ambiguous. Further optimization of the cancer model may be required to hone in on these details.

Results and Discussion

Evaluation of sialidase from Vibrio cholerae

Given that little is known about cancer-associated sialic acid recognition in zebrafish, an exploratory approach was adopted to determine which aspects of cancer cell survival *in vivo* are influenced by sialylation. Pretreatment of cancer cells with a sialidase to eliminate cell surface sialic acid followed by transplantation into zebrafish embryos would allow for the empirical observation of changes in cancer cell behavior that are dependent on sialic acid content. To this end, a sialidase from *Vibrio cholerae* was selected for its ability to cleave a variety of sialic acid linkages[32,33] and its demonstrated use to modulate interaction with immune cell Siglecs.[15,34] *V. cholerae* sialidase (VCsia) was evaluated for activity on several different human cancer cell lines: DU145 and PC3 prostate cancer cells, and stably GFP-expressing M4A4 and CL16 melanoma cells. The degree of sialic acid reduction was surveyed by binding of a DyLight 649-conjugated lectin from *Sambucus nigra* (SNA-I), which primarily recognizes α2,6-linked sialic acid.[35] Flow cytometry analysis revealed a

significant reduction in SNA-I binding of approximately 95% for all cell lines tested, suggesting that sialic acid removal by VCsia is quite efficient (Figure 3.1).

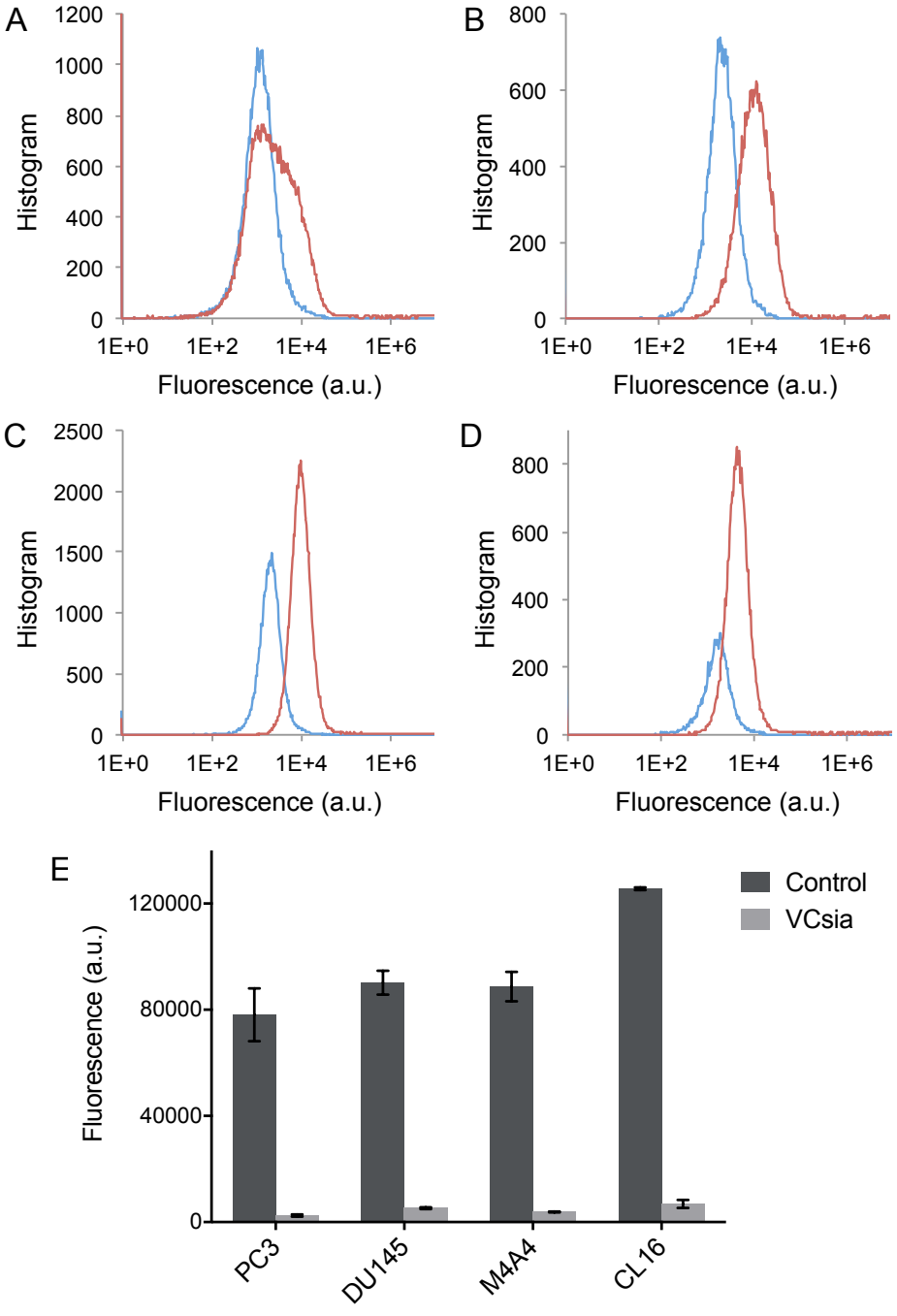

Figure 3.1. Desialylation of cancer cells with sialidase from *V. cholerae.* Flow cytometry histograms for (A) PC3, (B) DU145, (C) M4A4, and (D) CL16 cells. Blue, sialidase-treated; red, DPBS control. (E) Mean fluorescence intensity of treated and control cells after staining with DyLight 649-conjugated SNA-I lectin. Error bars represent SD (n=3).

M4A4 cells were chosen for subsequent experiments based on their unimodal SNA-I binding shift and higher viability after VCsia-treatment than DU145 or CL16 cells (data not shown). Additionally, M4A4 cells robustly incorporate ManNAz, creating opportunities to study sialylation using metabolic bioorthogonal labeling approaches (Figure S3.1).

The duration of sialic acid reduction was crucial to determine, as this parameter would govern the timescale by which differential sialic acid-dependent interactions might occur. It was observed *in vitro* by SNA-I binding that by 12 hours post sialidase-treatment, sialylation had been restored to native levels (Figure 3.2A). This rapid recovery is likely due to the mobilization of intracellular pools of sialic acid to the cell surface.[36] A notable caveat is that the rate of sialic acid restoration may be different within the environment of a zebrafish model, where transplanted cells may experience suboptimal conditions of nutrient availability and other stressors. Desialylation was found to have no effect on cell viability at each timepoint investigated, suggesting that differences observed *in vivo* would be host-related and not attributed to sialidase toxicity (Figure 3.2B).

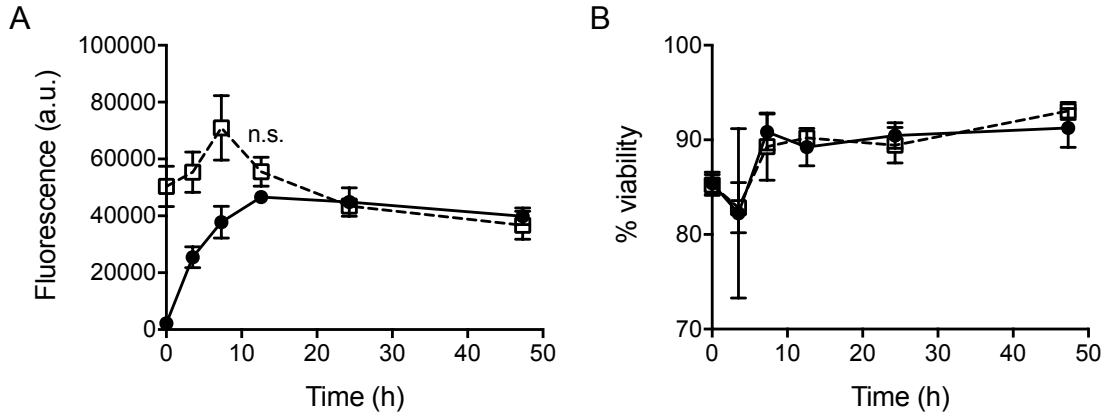

Figure 3.2. Sialic acid recovery following desialylation with *V. cholerae* sialidase. (A) Mean fluorescence intensity from DyLight 649-conjugated SNA-I lectin. Timepoint 1; $p < 0.005$. Timepoints 2, 3; $p < 0.05$. (B) Cell viability estimated from frequency of parent (%) included in flow cytometry gate. Black circle, sialidase-treated; white square, DPBS control. Error bars represent SD of (n=3).

Sialidase treatment affects cancer cell survival in a myeloid differentiation knockdown model

The interplay between cancer cells and the innate immune system, namely macrophages and neutrophils, has been studied in cancer xenograft models in zebrafish.[16] Such interactions have been observed to play critical roles in cancer progression, promoting early tumorigenesis and metastasis.[19] In light of the ubiquity of sialic acid-mediated immunoregulation in mammalian models of

cancer, we aimed to establish the existence of similar modes of cancer survival within zebrafish. A myeloid differentiation knockdown model proved suitable for this goal, whereby the survival of desialylated cancer cells was monitored in the presence or absence of a fully functional innate immune system.

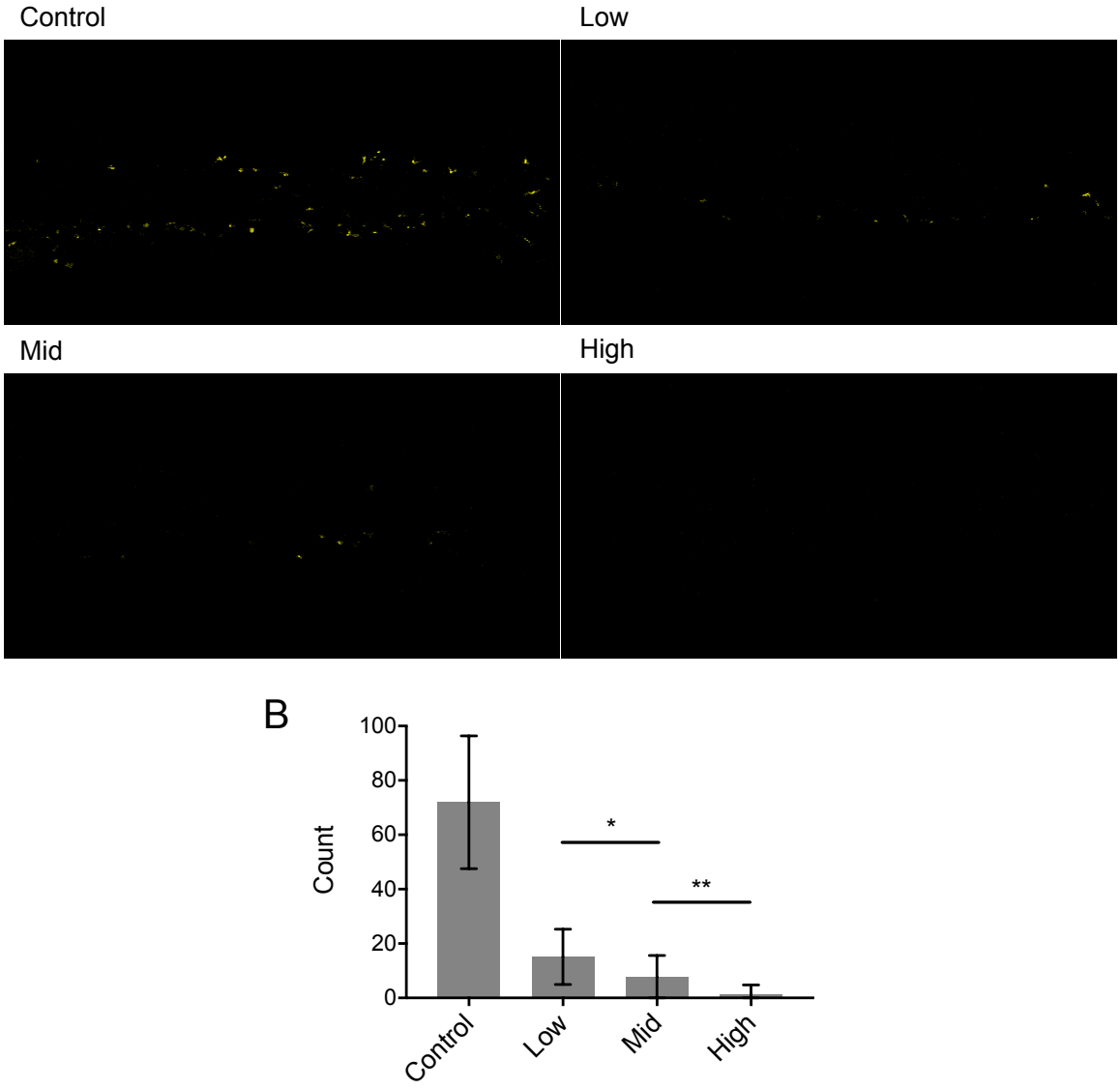

Figure 3.3. Pu.1 morpholino knockdown dose-dependence. (A) Representative tail images of pu.1 morphant embyros (mfap4:YFP) at 2 dpf. (B) Macrophage count as determined by number of discrete objects detected. Control, uninjected; low, 0.4 mM; mid, 0.8 mM; high, 1.6 mM. Error bars represent SD (n=14-15). *p < 0.05, **p < 0.005.

Macrophage depletion was accomplished through microinjection at the one-cell stage of a morpholino targeting pu.1, a transcription factor for myeloid differentiation.[37] A transgenic zebrafish line expressing a fluorescent protein marker under the macrophage-specific mfap4 promoter[24] was used to determine the appropriate dose to achieve complete macrophage knockdown while avoiding any other observable phenotypic abnormalities (Figure 3.3), thus a concentration of 1.6 mM morpholino was used for subsequent experiments. While the pu.1 morpholino primarily affects macrophages, the concentration used may also reduce neutrophil populations, though likely to a lesser extent.[38]

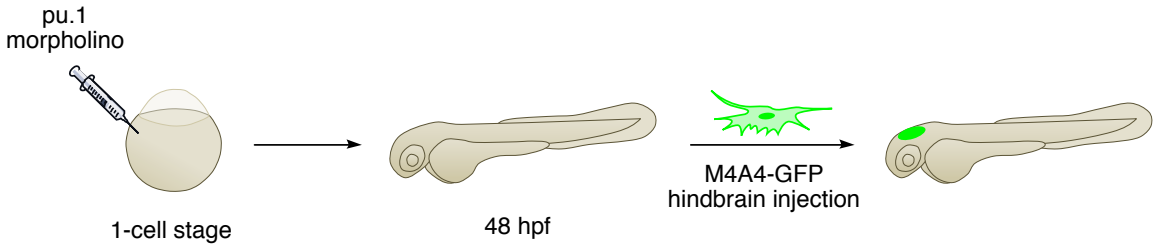

Figure 3.4. GFP-expressing M4A4 hindbrain xenograft in a macrophage depletion model.

Evaluation of the role of sialic acid in cancer cell survival in zebrafish embryos was performed by treatment of GFP-expressing M4A4 cells with VCsia, as above, immediately prior to microinjection into the hindbrain of pu.1 morphant or untreated embryos at 48 hours post fertilization (hpf) (Figure 3.4). Cell survival in each embryo was monitored over a two-day period by fluorescence imaging, with the amount of viable cells calculated from the total volume of GFP fluorescent signal. In immunocompetent embryos, VCsia-treated cells exhibited significantly diminished viability compared to cells treated with PBS (45% versus 73% survival) by 42 hours post injection (hpi) (Figure 3.5A). This represents a delay with respect to the measured recovery time from desialylation, suggesting that sialic acid-dependent effects on survival take time to manifest after putative recognition events. Parallel results from pu.1 morphant embryos indicate that macrophage depletion rescues survival following VCsia-treatment (Figure 3.5B), implying a macrophage-dependent pathway of cancer cell death. The survival enhancement is vast enough that VCsia-treated cells in pu.1 morphant embryos show greater survival than untreated cells in immunocompetent fish at all timepoints tested ($p < 0.05$). An additional experimental condition examining untreated cells with pu.1 knockdown is needed to more completely determine the extent of survival attributable to macrophage knockdown after desialylation. Nonetheless, the data confirms that the innate immune system contributes to cancer cell death in zebrafish, though the degree of sialic acid involvement in macrophage-mediated killing is unclear.

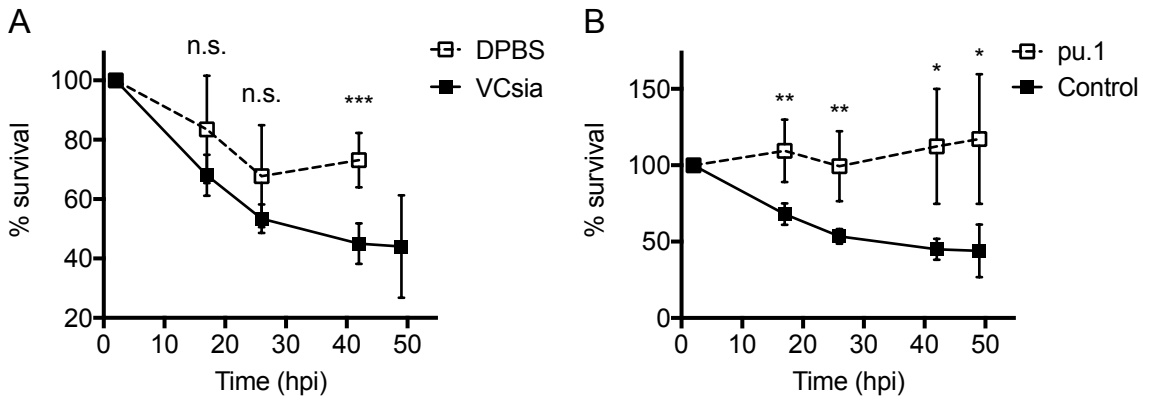

Figure 3.5. Cancer cell survival in a macrophage knockdown model. (A) Cell survival of GFP-expressing M4A4 cells treated with either sialidase or DPBS control and injected at 48 hpf. Error bars represent SD (n=10 control, 5 treated). (B) Survival of sialidase-treated M4A4 cells in pu.1 morphant embryos or uninjected control embryos - same dataset as VCsia in (A). Error bars represent SD (n=5 control, 4 treated). *p < 0.05, **p < 0.005, ***p < 0.0005.

Cancer desialylation alters macrophage and neutrophil recruitment to the hindbrain

We next aimed to gain more detailed insight into the influence of cancer sialylation on immune cell behavior in zebrafish. Zebrafish macrophages have been shown to infiltrate tumor xenografts within hours of transplantation, where interactions within the tumor microenvironment often favor metastatic progression by facilitating tumor cell intravasation and angiogenesis. [20–22] We surmised that desialylation might alter the distribution of macrophages in the cancer cell vicinity as their activity shifts from protumorigenic to tumoricidal. VCsia-treated M4A4 cells were injected into the hindbrain of transgenic zebrafish bearing macrophages expressing the red fluorescent protein tdTomato. The total volume of macrophages residing in the hindbrain normalized to M4A4 volume was used as a metric for recruitment (Figure 3.6). VCsia-treated cells elicited a greater macrophage recruitment response than control cells shortly after injection, with a sustained increase in macrophage volume through the duration of the study. Interestingly, this occurred within hours of cancer cell introduction, while VCsia-dependent alterations to cell viability were not observed until 42 hpi. This may be in accordance with a macrophage tumoricidal response, which has been documented to take up to 24 hours.[39]

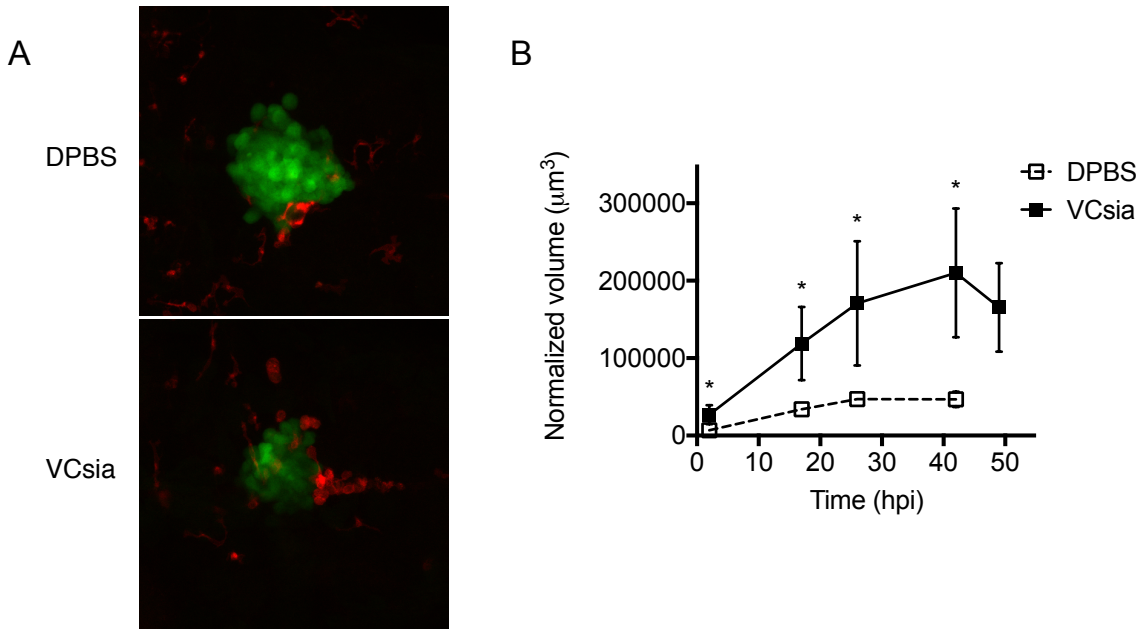

Figure 3.6. Macrophage recruitment to hindbrain with sialidase treatment. (A) GFP-expressing M4A4 cells in hindbrain of mfap4:tdTomato embryos at 17 hpi. GFP-RFP channel overlay: green, M4A4 cells; red, macrophages. (B) Volume of macrophages in the hindbrain is calculated from fluorescence signal in mfap4:tdTomato zebrafish embryos and normalized to the total volume of GFP-expressing M4A4 cells present. Error bars represent SEM (n=4-5). *$p < 0.05$.

As with macrophages, neutrophils are rapidly recruited to tumors and have been reported to display both pro- and antitumor activity.[40] Neutrophils have been previously examined in zebrafish cancer xenograft models where they promote tumor invasion and metastasis through host tissue remodeling.[19] Neutrophil recruitment was assayed in the same manner as macrophage recruitment, using a zebrafish line expressing the fluorescent protein DsRed under control of the lysozyme C promoter, which is abundantly present in neutrophils.[23] In contrast to macrophage recruitment results, VCsia-treated cells induced increased neutrophil recruitment to the hindbrain only after 22 hours, with no change measured at earlier timepoints (Figure 3.7A). This was somewhat unanticipated, as neutrophils are typically the first immune cell to respond to inflammatory stimuli, although it may reflect a lack of sialic acid-dependent recognition by neutrophils in zebrafish. Curiously, a decrease in the viability of VCsia-treated cells was detectable by 22 hours (Figure 3.7B), as opposed to 42 hours in our initial study. The temporal correspondence of increased cell death and neutrophil content may suggest that recruitment is in response to dead cellular debris rather than differential sialic acid expression. Additionally, the differences between this and the previously discussed cancer cell viability experiment highlight inconsistencies between studies.

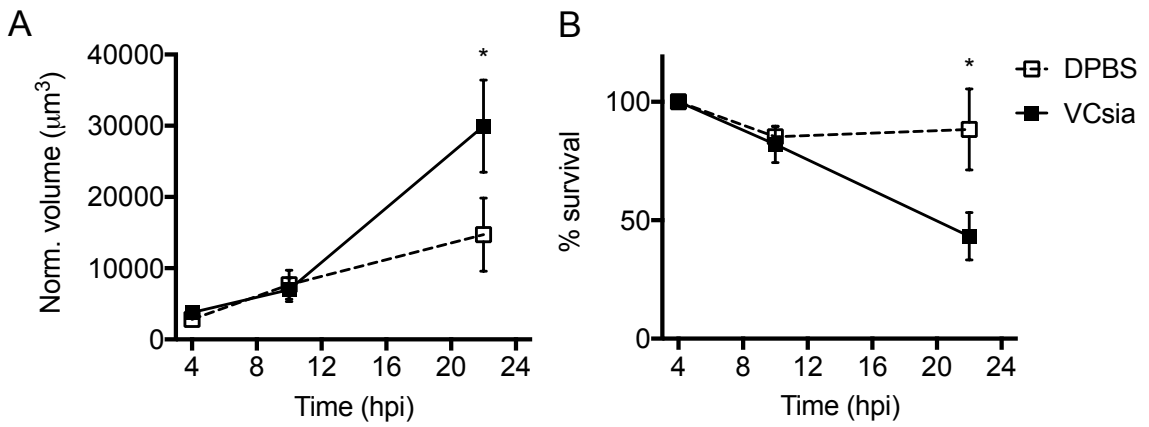

Figure 3.7. Quantitation of neutrophil recruitment and cancer cell survival in hindbrain. (A) Neutrophil volume within hindbrain for embryos (LysC:DsRed) implanted with GFP-expressing M4A4 cells treated with sialidase or DBPS control. Volume is normalized to total volume of cancer cells present. (B) Survival of sialidase-treated or DBPS-treated cells. Error bars represent SEM (n=12-16). *$p < 0.05$.

Desialylation decreases cancer cell viability shortly after transplantation

It was noted during preliminary experiments employing microinjection of GFP-expressing M4A4 cells that the initial tumor burden, as gauged by GFP fluorescence signal, was consistently lower for cells that had undergone VCsia treatment than for control cells. This was originally attributed to increased sialidase-dependent cell aggregation leading to uneven injection volumes. Adjustments made to the microinjection procedure failed to completely remedy this issue, however. An alternate explanation was that, while the total number of cells injected might be comparable between VCsia-treated and control groups, a decrease in cell viability immediately following transplantation would result in diminished GFP fluorescence and an underestimation of initial cell loading. To investigate this hypothesis, GFP-expressing M4A4 cells were stained with a near-IR Cy5-based CellTracker dye prior to hindbrain injection. In this manner, GFP signal would report on viable cells and Cy5 signal would report on total injected cellular material, including cells with compromised viability. The ratio of GFP to Cy5 signal provided a means to judge post-injection viability. It was found that a significant degree of cell death occurs shortly after injection in VCsia-treated cells compared to untreated cells (Figure 3.8).

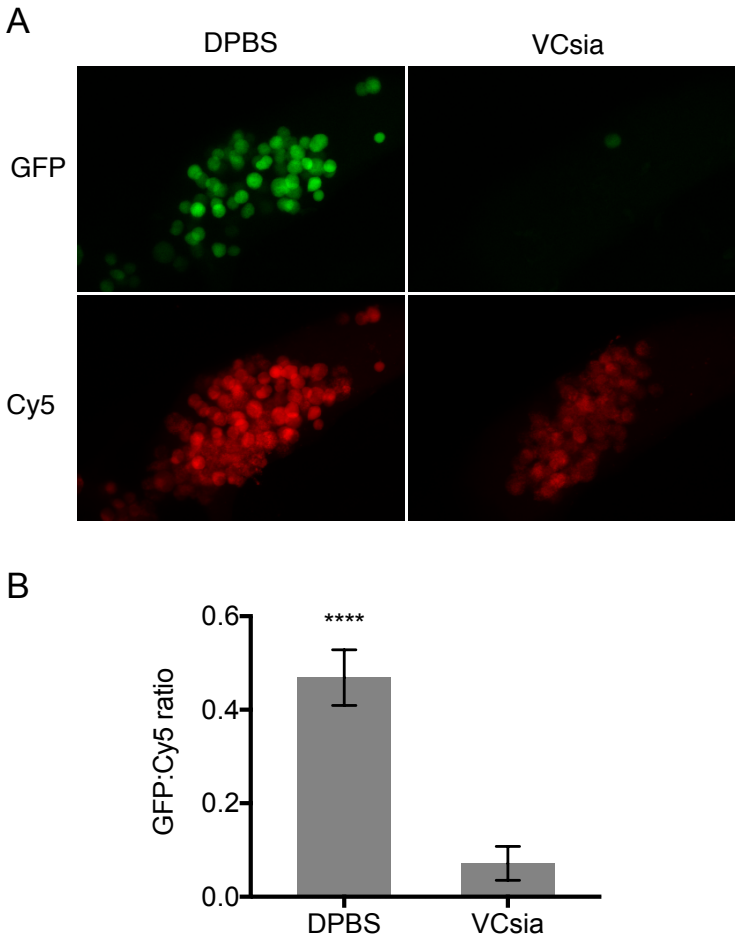

Figure 3.8. Sialidase-treatment induces cell death shortly after transplantation in zebrafish hindbrain. (A) Hindbrain images at 4 hpi for GFP-expressing M4A4 cells (GFP) treated with sialidase or DPBS and strained with CellTracker Deep Red (Cy5). (B) Ratio (vol:vol) of GFP signal to CellTracker Deep Red signal (Cy5) at 4 hpi timepoint. Error bars represent SEM (n=12-16). ****$p < 0.0005$.

This observation was discouraging, as it opens the possibility that factors such as macrophage recruitment are in response to this early cell death rather than stemming from specific recognition events. To further pinpoint the timing of cell death, a mock transplantation protocol was performed in which viability was measured after cells were subjected to conditions analogous to preparation for injection. After treatment with varying doses of VCsia, M4A4 cells were allowed to incubate in PBS at room temperature for an hour. A subsequent viability assay revealed only slight differences in cell survival due to sialidase treatment, of much lesser magnitude than observed *in vivo* (Figure 3.9). While these results complicate interpretation of previous experiments, they are also intriguing in that they represent an avenue for sialic acid-dependent cancer cell death in zebrafish.

Whether the nature of this is immunological, cell signaling, biophysical, or by other mechanisms will be the subject of future studies.

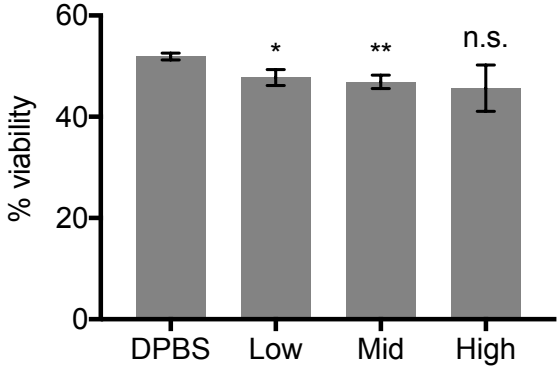

Figure 3.9. Cell viability with *V. cholerae* sialidase treatment. GFP-expressing M4A4 cells treated with 0, 2.5, 5, or 10 μg/mL (DPBS control, low, mid, high) *V. cholerae* sialidase for 1 h were stained with ethidium homodimer-1 and analyzed by flow cytometry. Cells with high FL1 signal and low FL4 signal were considered viable. Error bars represent SD (n=3); p-values are calculated compared to DPBS control. *$p < 0.05$, ** $p < 0.005$.

Synthetic glycopolymers to study altered glycosylation in a zebrafish model of metastasis

An in-depth study of possible sialic acid-mediated cancer-immune interactions in zebrafish might benefit from a model less perturbative to early cancer cell survival. An alternative strategy is to artificially boost sialic acid levels rather than reducing them through sialidase treatment. This can be achieved through the use of glycoprotein-mimicking synthetic glycopolymers. We previously applied a glycopolymer-based approach to study cancer glycosylation in zebrafish, where mucin mimetics composed of a synthetic polymer decorated with GalNAc residues enhanced viability when incorporated into the surface of non-malignant cells.[41] In this study, mucin mimetics bearing cholesterylamine (CholA) anchors were imbedded into the membranes of MCF10A human breast epithelial cells, and their survival in zebrafish embyros was monitored (Figure 3.10). To explore the role of sialylation, a similar approach can be envisioned using sialic acid-modified polymers. Sialylated glycopolymers have been utilized previously to modulate immune cell activity against cancer cells *in vitro*.[14] Additionally, the ability to examine the contribution of specific sialoglycan epitopes to cancer survival through their incorporation into polymers makes this strategy an attractive focus for future exploration.

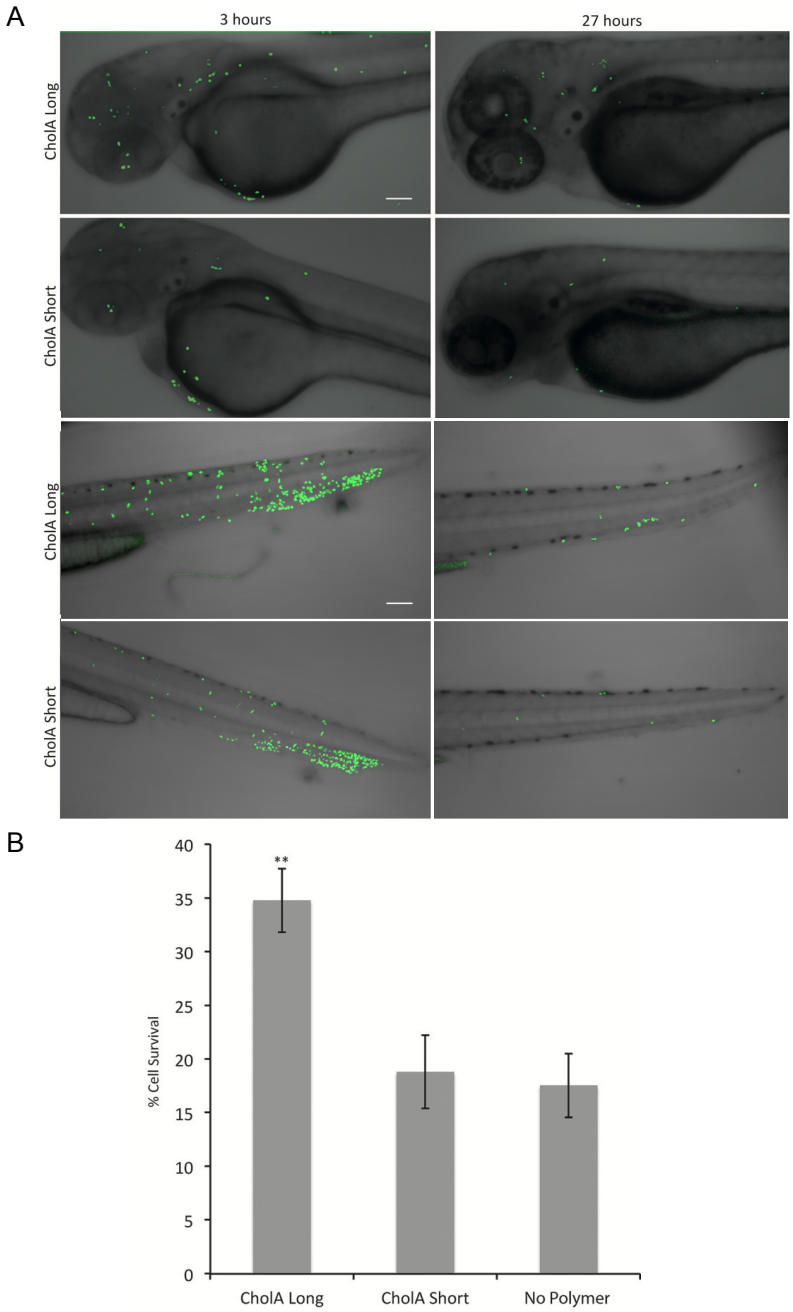

Figure 3.10. Survival of glycopolymer-treated cancer cells in zebrafish. (A) Head and tail images of embryos injected at 48 hpf with GFP-H2-expressing MCF10A cells treated with long (90 nm) or short (3 nm) glycopolymers. (B) Cell survival at 27 hour timepoint for cells treated with long or short glycopolymers, or PBS control. Figure 3.10 adapted with permission from reference (41), copyright 2015 WILEY-VCH Verlag GmbH & Co. KGaA, Weinheim.

Conclusion

In efforts to understand how cancer sialylation influences innate immune activity, a zebrafish xenograft model has shown some promise. Sialidase removal of cancer cell surface sialic acid correlates with lowered cell survival, as well as increased recruitment of macrophages and neutrophils to the transplantation site. This is indicative that, as in mammalian systems, sialic acid confers protective benefits to cancer within zebrafish embryos, motivating further advancement of zebrafish models to study cancer sialylation. A limitation of the strategy employed here is that sialidase treatment induced significant and rapid cell death within only a few hours of cancer cell introduction, raising questions as to the mechanism of observed killing, as the greatest differences in immune cell recruitment did not emerge until later. A more precision-based sialylated glycopolymer approach may aid in the determination of specific cancer-immune interactions.

Materials and Methods

Tissue Culture

PC3, DU145, M4A4-GFP, and CL16-GFP cells were obtained from American Type Culture Collection. PC3 cells were cultured in Ham's F-12 medium. DU145 cells were culture in Eagle's Minimum Essential Medium. M4A4-GFP and CL16-GFP cells were cultured in Dulbecco's Modified Eagle's Medium. All media was supplemented with 10% fetal bovine serum (FBS), 100 units/mL penicillin and 100 µg/mL streptomycin. M4A4-GFP and CL16-GFP media was supplemented with 600 µg/mL geneticin. Cells were maintained at 37 °C and 5% CO_2 in a water-saturated incubator.

Sialidase Treatment of Cancer Cell Lines

V. cholerae was obtained as described previously.[15] Adherent cells were lifted using 2 mM EDTA in PBS and washed three times with DPBS containing Ca^{2+} and Mg^{2+}. Cells were suspended in 1 mL of *V. cholerae* sialidase solution, 10 µg/mL in DPBS containing Ca^{2+} and Mg^{2+}, and incubated at 37 °C for 1 h. After washing with PBS, cells were incubated with SNA-I DyLight 649 conjugate (EY Laboratories, San Mateo, CA) (10 µg/mL in PBS containing 0.5% FBS) at 0 °C for 30 min. Cells were then analyzed by flow cytometry.

For injection into zebrafish embryos, cells were treated with *V. cholerae* sialidase, as described above, or vehicle prior to preparation for injection.

For dose-dependent viability testing, cells were treated with *V. cholerae* sialidase at 0, 2.5, 5, or 10 µg/mL in DPBS containing Ca^{2+} and Mg^{2+} as described above. Cells were incubated with 8 µM ethidium homodimer-1 in PBS and analyzed by flow cytometry.

Incorporation of ManNAz into Cell Lines

Ac_4ManNAz or Ac_4ManNAc were synthesized as described previously.[42] Cells were passaged in appropriate media and solutions Ac_4ManNAz or Ac_4ManNAc in DMSO were added to a final concentration of 100 µM sugar and 0.5% DMSO and allowed to incubate for 3 d. Cells were lifted using a cell scraper and suspended in 0.5 mL DBCO-$(PEG)_4$-biotin (Click Chemistry Tools), 10 µM solution in FACS buffer (PBS with 1% FBS) and 0.1% DMSO, and allowed to incubate at 37 °C for 1 h. Cells were washed twice and incubated 200 µL streptavidin-APC solution (Thermo Fisher Scienfitic), 200-fold dilution in FACS buffer, 20 min at 0 °C. Cells were washed twice and analyzed by flow cytometry.

Zebrafish Husbandry

Wild type AB zebrafish were obtained from Zebrafish International Resource Center. Transgenic lines mfap4:YFP, mfap4:tdtomato, and lysC:dsred, were

obtained from David Tobin, Duke University. Adult zebrafish were kept at 28.5 °C on a 14-h light/10-h dark cycle. Embryos were obtained from natural spawning and maintained at 28.5 °C in embryo medium (EM; 150 mM NaCl, 0.5 mM KCl, 1.0 mM $CaCl_2$, 0.37 mM KH_2PO_4, 0.05 mM Na_2HPO_4, 2.0 mM $MgSO_4$, 0.71 mM $NaHCO_3$ in deionized water, pH 7.4) containing N-phenylthiourea (PTU; 0.2 mM). At 24 hours post fertilization (hpf), embryos were dechorionated manually using forceps. Embryos were developmentally staged according to Kimmel and coworkers.[43] Experiments involving zebrafish were performed in accordance with Stanford University Institutional Animal Care and Use Committee under APLAC protocol #30262.

Morpholino Injections

Pu.1 morpholino mixture was obtained from Gene Tools, LLC. Morpholino mixture was injected into the yolk of embryos at the 1-2 cell stage at aforementioned concentrations. Morphants were obtained as described previously.[44] Morpholino mixture was composed of 0.375 mM/0.025 mM, 0.750 mM/0.050 mM, or 1.500 mM/0.100 mM initiation/exon morpholino. Phenol red was added to a final concentration of 2 mg/mL in 0.2 M KCl and 5 nL of pu.1 morpholino mixture were injected per embryo.

CellTracker Labeling

Prior to sialidase treatment, cells were stained with 25 μM CellTracker Deep Red (Thermo Fisher Scientific) according to manufacturer's instructions.

Human Cancer Cell Xenotransplantation

At 48 hpf, zebrafish embryos were anesthetized in EM containing PTU (0.2 mM) and tricaine (2.4 mM). Cells were suspended in a minimal amount of PBS and into a borosilicate needle and approximately 50 cells were injected into each the hindbrain. After injection of cells, embryos were incubated at 28.5 °C in EM containing PTU (0.2 mM) for 1 h and subsequently transferred to an incubator maintained at 32 °C.

Confocal Microscopy and Image Analysis

Embryos were anesthetized in EM containing PTU (0.2 mM) and tricaine (2.4 mM) and mounted glass slides or glass-bottom well plates in 0.75% agarose. Fluorescence imaging was performed using a Nikon A1R confocal microscrope. For longitudinal studies, embryos were demounted after imaging and maintained at 32 °C in EM containing PTU (0.2 mM). Subsequent imaging was performed according to the same procedure. Fluorescence microscopy images were analyzed using Imaris x64 v8.4.0 (Bitplane).

Supplementary Figures

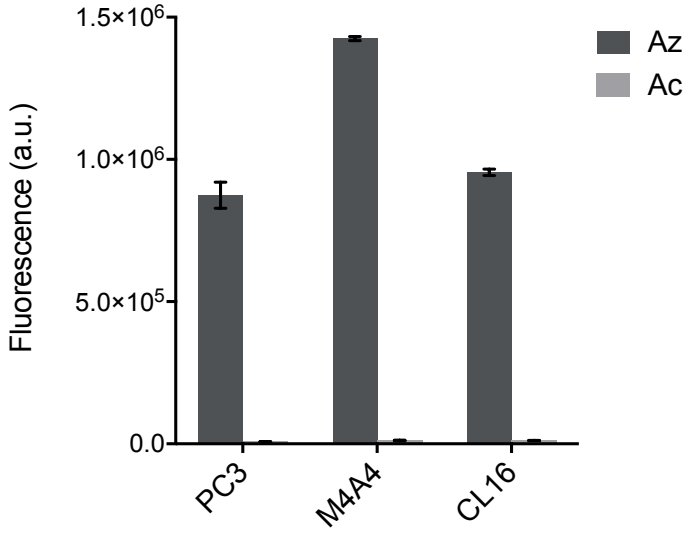

Figure S3.1. ManNAz incorporation in various cancer cell lines. Cells were incubated with Ac_4ManNAz or Ac_4ManNAc (100 μM) 3 d followed by reaction with DBCO-biotin and streptavidin-APC. Error bars represent SD (n=3).

References

(1) *Essentials of Glycobiology*, 2nd ed.; Varki, A., Cummings, R. D., Esko, J. D., Freeze, H. H., Stanley, P., Bertozzi, C. R., Hart, G. W., Etzler, M. E., Eds.; Cold Spring Harbor Laboratory Press: Cold Spring Harbor, 2009.

(2) Schneider, F.; Kemmner, W.; Haensch, W.; Franke, G.; Gretschel, S.; Karsten, U.; Schlag, P. M. Overexpression of Sialyltransferase CMP-Sialic acid:Galβ1,3GalNAc-R α6-Sialyltransferase Is Related to Poor Patient Survival in Human Colorectal Carcinomas. *Cancer Res.* **2001**, *61*, 4605–4611.

(3) Wu, H.; Shi, X. L.; Zhang, H. J.; Song, Q. J.; Yang, X. B.; Hu, W. D.; Mei, G. L.; Chen, X.; Mao, Q. S.; Chen, Z. Overexpression of ST3Gal-I Promotes Migration and Invasion of HCCLM3 in Vitro and Poor Prognosis in Human Hepatocellular Carcinoma. *Onco. Targets. Ther.* **2016**, *9*, 2227–2236.

(4) Schultz, M. J.; Swindall, A. F.; Bellis, S. L. Regulation of the Metastatic Cell Phenotype by Sialylated Glycans. *Cancer Metastasis Rev.* **2012**, *31*, 501–518.

(5) Büll, C.; Stoel, M. A.; Den Brok, M. H.; Adema, G. J. Sialic Acids Sweeten a Tumor's Life. *Cancer Res.* **2014**, *74*, 3199–3204.

(6) Pearce, O. M. T.; Läubli, H. Sialic Acids in Cancer Biology and Immunity. *Glycobiology* **2015**, *26*, 111–128.

(7) Swindall, A. F.; Bellis, S. L. Sialylation of the Fas Death Receptor by St6Gal-I Provides Protection against Fas-Mediated Apoptosis in Colon Carcinoma Cells. *J. Biol. Chem.* **2011**, *286*, 22982–22990.

(8) Zhuo, Y.; Bellis, S. L. Emerging Role of α2,6-Sialic Acid as a Negative Regulator of Galectin Binding and Function. *J. Biol. Chem.* **2011**, *286*, 5935–5941.

(9) Sanchez-Ruderisch, H.; Detjen, K. M.; Welzel, M.; André, S.; Fischer, C.; Gabius, H.-J.; Rosewicz, S. Galectin-1 Sensitizes Carcinoma Cells to Anoikis via the Fibronectin Receptor α5β1-Integrin. *Cell Death Differ.* **2011**, *18* (5), 806–816.

(10) Läubli, H.; Borsig, L. Selectins Promote Tumor Metastasis. *Semin. Cancer Biol.* **2010**, *20*, 169–177.

(11) Macauley, M. S.; Crocker, P. R.; Paulson, J. C. Siglec-Mediated Regulation of Immune Cell Function in Disease. *Nat. Rev. Immunol.* **2014**, *14*, 653–666.

(12) Mohan, B.; Crocker, P. R. Sialylation and Immune Surveillance of Cancer by Siglecs. In *Glycosignals in Cancer: Mechanisms of Malignant Phenotypes*; Furukawa, K., Fukuda, M., Eds.; Springer Japan: Tokyo, 2016; pp 125–138.

(13) Jandus, C.; Boligan, K. F.; Chijioke, O.; Liu, H.; Dahlhaus, M.; Démoulins, T.; Schneider, C.; Wehrli, M.; Hunger, R. E.; Baerlocher, G. M.; et al. Interactions between Siglec-7 / 9 Receptors and Ligands Influence NK Cell – Dependent Tumor Immunosurveillance. *J. Clin. Invest.* **2014**, *124*, 1810–1820.

(14) Hudak, J. E.; Canham, S. M.; Bertozzi, C. R. Glycocalyx Engineering Reveals a Siglec-Based Mechanism for NK Cell Immunoevasion. *Nat. Chem. Biol.* **2014**, *10*, 69–75.
(15) Xiao, H.; Woods, E. C.; Vukojicic, P.; Bertozzi, C. R. Precision Glycocalyx Editing as a Strategy for Cancer Immunotherapy. *Proc. Natl. Acad. Sci. U. S. A.* **2016**, *113*, 10304–10309.
(16) Feng, Y.; Martin, P. Imaging Innate Immune Responses at Tumour Initiation: New Insights from Fish and Flies. *Nat Rev Cancer* **2015**, *15*, 556–562.
(17) Novoa, B.; Figueras, A. Current Topics in Innate Immunity II. *Adv. Exp. Med. Biol.* **2012**, *946*, 253–275.
(18) Feng, Y.; Santoriello, C.; Mione, M.; Hurlstone, A.; Martin, P. Live Imaging of Innate Immune Cell Sensing of Transformed Cells in Zebrafish Larvae: Parallels between Tumor Initiation and Wound Inflammation. *PLoS Biol.* **2010**, *8*, e1000562.
(19) He, S.; Lamers, G. E. M.; Beenakker, J. W. M.; Cui, C.; Ghotra, V. P. S.; Danen, E. H. J.; Meijer, A. H.; Spaink, H. P.; Snaar-Jagalska, B. E. Neutrophil-Mediated Experimental Metastasis Is Enhanced by VEGFR Inhibition in a Zebrafish Xenograft Model. *J. Pathol.* **2012**, *227*, 431–445.
(20) Yang, X. J.; Chen, G. L.; Yu, S. C.; Xu, C.; Xin, Y. H.; Li, T. T.; Shi, Y.; Gu, A.; Duan, J. J.; Qian, C.; et al. TGF-β1 Enhances Tumor-Induced Angiogenesis via JNK Pathway and Macrophage Infiltration in an Improved Zebrafish Embryo/xenograft Glioma Model. *Int. Immunopharmacol.* **2013**, *15*, 191–198.
(21) Sanderson, L. E.; Chien, A. T.; Astin, J. W.; Crosier, K. E.; Crosier, P. S.; Hall, C. J. An Inducible Transgene Reports Activation of Macrophages in Live Zebrafish Larvae. *Dev. Comp. Immunol.* **2015**, *53*, 63–69.
(22) Wang, J.; Cao, Z.; Zhang, X. M.; Nakamura, M.; Sun, M.; Hartman, J.; Harris, R. A.; Sun, Y.; Cao, Y. Novel Mechanism of Macrophage-Mediated Metastasis Revealed in a Zebrafish Model of Tumor Development. *Cancer Res.* **2015**, *75*, 306–315.
(23) Hall, C.; Flores, M. V.; Storm, T.; Crosier, K.; Crosier, P. The Zebrafish Lysozyme C Promoter Drives Myeloid-Specific Expression in Transgenic Fish. *BMC Dev Biol* **2007**, *7*, 42.
(24) Walton, E. M.; Cronan, M. R.; Beerman, R. W.; Tobin, D. M. The Macrophage-Specific Promoter mfap4 Allows Live, Long-Term Analysis of Macrophage Behavior during Mycobacterial Infection in Zebrafish. *PLoS One* **2015**, *10*, e0138949.
(25) Angata, T.; Tabuchi, Y.; Nakamura, K.; Nakamura, M. Siglec-15: An Immune System Siglec Conserved throughout Vertebrate Evolution. *Glycobiology* **2007**, *17*, 838–846.
(26) Hiruma, Y.; Hirai, T.; Tsuda, E. Siglec-15, a Member of the Sialic Acid-Binding Lectin, Is a Novel Regulator for Osteoclast Differentiation. *Biochem. Biophys. Res. Commun.* **2011**, *409*, 424–429.
(27) Ishida-Kitagawa, N.; Tanaka, K.; Bao, X.; Kimura, T.; Miura, T.; Kitaoka, Y.; Hayashi, K.; Sato, M.; Maruoka, M.; Ogawa, T.; et al. Siglec-15 Protein

Regulates Formation of Functional Osteoclasts in Concert with DNAX-Activating Protein of 12 kDa (DAP12). *J. Biol. Chem.* **2012**, *287*, 17493–17502.

(28) Hiruma, Y.; Tsuda, E.; Maeda, N.; Okada, A.; Kabasawa, N.; Miyamoto, M.; Hattori, H.; Fukuda, C. Impaired Osteoclast Differentiation and Function and Mild Osteopetrosis Development in Siglec-15-Deficient Mice. *Bone* **2013**, *53*, 87–93.

(29) Kameda, Y.; Takahata, M.; Mikuni, S.; Shimizu, T.; Hamano, H.; Angata, T.; Hatakeyama, S.; Kinjo, M.; Iwasaki, N. Siglec-15 Is a Potential Therapeutic Target for Postmenopausal Osteoporosis. *Bone* **2015**, *71*, 217–226.

(30) Shimizu, T.; Takahata, M.; Kameda, Y.; Endo, T.; Hamano, H.; Hiratsuka, S. Sialic Acid-Binding Immunoglobulin-like Lectin 15 (Siglec-15) Mediates Periarticular Bone Loss, but Not Joint Destruction, in Murine Antigen-Induced Arthritis. *Bone* **2015**, *79*, 65–70.

(31) Takamiya, R.; Ohtsubo, K.; Takamatsu, S.; Taniguchi, N.; Angata, T. The Interaction between Siglec-15 and Tumor-Associated Sialyl-Tn Antigen Enhances TGF-β Secretion from Monocytes/macrophages through the DAP12-Syk Pathway. *Glycobiology* **2013**, *23*, 178–187.

(32) Corfield, a P.; Higa, H.; Paulson, J. C.; Schauer, R. The Specificity of Viral and Bacterial Sialidases for alpha(2-3)- and alpha(2-6)-Linked Sialic Acids in Glycoproteins. *Biochim. Biophys. Acta* **1983**, *744* (2), 121–126.

(33) Rogerieux, F.; Belaise, M.; Terzidis-Trabelsi, H.; Greffard, A.; Pilatte, Y.; Lambré, C. R. Determination of the Sialic Acid Linkage Specificity of Sialidases Using Lectins in a Solid Phase Assay. *Anal. Biochem.* **1993**, *211*, 200–204.

(34) Nicoll, G.; Avril, T.; Lock, K.; Furukawa, K.; Bovin, N.; Crocker, P. R. Ganglioside GD3 Expression on Target Cells Can Modulate NK Cell Cytotoxicity via Siglec-7-Dependent and -Independent Mechanisms. *Eur. J. Immunol.* **2003**, *33*, 1642–1648.

(35) Wu, Z. J.; Miller, E.; Agbandje-McKenna, M.; Samulski, R. J. α2,3 and α2,6 N-Linked Sialic Acids Facilitate Efficient Binding and Transduction by Adeno-Associated Virus Types 1 and 6. *J. Virol.* **2006**, *80*, 9093–9103.

(36) Bork, K.; Horstkorte, R.; Weidemann, W. Increasing the Sialylation of Therapeutic Glycoproteins: The Potential of the Sialic Acid Biosynthetic Pathway. *J. Pharm. Sci.* **2009**, *98*, 3499–3508.

(37) Rhodes, J.; Hagen, A.; Hsu, K.; Deng, M.; Liu, T. X.; Look, A. T.; Kanki, J. P. Interplay of pu.1 and Gata1 Determines Myelo-Erythroid Progenitor Cell Fate in Zebrafish. *Dev. Cell* **2005**, *8* (1), 97–108.

(38) Su, F.; Juarez, M. a; Cooke, C. L.; Lapointe, L.; Shavit, J. a; Yamaoka, J. S.; Lyons, S. E. Differential Regulation of Primitive Myelopoiesis in the Zebrafish by Spi-1/Pu.1 and C/ebp1. *Zebrafish* **2007**, *4*, 187–199.

(39) Jadus, M. R.; Irwin, M. C.; Irwin, M. R.; Horansky, R. D.; Sekhon, S.; Pepper, K. a; Kohn, D. B.; Wepsic, H. T. Macrophages Can Recognize and Kill Tumor Cells Bearing the Membrane Isoform of Macrophage Colony-Stimulating Factor. *Blood* **1996**, *87*, 5232–5241.

(40) Powell, D. R.; Huttenlocher, A. Neutrophils in the Tumor Microenvironment. *Trends Immunol.* **2016**, *37*, 41–52.
(41) Woods, E. C.; Yee, N. A.; Shen, J.; Bertozzi, C. R. Glycocalyx Engineering with a Recycling Glycopolymer That Increases Cell Survival in Vivo. *Angew. Chemie Int. Ed.* **2015**, *54*, 15782–15788.
(42) Laughlin, S. T.; Bertozzi, C. R. Metabolic Labeling of Glycans with Azido Sugars and Subsequent Glycan-Profiling and Visualization via Staudinger Ligation. *Nat. Protoc.* **2007**, *2*, 2930–2944.
(43) Kimmel, C. B.; Ballard, W. W.; Kimmel, S. R.; Ullmann, B.; Schilling, T. F. Stages of Embryonic Development of the Zebrafish. *Dev. Dyn.* **1995**, *203*, 253–310.
(44) Cambier, C. J.; Takaki, K. K.; Larson, R. P.; Hernandez, R. E.; Tobin, D. M.; Urdahl, K. B.; Cosma, C. L.; Ramakrishnan, L. Mycobacteria Manipulate Macrophage Recruitment through Coordinated Use of Membrane Lipids. *Nature* **2014**, *505*, 218–222.

Chapter 4

An Engineered Riboflavin-binding Protein for Self-labeling with Acrylamidoflavin Fluorophores

Chapter 4. An Engineered Riboflavin-binding Protein for Self-labeling with Acrylamidoflavin Fluorophores

Introduction

Fluorescence-based measurements are widely used to study biological processes over multiple scales of time, distance and molecular hierarchy. Genetically encoded fluorescent protein tags have proven especially useful for these studies as they allow for sensitive and selective imaging of proteins in living cells and tissue.[1,2] In addition to the well-known green fluorescent protein, the labeling of specific proteins with fluorescent tags has also been realized using hybrid systems, where an extrinsic probe is coupled *in situ* to an encoded self-labeling enzyme.[3] The advantage of this latter labeling approach is that one can append fluorophores and other molecular cargo to the enzyme that interact directly with targets in the cytoplasmic milieu. Amongst these self-labeling tags are the SNAP-tag,[4] CLIP-tag,[5] and HaloTag[6] that can be selectively labeled with fluorescent suicide inhibitor-like probe molecules. A well-recognized limitation of these enzymes is their large size (~20-42 kDa), which can cause interference with the native activity of the tagged protein of interest.[7] An alternative self-labeling platform was recently developed by Hoepker et al., in which a low molecular weight protein, lumazine binding protein (LUMP), is engineered to bind tightly and specifically to an endogenous small molecule fluorescent cofactor, which is accompanied by increases in the quantum yield, lifetime and other photophysical properties.[8] In this study we extend this approach to a riboflavin-binding protein, which is engineered from the N-terminal domain of *Escherichia coli* riboflavin synthase. The modified enzyme has a mass of 10.7 kDa, and is shown to be labeled chemically by spectroscopically robust flavin-derived fluorophores to produce one of the smallest genetically encoded fluorescent proteins in mammalian cells.

Riboflavin synthase catalyzes the conversion of 6,7-dimethyl-8-ribityllumazine into riboflavin in the final step of riboflavin biosynthesis.[9] Drawing inspiration from existing self-labeling enzymes, we sought to engineer riboflavin synthase as a new class of self-labeling tag, first by reducing the size of the protein scaffold, and second by installing a reactive cysteine residue proximal to the native binding pocket that would allow for the conjugation of a new class of thiol-reactive riboflavin-based fluorophore. Flavins and related isoalloxazines are ubiquitous in nature, where they serve vital roles as cofactors in oxidoreductases and photosensory proteins.[10,11] The well-characterized absorption and fluorescence properties of flavins, coupled with excellent photostability when bound to certain flavin-binding proteins make them ideal probes for fluorescence imaging applications *in vitro* and *in vivo*.[12,13] The covalent attachment of flavins to riboflavin synthase was realized in this study by appending an acrylamide group to the isoalloxazine ring and by introducing a cysteine residue in the flavin-binding pocket, whereby noncovalent association accelerates the conjugation reaction (Figure 4.1). The acrylamide group has previously been utilized as a

reactive handle to introduce probe molecules into proteins harboring an unnatural amino acid (e.g., *N*-acryloyl-L-lysine) via Michael addition and phospha-Michael addition reactions with thiol and phosphine probes, respectively.[14,15] Additionally, acrylamide-tethered nucleobases have been incorporated into DNA for cysteine-mediated crosslinking with DNA-binding proteins.[16] Furthermore, acrylamides have been shown to react sluggishly with biological thiol nucleophiles including glutathione, a key feature for reducing nonspecific background labeling.[17]

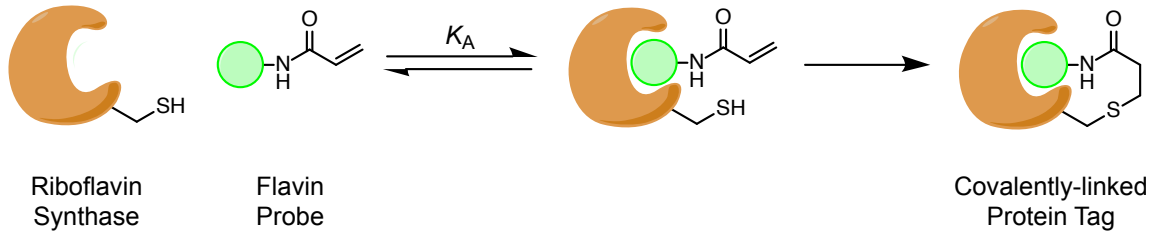

Figure 4.1. Covalent ligation of acrylamide-modified flavins to an engineered riboflavin synthase.

Herein we introduce a new class of self-labeling riboflavin-binding proteins through the rational design and modification of the binding pocket of riboflavin synthase in order to enhance the covalent labeling efficiency of an engineered cysteine residue with novel acrylamido-flavin probes. Spectroscopic and biochemical characterization of the labeling reaction reveals the bioconjugation of the acrylamide group of the flavin-analog to riboflavin synthase proceeds selectively under biologically relevant conditions in studies that demonstrate the suitability of this protein-labeling platform to *in vitro* and cellular environments. The low molecular weight of riboflavin synthase, coupled with its long wavelength emission (green/yellow) and excited state lifetime, increases the capabilities of our previously described LUMP tag for anisotropy, lifetime and FRET-based imaging and analysis of specifically tagged proteins and their complexes *in vitro* and *in vivo*.

Results

Design of Monomeric Riboflavin Synthase as a Bioconjugation Scaffold

Native homodimeric N-terminal riboflavin synthase (RS) from *E. coli* (truncated construct spanning residues 1-97) was envisaged as a protein scaffold that through site-directed mutagenesis could be further reduced in size by disrupting the dimerization interface. Gleaning from the available crystal structure of homodimeric RS (PDB: 1PKV) it was readily apparent that three asparagine residues (N45, N72, N83) created an important hydrogen-bonding network as a

critical driving force of homodimerization. Single mutations N45G and N72D were only partially successful in generating the monomeric species (~10%) as evidenced by clearly resolved peaks of dimer and monomer in size exclusion chromatography. The double mutant (N72D, N83A) resulted in complete conversion from the dimeric to the monomeric form of RS. While native riboflavin binds tightly to homodimeric RS within bacteria and remains bound during protein purification, it no longer visibly binds to monomeric RS as evidenced by the absence of riboflavin fluorescence. We surmised that the second RS subunit contributes significantly to the binding affinity of riboflavin. We envisioned favorable noncovalent binding of the flavin fluorophore to RS as a critical prerequisite for an efficient self-labeling strategy because the overall rate of conjugation would be greatly accelerated due to increased local concentration of cysteine and reactive probe within the binding pocket. To compensate for the loss in riboflavin binding to the monomer, we introduced mutation M64F (RS-A) to increase hydrophobic contacts between phenylalanine and the isoalloxazine ring system. RS-A was copurified with a small fraction of natively bound riboflavin as evidenced by a weak riboflavin-specific spectroscopic signature. The purified protein was confirmed to be monomeric by size exclusion chromatography. Encouraged by the increase in riboflavin binding, we investigated other mutations that could increase the binding by further increasing hydrophobic contacts with the planar isoalloxazine fluorophore. Mutation S41F (RS-B) proved insightful. Protein RS-B was isolated from *E. coli* with natively bound 6,7-dimethyl-8-ribityllumazine (lumazine), the biosynthetic precursor to riboflavin, albeit as the dimeric form of RS. Lumazine was tentatively identified as the bound cofactor based on its characteristic fluorescence emission at 420 nm. This suggests that Phe at position 41 must considerably increase the binding of RS to lumazine, and moreover, that the ribityl group of lumazine assists in the dimerization. Based on these studies, we elected to investigate both RS-A and RS-B as targets for self-labeling proteins in combination with reactive synthetic flavin fluorophores. These RS-flavin conjugates extend the capabilities of our previously described LUMP as universal probe for fluorescence anisotropy (FA)-based measurements of target proteins.

Design of Isoalloxazine Derivative with Cysteine Reactive Group

With a monomeric 10 kDa lumazine-binding protein in hand, we chose to prepare a panel of isoalloxazine analogs with varying methyl substitutions at the C7 and C8 positions (Scheme 4.1). Moreover, installation of a covalent binding group was achieved through replacement of the native ribityl group with an acrylamide group connected to N10 with either a two or three carbon linker. Acrylamide was selected as the reactive handle as alkyl acrylamides have been shown to be poorly reactive with glutathione and other cysteine nucleophiles under physiological conditions[17] – a key attribute for fluorophore stability and diminished nonspecific background labeling. We anticipated that while acrylamide is generally slow to react with cysteine residues, labeling might be

accelerated for a well-positioned cysteine residue located within the RS binding pocket. Moreover, acrylamides have previously been incorporated into proteins as unnatural amino acids allowing for selective labeling using various acrylamide-reactive secondary probes.[14,15]

Using the existing crystallographic data of RS as a starting structure, we computationally explored potential cysteine residues that could react with the acrylamide group via Michael addition. Native C47, C48, and mutant T67C were identified as likely candidates to serve this role.

Finally, a survey of flavin analogs suggested that methyl substitution at the C7 and C8 positions of the isoalloxazine core results in dramatic changes in fluorescence quantum yield, fluorescence lifetime, and absorption/emission wavelengths.[18] We therefore decided to synthesize all four methyl variants of isoalloxazine with terminal acrylamide groups (Scheme 4.1).

Synthesis of Flavin Derivatives

A panel of substituted isoalloxazines bearing an acrylamide functionality was synthesized (Scheme 4.1) for covalent linkage of the riboflavin analog to RS. Briefly, substituted chloronitrobenzenes were reacted with diaminoalkanes followed by reduction of the nitro group and subsequent condensation with alloxan to yield the amine-functionalized isoalloxazine rings. Reaction of these analogs with acryloyl chloride provided access to a panel of acrylamido-flavin compounds.

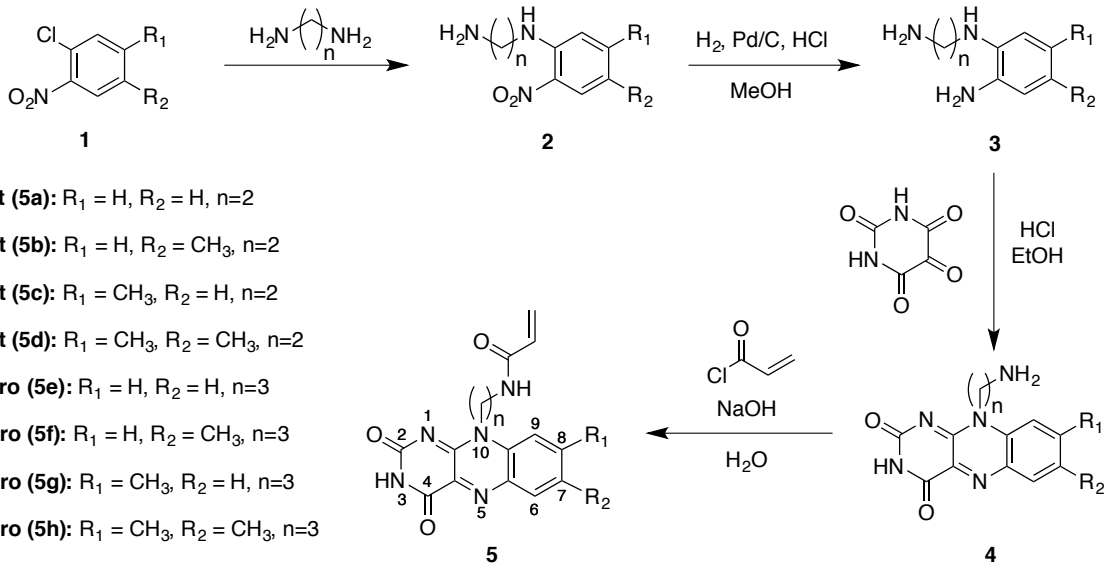

Scheme 4.1. Synthesis of a panel of acrylamide-functionalized flavin analogs.

This synthetic route allowed us to generate isoalloxazine rings bearing a two- or three-carbon linker denoted by suffixes -et and –pro, respectively. This approach also allowed us to vary the methyl substitution pattern at C7 and C8 of the isoalloxazine core (F1-F4) to assess the spectroscopic and steric properties of the probe.

Riboflavin Synthase Bioconjugation Studies

Ligand	Protein	Labeling efficiency (%)	λ_{Ex} (nm)	λ_{Em} (nm)	ε ($M^{-1}cm^{-1}$)
F1et	RS-A	17	439,450 (+0)	521 (+0)	5950
	RS-B	22	450,468 (+12-30)	524 (+3)	
F2et	RS-A	37	452,470 (+1)	533 (-2)	7130
	RS-B	60	452,470 (+1)	535 (+0)	
F3et	RS-A	59	439,450 (+0)	515 (+0)	14200
	RS-B	85	439,450 (+0)	517 (+2)	
F4et	RS-A	11	451,469 (+1)	527 (-1)	2220
	RS-B	26	451,469 (+1)	530 (+2)	
F1pro	RS-A	62	439 (+19)[a]	506 (-7)	11600
	RS-B	50	439 (+19)[a]	510 (-3)	
F2pro	RS-A	90	451,469 (+1)	518 (-11)	9840
	RS-B	90	451,470 (+2)	521 (-8)	
F3pro	RS-A	47	430 (+8)[a]	503 (-5)	11500
	RS-B	53	430 (+20)[a]	509 (+1)	
F4pro	RS-A	36	450,468 (+0)	515 (-9)	5940
	RS-B	57	451,468 (+0)	518 (-6)	

Table 4.1. Labeling efficiencies and optical properties of RS-isoalloxazine conjugates. The shift in excitation and emission wavelengths of the protein conjugate relative to free ligand is reported in parentheses. Molar extinction coefficients (ε) are reported for free ligands. Generally, two excitation peaks are observed whose relative peak heights change upon binding to ligand (see supporting information for all spectra). [a]Only one fluorescence excitation peak is resolved.

Our initial efforts focused on establishing methods to covalently link probes F1et-F4et to RS-A and RS-B via three potential cysteine conjugation sites. To this end, 100 μM of purified RS was treated with a 1 mM solution of the

probe in aqueous buffer at 37 °C for 2 hours. The product was filtered and purified by size exclusion chromatography to remove any free probe. The identity and labeling efficiency of the protein conjugate using each of the eight probes was established by LC/MS. The fluorescence excitation and emission properties of each conjugate were recorded and molar extinction coefficients were derived from absorbance spectra at varying concentrations of the free probe (Figure S4.3). The data are summarized in Table 4.1.

A total of eight protein conjugates were successfully labeled with varying labeling efficiencies. Notably, RS conjugates derived from F1et-F4et were found to exhibit lower fluorescence emission intensities than the free probes. We presumed this to result from out-of-plane movements of N10 as a consequence of the strained linker-to-protein connection that would compromise π-conjugation. This hypothesis was supported by molecular dynamics (MD) simulations of the 2-carbon linker probes (F1et-F4et) showing a distortion in the planarity at the N10 position, as well as the observation that the probes with a 2-carbon linker exhibited dimmer emission than the corresponding 3-carbon linker probes (F1pro-F4pro).

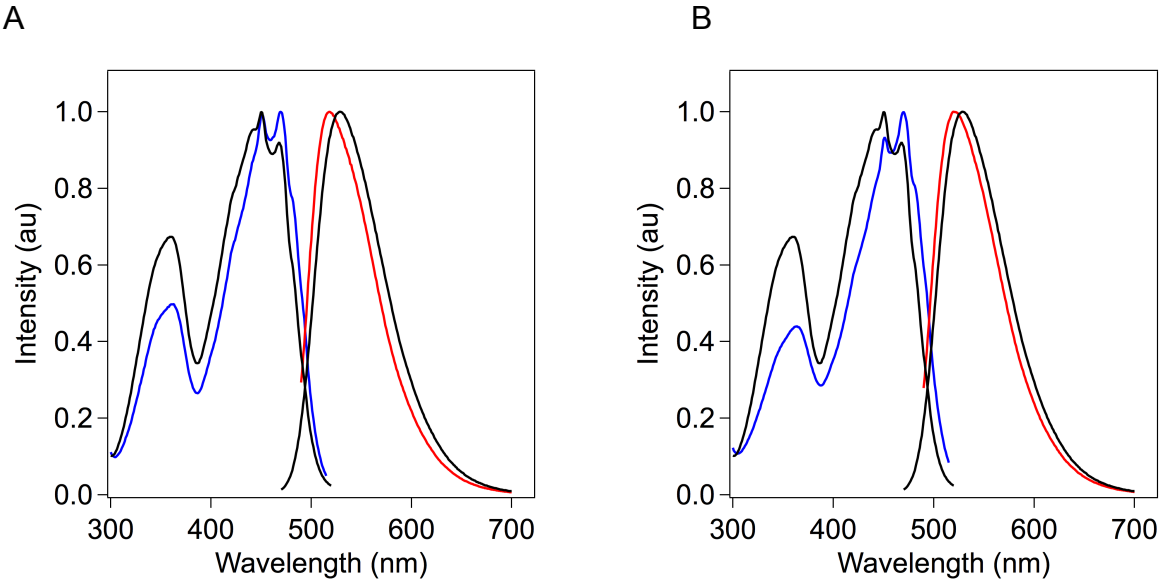

Figure 4.2. Fluorescence spectra of RS-F2pro conjugates. Fluorescence excitation (blue) and emission spectra (red) of protein conjugate superimposed on excitation and emission spectra of free ligand F2pro (black) at 25 °C in aqueous buffer (150 mM NaCl, 20 mM HEPES, pH=7.9). (A) RS-A. (B) RS-B.

The highest labeling efficiencies for the 3-carbon isoalloxazine derivatives were achieved using ligand F2pro with monomethyl substitution at position C7 of the isoalloxazine ring. Quantitative fluorescence analysis of free F2pro and its conjugate with RS-A and RS-B are summarized in Figure 4.2. Upon binding to RS-A, the fluorescence emission wavelength blue-shifts by 11 nm. The two

fluorescence excitation maxima of the probe are unchanged at 451 nm and 469 nm (Table 4.1). The FA value for the same conjugate was measured as 0.21, further indicating that the probe is firmly attached to the protein and exhibits little in the way of librational motions that would decrease the FA value beyond that expected for the tumbling of the RS protein. The fluorescence wavelength shifts (blue shift) further support this conclusion. F2pro was selected for further testing and characterization as it yielded the highest labeling efficiency (Table 4.1).

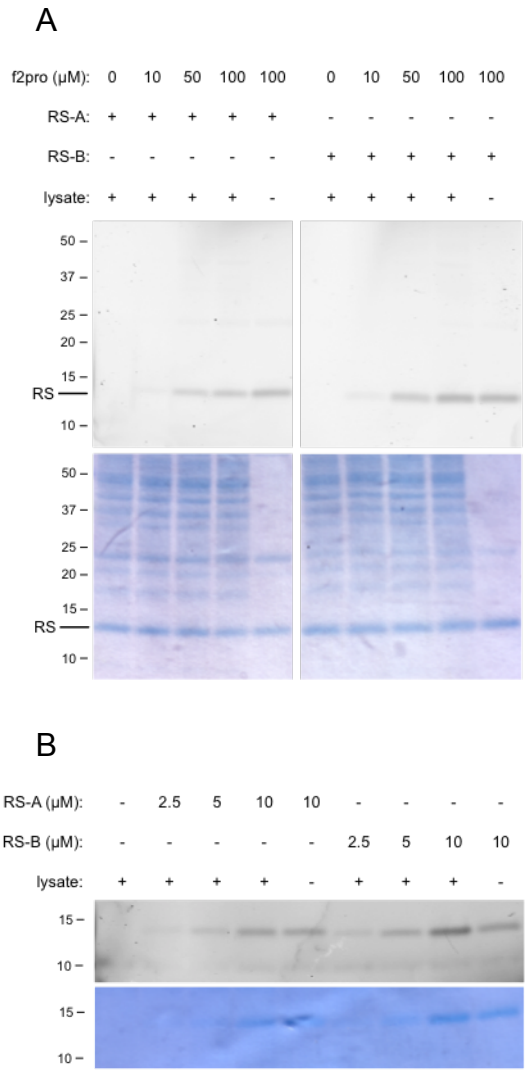

Figure 4.3. Bioconjugation of RS proteins and F2pro in human cell lysate. (A) F2pro dose-dependent labeling of RS-A and RS-B in PC3 cell lysate; 10 μM RS, 0 – 100 μM F2pro. Diffuse fluorescence stain at top of gel resulting from excess F2pro ligand has been cropped for visual clarity. (B) Varying concentrations of RS at constant F2pro concentration; 0 – 10 μM RS, 100 μM F2pro.

Next, we investigated the bioconjugation reaction under conditions representative of the cellular environment. To this end, 10 μM RS-A and RS-B were incubated with varying concentrations of F2pro at 37 °C for 1 hour in cell lysate prepared from PC3 human prostate cancer cells. Results were obtained through direct analysis of the reaction mixtures by SDS-PAGE without purification. Imaging of the gel using a fluorescence scanner showed that reactions with F2pro yielded dose-dependent labeling that was comparable between both RS constructs tested, with a low level of observable background labeling of lysate proteins (Figure 4.3A). This demonstrates that the reaction proceeds selectively even in the presence of competing human cell lysate components. Additionally, we varied the concentration of RS (RS-A and RS-B) with a constant amount of F2pro (100 μM), and observed selective labeling with as little as 2.5 μM of protein (Figure 4.3B). These results demonstrate this labeling platform to be suitable for the study of protein dynamics in cell culture.

Analysis of Probe Attachment Sites in RS Mutants

Peptide mapping of the F2pro conjugates with RS-A and RS-B was performed by denaturing the respective proteins in 6 M urea followed by digestion with Glu-C (New England Biolabs). Subsequent tandem mass spectrometric analysis of peptide fragments showed that the acrylamide is conjugated exclusively to T67C in preference over the wild-type C47 and C48 residues (Figure S4.11).

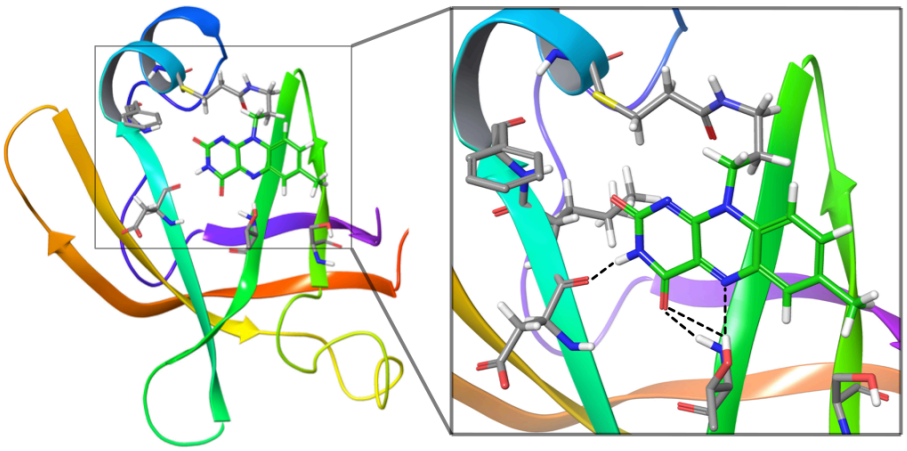

Figure 4.4. Computed structure of RS-A-F2pro. Image obtained from a 50 ns molecular mechanics simulation in a water box (Desmond) and subsequent minimization (Macromodel, Schrödinger Inc.). The hydrogen-bonding network largely matches the native isoalloxazine ligand-binding motif of riboflavin.

To gain a better understanding of how the acrylamide interacts with cysteine residues in each RS mutant, we performed a 50 ns MD simulation in a water box (Desmond in the Maestro suite, Schrödinger Inc) starting with a minimized structure (OPLS 2005) of RS-A linked to the F2pro ligand. The MD simulation was tracked using the RMSD of the backbone, which was found to be largely unchanged after 32 ns. Six structures were selected for further analysis at time-points between 32 ns and 50 ns, and all were found to be structurally similar including the conformations of F2pro and the binding pocket of RS-A. A representative structure of the F2pro-RS conjugate is shown in Figure 4.4. Notably, the 3-carbon linker points towards the interior of the protein while the amide bond is antiparallel with its nitrogen atom directed towards the exterior.

Anisotropy Imaging

Purified RS-A-F2pro was added to aqueous buffer containing a small amount of Ni-NTA agarose beads to be able to individually resolve them by scanning confocal microscopy. RS-F2pro conjugates were found to be attached to the beads via their N-terminal hexa-histidine tag as evidenced by the appearance of fluorescence emission on the bead surface. Images were recorded with a laser scanning confocal microscope and anisotropy images were calculated in Igor Pro (version 6.35, Wavemetrics) using a customized procedure as described previously.[8]

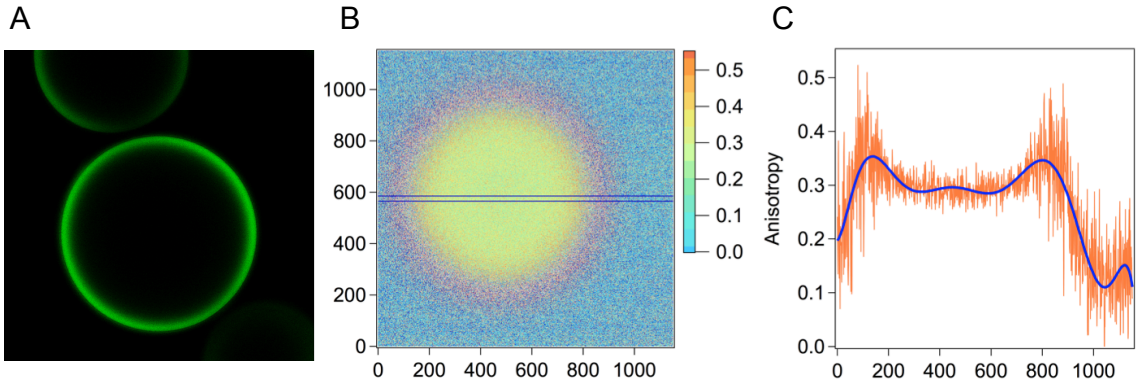

Figure 4.5. Fluorescence anisotropy image of Nickel-NTA agarose beads incubated with hexahistidine-tagged RS-A-F2pro. (A) Fluorescence image of Ni-NTA agarose beads labeled with hexahistidine bearing RS-A conjugated to F2pro. (B) Anisotropy image obtained from P- and S- polarized images using a G-factor of 0.78. (C) Plot profile of horizontal selection (blue rectangle) in (B) superimposed with smoothed line for purpose of visual clarity.

The image shown in Figure 4.5 was recorded from a cross section on the upper hemisphere of the agarose bead – no probe was detected within the interior of the bead. The FA values of the bead bound conjugate were as high as

r = 0.35, which is close to that measured for the limiting (r_0) value of 0.36 measured at infinite viscosity. This result suggests that the RS conjugate is firmly attached to the bead via the His-tag and that the isoalloxazine fluorophore experiences little librational motion. Unbound RS conjugates have FA values (measured outside the bead) of r = 0.21.

The FA value of an appropriately labeled fluorescent protein can be used to quantify the fluorescence lifetime of the unbound RS conjugate sensor. The Perrin-Weber equation expressed in terms of FA is given as:

$$r_0 / r = (1 + \tau_f / \tau_c) \qquad \text{(Eqn 1)}$$

where r is the measured FA value, r_0 is the limiting FA value, τ_f is the excited-state fluorescence lifetime, and τ_c is the rotational correlation time (time to rotate through 1 radian).[19,20] τ_c is related to the hydrodynamic protein volume, V, according to:

$$\tau_c = \eta V / RT \qquad \text{(Eqn 2)}$$

where η is solvent viscosity, R is the gas constant, and T is the temperature in Kelvin.[19,20] For spherical proteins, τ_c will increase by 1 ns for every 2.5 kD in mass and so for RS conjugate (10 kDa) the value will be 4 ns. Thus using a measured r of 0.21 and given r_0 is 0.36 the fluorescence lifetime of the probe in RS is calculated as 2.85 ns.

Discussion

Protein tags that are self-labeled through the addition of exogenous small molecule fluorescent ligands offer many advantages for imaging applications. Advantages include the versatility and choice of fluorophore, the genetically encoded nature of the protein, and the temporal control of emerging fluorescence that is dependent on secondary addition of a fluorescent probe. Like conventional fluorescent protein tags, however, a potential drawback lies in their size, which is typically in excess of 20 kDa and can disrupt the native folding and function of target proteins. We have demonstrated a new scaffold for a self-labeling tag through rational protein engineering of riboflavin synthase to yield a 10 kDa riboflavin-binding protein capable of efficient and selective covalent labeling with synthetic acrylamido-flavin fluorophores. The bioconjugation reaction displays a high degree of selectivity under conditions reflective of the cellular environment even at a low concentration of RS, such that this approach may be readily adapted for labeling in live cells.

The labeling efficiency was found to be tunable through modification of amino acid residues within the binding pocket. In particular, we view the phenylalanine substitutions in RS-A and RS-B to be critical elements for increasing the affinity of lumazine binding to RS monomers, as our earlier studies had indicated both riboflavin and lumazine derive most of their free energy of

binding from interactions with residues on the outer surface of RS and could be susceptible to competition from abundant water molecules resulting in rapid ligand dissociation. We reasoned that shielding and encasing the cofactor using new hydrophobic residues would result in a stronger complex and slow cofactor dissociation from RS. Moreover, we proposed that additional hydrophobic residues in the cofactor binding pocket would allow us to use new flavin analogs with extended π-stacking to red-shift the emission interactions of the RS complex. As expected, the presence of an additional phenylalanine in RS-B conjugates consistently resulted in an observable shift in emission wavelength compared to conjugates of RS-A.

Aside from modifications to the protein scaffold, structural changes to the flavin probes themselves, linker length and methyl substitution pattern in particular, were also found to modulate labeling efficiency. This finding suggests it may be possible to further enhance the reactivity of the probe through alterations in probe design. Notably, within the RS binding pocket, residue C48 is proximal to the arene ring of a bound isoalloxazine and, based on molecular modeling, appears to be well-situated to undergo reaction with an acrylamide located at this position. As such, we are currently exploring the installation of an acrylamide moiety at positions C7 and C8 on the isoalloxazine core to evaluate this alternative site of attachment. Additionally, we are examining other functional groups apart from the acrylamide as reactive handles for bioconjugation. Alkyl chlorides, for instance, can undergo covalent reaction with thiols, yet are generally inert to other biologically relevant nucleophiles.[21] This would result in an even further reduction of background labeling and heightened selectivity and sensitivity.

The RS conjugate with F2pro also shows promise as a fluorescence anisotropy-based sensor, as shown *in vitro* in a bead-binding assay. FA values of 0.21 and 0.35 were obtained for free and surface-immobilized RS, respectively, which approaches the dynamic range achieved using our previously developed LUMP tag.[8] Ongoing efforts are focused on the generation of genetically encoded fusions of RS with proteins of interest. In this manner, an RS tag can act as a self-labeling fluorescent marker and fluorescent anisotropy-based sensor of protein hydrodynamics.

Acknowledgement

This chapter was coauthored with Alexander C. Hoepker and Gerard Marriott.

Materials and Methods

General Synthetic Methods

Reagents and solvents were obtained commercially and used without further purification unless otherwise noted, with the exception of anhydrous solvents which were prepared by the method developed by Pangborn et al.[22] Analytical TLC was performed on SiliCycle glass-backed silica gel 60 Å plates (thickness 250 µm) and detected by UV lamp or ninhydrin staining. Compounds were purified by flash column chromatography using Silicycle Silica Flash P60 silica (40-63 mm, 230-400 mesh) or a Biotage Isolera Prime purification system with Biotage KP-Sil cartridges. Unless otherwise noted, anhydrous magnesium sulfate was used to dry organic extracts and solutions were concentrated by rotary evaporation followed by high vacuum. ^{1}H and ^{13}C-NMR spectra were obtained using Bruker AVB-400, AVQ-400, or AV-600 instruments and shifts are reported in ppm (δ) relative to the solvent peak, while coupling constants (*J*) are reported in hertz (Hz). Electrospray ionization (ESI) and electron ionization (EI) high-resolution mass spectrometry (HRMS) were performed at the University of California, Berkeley QB3/Chemistry Mass Spectrometry Facility.

Synthesis and Characterization of Compounds

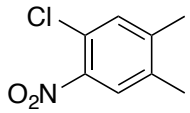

1-chloro-4,5-dimethyl-2-nitrobenzene (1d)

4,5-dimethyl-2-nitroaniline (5.00 g, 30.1 mmol, 1.00 eq) was dissolved in concentrated HCl (75 mL) and cooled by the addition of ice and stirred in an ice bath. $NaNO_2$ (2.30 g, 33.3 mmol, 1.10 eq) in H_2O (7 mL) was added below the surface of the solution over 10 min. The reaction mixture was stirred for an additional 30 min and filtered to yield a red-brown solution of diazonium salt. $CuSO_4 \cdot 5H_2O$ was dissolved in concentrated HCl (25 mL) and cooled by the addition of ice (51 g) and stirred in an ice bath to form a turquoise solution of CuCl. The cold diazonium salt solution was added and the reaction mixture stirred 30 min. The resulting dark green solution was allowed to come to room temperature and stand for 12 h. The solution was concentrated under reduced pressure to a brown solid, which was dissolved in CH_2Cl_2 and washed with H_2O (2x). The organic layer was dried over $MgSO_4$ and the solvent removed under reduced pressure to yield **1d** which was purified by silica gel chromatography (95:5 to 50:50 hexanes:EtOAc). 2.35 g (12.7 mmol, 42%), yellow solid. ^{1}H NMR (400 MHz, $CDCl_3$) δ 7.69 (s, 1H), 7.28 (s, 1H), 2.30 (s, 3H), 2.29 (s, 3H). ^{13}C NMR (101 MHz, $CDCl_3$) δ 143.79, 136.89, 132.56, 130.33, 126.62, 124.23, 19.80, 19.31. EI-HRMS: Calcd for $C_8H_8NO_2Cl^+$ $[M]^+$: 185.0244; found: 185.0246.

***N*-(Aminoethyl)-nitroaniline analogs (2a-h) general procedure**

Ethylenediamine or 1,3-diaminopropane (76 mmol, 6.0 eq) was added to 1-chloro-2-nitrobenzene analog **1a** (2.00 g, 12.7 mmol, 1.0 eq). The reaction mixture was stirred at 120 °C for 24 h and then allowed to come to r.t. The resulting viscous oil was dissolved in $CHCl_3$ and washed with H_2O (2x). The organic layer was dried over $MgSO_4$ and the solvent removed under reduced pressure to give **2a** or **2e**, which were used without further purification.

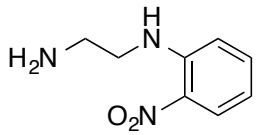

***N*^{1}-(2-Nitrophenyl)ethane-1,2-diamine (2a)**

1.86 g (10.3 mmol, 81%), orange oil. ^{1}H (400 MHz, DMSO-d_6) δ 8.35 (s, 1H), 8.02 (dd, *J*= 8.6, 1.6 Hz, 1H), 7.47 (t, *J*= 7.1 Hz, 1H), 6.98 (d, *J*= 8.5 Hz, 1H), 6.62 (t of d, *J*= 7.1, 1.0 Hz, 1H), 3.28 (quartet, *J*= 5.8 Hz, 2H), 2.84 (t, *J*= 6.2 Hz, 2H); ^{13}C NMR (125 MHz, DMSO-d_6) δ 145.4, 136.4, 130.8, 126.1, 115.2, 114.9, 114.5, 44.9, 40.2; ESI-HRMS: Calcd for $C_8H_{12}N_3O_2^+$ $[M+H]^+$: 182.0924; found: 182.0924.

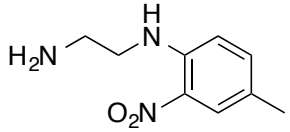

***N*^{1}-(4-Methyl-2-nitrophenyl)ethane-1,2-diamine (2b)**

2.25 g (11.5 mmol, 99%), orange oil. ^{1}H (400 MHz, $CDCl_3$) δ 8.15 (br, 1H), 7.93 (s, 1H), 7.23 (dd, *J*= 8.7, 2.0, 1H), 6.76 (d, *J*= 8.7, 1H), 3.34 (quartet, *J*= 5.8 Hz, 2H), 3.01 (t, *J*= 6.2, 2H), 2.23 (s, 3H); ^{13}C NMR (125 MHz, $CDCl_3$) δ 143.9, 137.8, 131.7, 126.1, 124.1, 113.9, 45.9, 41.0, 20.0; ESI-HRMS: Calcd for $C_9H_{14}N_3O_2^+$ $[M+H]^+$: 196.1081; found: 196.1079.

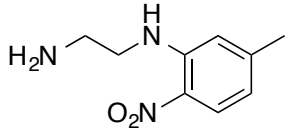

***N*^{1}-(5-Methyl-2-nitrophenyl)ethane-1,2-diamine (2c)**

2.19 g (11.2 mmol, 96%), brown oil. ^{1}H (400 MHz, $CDCl_3$) δ 8.28 (br, 1H), 8.05 (d, *J*= 8.7 Hz, 1H), 6.64 (s, 1H), 6.45 (d, *J*= 8.7 Hz, 1H), 3.37 (quartet, *J*= 5.8, 2H), 3.05 (t, *J*= 6.2 Hz, 2H), 2.34 (s, 3H); ^{13}C NMR (125 MHz, $CDCl_3$) δ 147.6, 145.4, 129.8, 126.5, 116.8, 113.2, 45.4, 40.6, 21.9; ESI-HRMS: Calcd for $C_9H_{14}N_3O_2^+$ $[M+H]^+$: 196.1081; found: 196.1079.

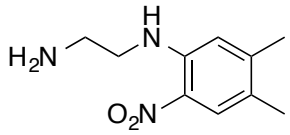

***N*[1]-(4,5-Dimethyl-2-nitrophenyl)ethane-1,2-diamine (2d)**

1.13 g (5.40 mmol, 99%), red oil. ^{1}H (400 MHz, $CDCl_3$) δ 8.16 (br, 1H), 7.94 (s, 1H), 6.65 (s, 1H), 3.38 (quartet, *J*= 5.8 Hz, 2H), 3.05 (t, *J*= 6.2 Hz, 2H), 2.27 (s, 3H), 2.18 (s, 3H); ^{13}C NMR (125 MHz, $CDCl_3$) δ 147.4, 144.3, 130.1, 126.7, 124.7, 114.3, 46.0, 41.1, 20.9, 18.7; ESI-HRMS: Calcd for $C_{10}H_{16}N_3O_2^+$ $[M+H]^+$: 210.1237; found: 210.1235.

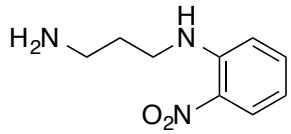

***N*[1]-(2-nitrophenyl)propane-1,3-diamine (2e)**

2.30 g (11.8 mmol, 93%), orange oil. ^{1}H (400 MHz, $CDCl_3$) δ 8.11 (br, 1H), 8.06 (dd, J= 8.6, 1.4 Hz, 1H), 7.35 (t, *J*= 7.1 Hz, 1H), 6.80 (d, *J*= 8.6 Hz, 1H), 6.55 (t, *J*= 7.4 Hz, 1H), 3.32 (quartet, *J*= 6.7 Hz, 2H), 2.82 (t, *J*= 6.7 Hz, 2H), 1.80 (pentet, *J*= 6.8 Hz, 2H); ^{13}C NMR (125 MHz, $CDCl_3$) δ 145.5, 136.2, 131.6, 126.7, 115.0, 113.7, 40.8, 39.7, 32.3; ESI-HRMS: Calcd for $C_9H_{14}N_3O_2^+$ $[M+H]^+$: 196.1081; found: 196.1080.

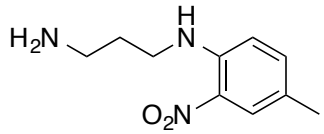

***N*[1]-(4-methyl-2-nitrophenyl)propane-1,3-diamine (2f)**

2.41 g (11.5 mmol, 98%), orange oil. ^{1}H (400 MHz, $CDCl_3$) δ 8.01 (br, 1H), 7.90 (s, 1H), 7.21 (dd, *J*= 8.7, 1.7 Hz, 1H), 6.74 (d, *J*= 8.7 Hz, 1H), 3.33 (quartet, *J*= 6.8, 2H), 2.84 (t, *J*= 6.7 Hz, 2H), 2.20 (s, 3H), 1.81 (pentet, *J*= 6.8 Hz, 2H); ^{13}C NMR (125 MHz, $CDCl_3$) δ 143.9, 137.8, 131.3, 126.0, 124.7, 113.8, 40.9, 39.8, 32.5, 20.0; ESI-HRMS: Calcd for $C_{10}H_{16}N_3O_2^+$ $[M+H]^+$: 210.1237; found: 210.1237.

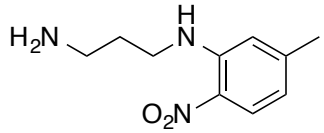

***N*[1]-(5-methyl-2-nitrophenyl)propane-1,3-diamine (2g)**

2.44 g (11.7 mmol, 99%), brown oil. ^{1}H (400 MHz, $CDCl_3$) δ 8.17 (br, 1H), 8.01 (d, *J*= 9.1 Hz, 1H), 6.63 (s, 1H), 6.43 (dd, *J*= 8.7, 1.2 Hz, 1H), 3.37 (quartet, *J*= 6.8 Hz, 2H), 2.88 (t, *J*= 6.8 Hz, 2H), 2.31 (s, 3H), 1.86 (pentet, *J*= 6.8 Hz, 2H); ^{13}C NMR (125 MHz, $CDCl_3$) δ 147.9, 145.7, 130.1, 126.9, 117.1, 113.5, 40.9, 39.9, 32.6, 22.3; ESI-HRMS: Calcd for $C_{10}H_{16}N_3O_2^+$ $[M+H]^+$: 210.1237; found: 210.1237.

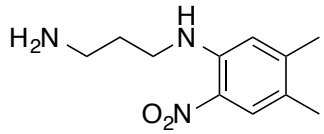

***N*^{1}-(4,5-dimethyl-2-nitrophenyl)propane-1,3-diamine (2h)**
1.16 g (5.20 mmol, 99%), orange oil. ^{1}H (400 MHz, $CDCl_3$) δ 8.08 (br, 1H), 7.93 (s, 1H), 6.67 (s, 1H), 3.40 (quartet, *J*= 6.8 Hz, 2H), 2.91 (t, *J*= 6.8 Hz, 2H), 2.28 (s, 3H), 2.19 (s, 3H), 1.89 (pentet, *J*= 6.8 Hz, 2H); ^{13}C NMR (125 MHz, $CDCl_3$) δ 147.4, 144.3, 130.3, 126.5, 124.4, 114.2, 41.0, 39.9, 32.7, 20.9, 18.7; ESI-HRMS: Calcd for $C_{11}H_{18}N_3O_2^+$ $[M+H]^+$: 224.1394; found: 224.1394.

***N*-(Aminoethyl)-1,2-diaminobenzene analogs (3a-h) general procedure**
Concentrated HCl (17 mL) and Pd/C (10% wt., 698 mg) were added to a solution of **2a** (1.01 g, 5.5 mmol) in MeOH (100 mL). The reaction mixture was purged with H_2 then stirred at r.t. under an atmosphere of H_2 for 24 h. The suspension was filtered and the filtrate concentrated under reduced pressure to give **3a** which was used without further purification.

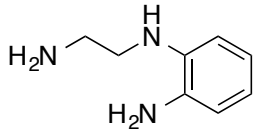

***N*^{1}-(2-Aminoethyl)benzene-1,2-diamine hydrochloride (3a)**
Crude, pink solid. ^{1}H (400 MHz, MeOD-d_4) δ 7.35 (t, *J*= 6.8 Hz, 1H), 7.30 (d, *J*= 7.6 Hz, 1H), 7.00 (d, *J*= 7.6 Hz, 1H), 6.87 (t, *J*= 7.2 Hz, 1H), 3.57 (br, 2H), 3.24 (br, 2H); ^{13}C NMR (125 MHz, MeOD-d_4) δ 142.2, 131.3, 125.1, 119.9, 119.5, 114.8, 41.7, 39.6; ESI-HRMS: Calcd for $C_8H_{14}N_3^+$ $[M+H]^+$: 152.1188; found: 152.1184.

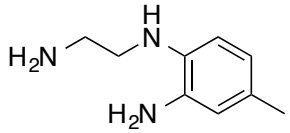

***N*^{1}-(2-Aminoethyl)-4-methylbenzene-1,2-diamine hydrochloride (3b)**
Crude, light brown solid. ^{1}H (400 MHz, MeOD-d_4) δ 7.18 (m, 2H), 6.94 (d, J= 5.2, 1H), 3.54 (br, 2H), 3.24 (br, 2H), 2.26 (s, 3H); ^{13}C NMR (125 MHz, MeOD-d_4) δ 139.2, 131.5, 130.6, 125.4, 120.2, 115.8, 42.1, 40.0, 20.3; ESI-HRMS: Calcd for $C_9H_{16}N_3^+$ $[M+H]^+$: 166.1339; found: 166.1339.

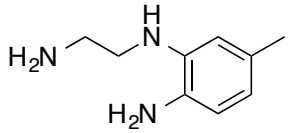

***N*^{1}-(2-Aminoethyl)-5-methylbenzene-1,2-diamine hydrochloride (3c)**
Crude, light brown solid. ^{1}H (400 MHz, MeOD-d_4) δ 7.23 (d, J= 7.6 Hz, 1H), 6.85 (s, 1H), 6.67 (d, J= 7.6 Hz, 1H), 3.57 (br, 2H), 3.25 (br, 2H), 2.32 (s, 3H); ^{13}C

NMR (125 MHz, MeOD-d_4) δ 141.6, 141.5, 124.8, 120.7, 117.1, 115.6, 41.7, 39.6, 21.5; ESI-HRMS: Calcd for $C_9H_{16}N_3^+$ $[M+H]^+$: 166.1339; found: 166.1338.

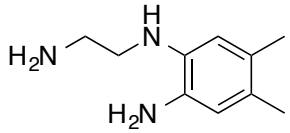

***N*^{1}-(2-Aminoethyl)-4,5-dimethylbenzene-1,2-diamine hydrochloride (3d)**

Crude, light brown solid. ^{1}H (400 MHz, MeOD-d_4) δ 7.05 (s, 1H), 6.83 (s, 1H), 3.52 (t, J= 5.6 Hz, 2H), 3.22 (t, J= 5.6 Hz, 2H), 2.26 (s, 3H), 2.19 (s, 3H); ^{13}C NMR (125 MHz, MeOD-d_4) δ 139.8, 132.0, 128.9, 125.7, 121.2, 116.7, 42.1, 39.7, 19.8, 18.7; ESI-HRMS: Calcd for $C_{10}H_{18}N_3^+$ $[M+H]^+$: 180.1495; found: 180.1495.

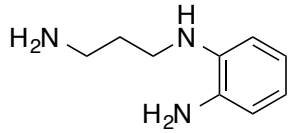

***N*^{1}-(3-aminopropyl)benzene-1,2-diamine hydrochloride (3e)**

Crude, pink solid. ^{1}H (400 MHz, MeOD-d_4) δ 6.60-6.10 (m, 4H), 2.59 (br, 2H), 2.35 (br,2H), 1.33 (br, 2H); ^{13}C NMR (125 MHz, MeOD-d_4) δ 139.6, 130.0, 124.4, 121.0, 120.8, 116.2, 42.9, 38.6, 27.0; ESI-HRMS: Calcd for $C_9H_{16}N_3^+$ $[M+H]^+$: 166.1339; found: 166.1339.

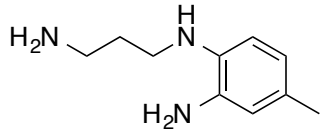

***N*^{1}-(3-aminopropyl)-4-methylbenzene-1,2-diamine hydrochloride (3f)**

Crude, light brown solid. ^{1}H (400 MHz, MeOD-d_4) δ 6.86-6.67 (m, 3H), 2.99 (br, 2H), 2.62 (br, 2H), 1.81 (s, 3H), 1.70 (br, 2H); ^{13}C NMR (125 MHz, MeOD-d_4) δ 137.9, 131.9, 130.8, 126.0, 124.9, 122.0, 47.2, 38.4, 26.2, 20.7; ESI-HRMS: Calcd for $C_{10}H_{18}N_3^+$ $[M+H]^+$: 180.1495; found: 180.1494.

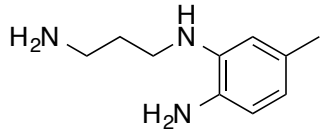

***N*^{1}-(3-aminopropyl)-5-methylbenzene-1,2-diamine hydrochloride (3g)**

Crude, light brown solid. ^{1}H (400 MHz, MeOD-d_4) δ 6.79 (d, J= 7.6 Hz 1H), 6.62 (s, 1H), 6.46 (d, J= 8.0 Hz, 1H), 2.98 (t, J= 6.8 Hz, 2H), 2.66 (t, J= 7.6 Hz, 2H), 1.87 (s, 3H), 1.70 (pentet, J= 6.8 Hz, 2H); ^{13}C NMR (125 MHz, MeOD-d_4) δ 142.0, 137.7, 125.6, 125.0, 119.8, 119.3, 45.3, 38.5, 26.8, 21.2; ESI-HRMS: Calcd for $C_{10}H_{18}N_3^+$ $[M+H]^+$: 180.1495; found: 180.1495.

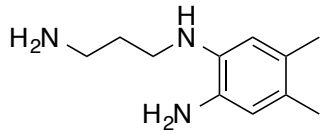

***N*^{1}-(3-aminopropyl)-4,5-dimethylbenzene-1,2-diamine hydrochloride (3h)**

Crude, light brown solid. ^{1}H NMR (400 MHz, MeOD-d_4) δ 8.07 (br s, 1H), 7.35 (s, 1H), 7.30 (s, 1H), 3.58 (t, J = 7.2 Hz, 2H), 3.17 (t, J = 7.2 Hz, 2H), 2.35-2.21 (m, 8H); ^{13}C NMR (125 MHz, MeOD-d_4) δ 140.51, 137.74, 131.46, 127.01, 124.00, 121.69, 48.13, 38.22, 26.01, 19.56, 19.20; ESI-HRMS: Calcd for $C_{11}H_{20}N_3^+$ $[M+H]^+$: 194.1652; found: 194.1652.

10-(2'-Aminoethyl)-flavin analogs (4a-h) general procedure

Alloxan monohydrate (643 mg, 4.02 mmol, 1.24 eq) was added to a solution of **3a** (606 mg, 3.23 mmol, 1.00 eq) in EtOH (20 mL) and aqueous HCl (1 M, 8.0 mL). The reaction mixture was stirred at 90 °C for 1 h until a yellow precipitate formed. The resulting solid was isolated by vacuum filtration to give **4a**.

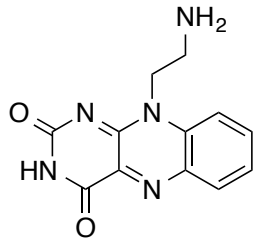

10-(2-Aminoethyl)benzo[*g*]pteridine-2,4(3*H*,10*H*)-dione hydrochloride (4a)

228 mg (0.78 mmol, 24%), yellow solid. ^{1}H (400 MHz, D_2O) δ 8.17 (d, J= 5.5 Hz, 1H), 8.09 (t, J= 5.3 Hz, 1H), 7.94 (d, J=5.8 Hz, 1H), 7.78 (t, J= 5.1 Hz, 1H), 5.11 (t, J= 4.2 Hz, 2H), 3.58 (t, J= 4.2 Hz, 2H); ^{13}C NMR (125 MHz, D_2O) δ 161.4, 158.2, 151.4, 137.6, 136.8, 136.0, 132.4, 128.2, 115.8, 100.0, 42.6, 37.2; ESI-HRMS: Calcd for $C_{12}H_{12}N_5O_2^+$ $[M+H]^+$: 258.0986; found: 258.0985.

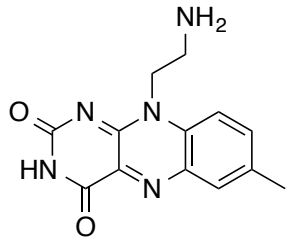

10-(2-Aminoethyl)-7-methylbenzo[*g*]pteridine-2,4(3*H*,10*H*)-dione hydrochloride (4b)

608 mg (1.98 mmol, 33%), yellow solid. ^{1}H (400 MHz, D_2O) δ 7.96 (d, J= 8.4 Hz, 1H), 7.93 (s, 1H), 7.84 (d, J= 8.8 Hz, 1H) 5.09 (t, J= 6.4 Hz, 2H), 3.58 (t, J= 6.8 Hz, 2H), 2.53 (s, 3H); ^{13}C NMR (101 MHz, D_2O) δ 161.27, 158.07, 156.67, 150.79, 139.54, 136.31, 136.01, 131.18, 130.38, 115.46, 42.58, 37.12, 19.93; ESI-HRMS: Calcd for $C_{13}H_{14}N_5O_2^+$ $[M+H]^+$: 272.1142; found: 272.1140.

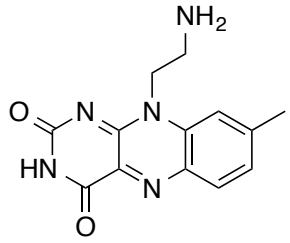

10-(2-Aminoethyl)-8-methylbenzo[*g*]pteridine-2,4(3*H*,10*H*)-dione hydrochloride (4c)

265 mg (0.86 mmol, 17%), yellow solid. ^{1}H (400 MHz, D_2O) δ 7.98 (d, J= 8.4 Hz, 1H), 7.75 (s, 1H), 7.62 (d, J= 8.4 Hz, 1H), 5.06 (t, J= 6.4 Hz, 2H), 3.56 (t, J= 6.4 Hz, 2H), 2.62 (s, 3H); ^{13}C NMR (125 MHz, MeOD-d_4) δ 161.3, 158.1, 151.5, 151.1 134.9, 134.4, 132.4, 131.8, 130.8, 115.4, 42.4, 37.0, 22.2; ESI-HRMS: Calcd for $C_{13}H_{14}N_5O_2^+$ $[M+H]^+$: 272.1142; found: 272.1140.

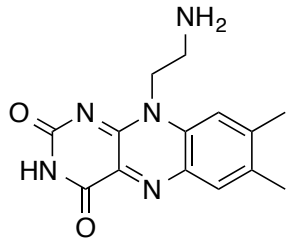

10-(2-Aminoethyl)-7,8-dimethylbenzo[*g*]pteridine-2,4(3*H*,10*H*)-dione hydrochloride (4d)

283 mg(0.88 mmol, 18%), yellow solid. ^{1}H (400 MHz, D_2O) δ 7.66 (s, 2H), 4.98 (s, 2H), 3.52 (s, 2H), 2.52 (s, 3H), 2.37 (s, 3H); ^{13}C NMR (125 MHz, D_2O) δ 160.8, 157.7, 150.2, 139.8, 135.9, 134.1, 130.9, 130.5, 115.6, 100.2, 42.3, 36.9, 20.7, 18.6; ESI-HRMS: Calcd for $C_{14}H_{16}N_5O_2^+$ $[M+H]^+$: 286.1299; found: 286.1298.

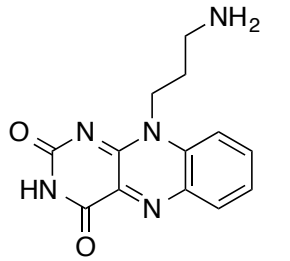

10-(3-aminopropyl)benzo[*g*]pteridine-2,4(3*H*,10*H*)-dione hydrochloride (4e)

499 mg (1.62 mmol, 37%), yellow solid. ^{1}H (400 MHz, D_2O) δ 8.08-8.01 (m, 2H), 7.95 (d, J= 8.4 Hz, 1H), 7.73 (t, J= 7.6 Hz, 1H), 3.16 (t, J= 6.8 Hz, 2H), 2.30 (pentet, J= 7.2 Hz, 2H); ^{13}C NMR (125 MHz, D_2O) δ 161.1, 158.0, 150.4, 137.6, 136.4, 135.7, 132.5, 131.8, 128.4, 116.4, 42.6, 36.4, 25.1; ESI-HRMS: Calcd for $C_{13}H_{14}N_5O_2^+$ $[M+H]^+$: 272.1142; found: 272.114.

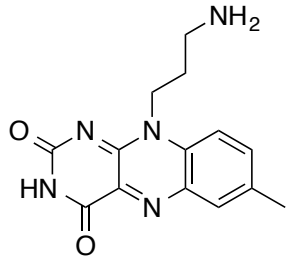

10-(3-aminopropyl)-7-methylbenzo[*g*]pteridine-2,4(3*H*,10*H*)-dione hydrochloride (4f)

802 mg (2.49 mmol, 36%), yellow solid. ^{1}H NMR (400 MHz, MeOD-d_4) δ 8.06 (s, 1H), 7.97 ? 7.87 (m, 2H), 4.84 (t, J = 6.8 Hz, 2H), 3.12 (t, J = 6.7 Hz, 2H), 2.57 (s, 3H), 2.31 (p, J = 6.6 Hz, 2H). ^{13}C NMR (101 MHz, MeOD-d_4) δ 161.86, 158.74, 152.16, 139.26, 139.07, 139.00, 137.54, 132.80, 131.93, 116.93, 43.24, 37.64, 26.64, 20.73. ESI-HRMS: Calcd for $C_{14}H_{16}N_5O_2^+$ $[M+H]^+$: 286.1299; found: 286.1297.

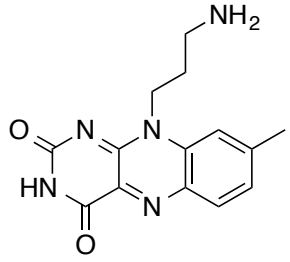

10-(3-aminopropyl)-8-methylbenzo[*g*]pteridine-2,4(3*H*,10*H*)-dione hydrochloride (4g)

945 mg (2.94, 40%), yellow solid. ^{1}H NMR (400 MHz, MeOD-d_4) δ 8.13 (d, J = 8.4 Hz, 1H), 7.86 (s, 1H), 7.61 (dd, J = 8.3, 1.5 Hz, 1H), 4.84 (t, J = 6.8 Hz, 2H), 3.13 (t, J = 6.7 Hz, 2H), 2.69 (s, 3H), 2.31 (p, J = 6.8 Hz, 2H). ^{13}C NMR (101 MHz, MeOD d_4) δ 162.00, 158.81, 152.50, 150.29, 137.90, 136.05, 133.99, 133.40, 130.14, 116.74, 43.10, 37.66, 26.55, 22.74. ESI-HRMS: Calcd for $C_{14}H_{16}N_5O_2^+$ $[M+H]^+$: 286.1299; found: 286.1298.

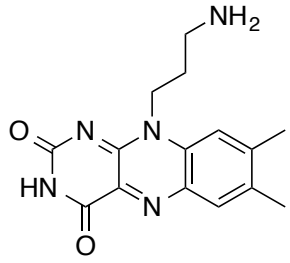

10-(3-aminopropyl)-7,8-dimethylbenzo[*g*]pteridine-2,4(3*H*,10*H*)-dione hydrochloride (4h)

122 mg (0.38 mmol, 14%), yellow solid. ^{1}H (400 MHz, D_2O) δ 7.61 (s, 1H), 7.58 (s, 1H), 4.68 (br, 2H), 3.15 (br, 2H), 2.51 (br, 2H), 2.36 (s, 3H), 2.26 (s, 3H); ^{13}C NMR (101 MHz, D_2O) δ 161.01, 157.77, 151.15, 149.56, 139.59, 134.58, 134.02, 130.66, 130.62, 115.84, 42.54, 36.40, 24.73, 20.67, 18.61; ESI-HRMS: Calcd for $C_{15}H_{18}N_5O_2^+$ $[M+H]^+$: 300.1455; found: 300.1454.

***N*-(10-(2'-Aminoethyl)-flavin)acrylamide analogs (5a-h) general procedure**

Acryloyl chloride (55 µL, 0.68 mmol, 2.0 eq) was added to a solution of **4a** (100 mg, 0.34 mmol, 1.0 eq) in aqueous NaOH (1 mL, 1 M, 3.0 eq) at 0 °C wrapped in foil to protect from ambient light. The reaction mixture was allowed to warm to r.t. slowly and stirred overnight. The resulting yellow precipitate was isolated by vacuum filtration and purified by silica gel chromatography (95:5 to 80:20 CH_3CN:MeOH) to give **5a**.

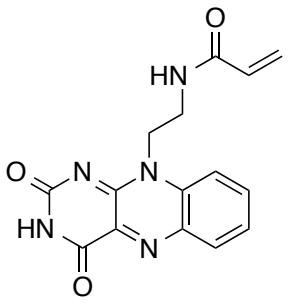

***N*-(2-(2,4-dioxo-3,4-dihydrobenzo[*g*]pteridin-10(2*H*)-yl)ethyl)acrylamide (5a)**

69 mg (0.20 mmol, 59%) yellow solid. ^{1}H NMR (400 MHz, DMSO-d_6) δ 11.45 (s, 1H), 8.47 (t, J = 5.9 Hz, 1H), 8.14 (dd, J = 8.2, 1.5 Hz, 1H), 8.08 (d, J = 8.6 Hz, 1H), 7.95 (ddd, J = 8.7, 7.1, 1.6 Hz, 1H), 7.64 (ddd, J = 8.1, 7.1, 1.1 Hz, 1H), 6.14-6.00 (m, 2H), 5.58 (dd, J = 8.3, 4.0 Hz, 1H), 4.68 (t, J = 6.9 Hz, 2H), 3.54 (q, J = 6.6 Hz, 2H); ^{13}C NMR (101 MHz, DMSO) δ 165.56, 159.69, 155.57, 150.68, 138.51, 134.94, 134.87, 132.86, 131.79, 131.19, 126.02, 125.66, 116.14, 43.15, 35.37; ESI-HRMS: Calcd for $C_{15}H_{13}N_5O_3Na^+$ $[M+Na]^+$: 334.0911; found: 334.0910.

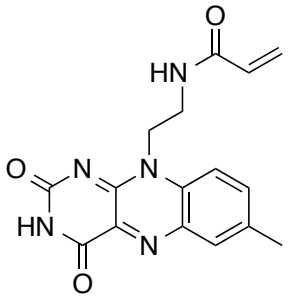

***N*-(2-(7-methyl-2,4-dioxo-3,4-dihydrobenzo[*g*]pteridin-10(2*H*)-yl)ethyl)acrylamide (5b)**

31 mg (0.10 mmol, 31%), yellow solid. ^{1}H NMR (400 MHz, DMSO-d_6) δ 11.40 (s, 1H), 8.53 (t, J = 6.0 Hz, 1H), 7.97 (d, J = 8.9 Hz, 1H), 7.93-7.86 (m, 1H), 7.77 (dd, J = 8.8, 2.1 Hz, 1H), 6.15-6.00 (m, 2H), 5.57 (dd, J = 8.9, 3.3 Hz, 1H), 4.65 (t, J = 6.9 Hz, 2H), 3.53 (q, J = 6.5 Hz, 2H), 2.47 (s, 3H); ^{13}C NMR (101 MHz, DMSO) δ 165.54, 159.73, 155.53, 150.31, 138.22, 136.53, 135.98, 134.95, 131.23, 130.87, 130.84, 125.62, 115.93, 43.27, 35.43, 20.17; ESI-HRMS: Calcd for $C_{16}H_{16}N_5O_3^+$ $[M+H]^+$: 326.1248; found: 326.1252.

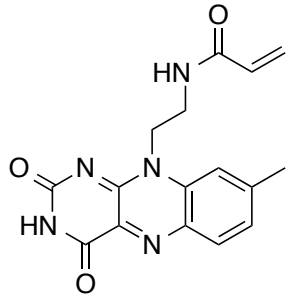

***N*-(2-(8-methyl-2,4-dioxo-3,4-dihydrobenzo[*g*]pteridin-10(2*H*)-yl)ethyl)acrylamide (5c)**

32 mg (0.10 mg, 15%), yellow solid. ^{1}H NMR (400 MHz, DMSO-d_6) δ 11.40 (s, 1H), 8.38 (t, J = 6.0 Hz, 1H), 7.99 (d, J = 8.3 Hz, 1H), 7.85 (s, 1H), 7.47 (d, J = 8.4 Hz, 1H), 6.04 (d, J = 6.1 Hz, 2H), 5.58 (q, J = 8.6, 6.2 Hz, 1H), 4.66 (t, J = 6.6 Hz, 2H), 3.55 (q, J = 6.6 Hz, 2H), 2.54 (s, 3H); ^{13}C NMR (101 MHz, DMSO) δ 165.62, 159.80, 155.56, 150.61, 146.55, 137.13, 133.41, 132.90, 131.47, 131.16, 127.67, 125.63, 115.88, 43.15, 35.50, 22.21; (ESI-HRMS: Calcd for $C_{16}H_{15}N_5O_3Na^+$ $[M+Na]^+$: 348.1065; found: 348.1067.

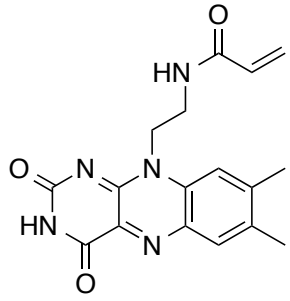

***N*-(2-(7,8-dimethyl-2,4-dioxo-3,4-dihydrobenzo[*g*]pteridin-10(2*H*)-yl)ethyl)acrylamide (5d)**

58 mg (0.17 mmol, 49%), yellow solid. ^{1}H NMR (400 MHz, DMSO-d_6) δ 11.36 (s, 1H), 8.56 (t, J = 6.0 Hz, 1H), 7.90 (s, 1H), 7.87 (s, 1H), 6.13-5.99 (m, 2H), 5.57 (dd, J = 8.0, 4.3 Hz, 1H), 4.66 (t, J = 6.8 Hz, 2H), 3.54 (q, J = 6.6 Hz, 2H), 2.47 (s, 3H), 2.38 (s, 3H); ^{13}C NMR (101 MHz, DMSO) δ 165.59, 159.86, 155.50, 150.21, 146.48, 136.87, 135.80, 133.78, 131.25, 131.19, 130.91, 125.54, 116.24, 43.30, 40.15, 39.94, 39.73, 39.52, 39.31, 39.10, 38.89, 35.55, 20.74, 18.77; ESI-HRMS: Calcd for $C_{17}H_{18}N_5O_3Na^+$ $[M+Na]^+$: 362.1229; found: 362.1221.

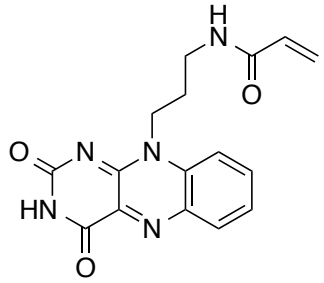

***N*-(3-(2,4-dioxo-3,4-dihydrobenzo[*g*]pteridin-10(2*H*)-yl)propyl)acrylamide (5e)**

48 mg (0.13 mmol, 41%), yellow solid. ^{1}H NMR (400 MHz, DMSO-d_6) δ 11.43 (s, 1H), 8.39 (t, J = 5.7 Hz, 1H), 8.13 (d, J = 8.1 Hz, 1H), 7.95 (dt, J = 15.6, 8.5 Hz, 2H), 7.65 (t, J = 7.5 Hz, 1H), 6.27 (dd, J = 17.1, 10.2 Hz, 1H), 6.09 (dd, J = 17.0, 2.2 Hz, 1H), 5.59 (dd, J = 10.1, 2.2 Hz, 1H), 4.63 (t, J = 7.7 Hz, 2H), 3.31 (q, J = 6.5 Hz, 2H), 1.94 (p, J = 7.0 Hz, 2H); ^{13}C NMR (101 MHz, DMSO) δ 164.68, 159.78, 155.70, 150.56, 138.73, 134.95, 134.91, 132.33, 131.87, 131.80, 126.03, 125.05, 116.22, 42.42, 36.02, 26.67; ESI-HRMS: Calcd for $C_{16}H_{15}N_5O_3Na^+$ $[M+H]^+$: 348.1067; found: 348.1066.

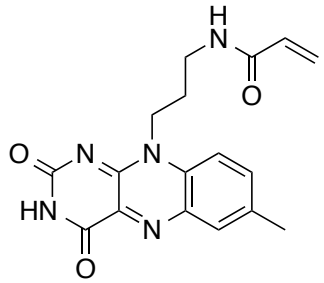

***N*-(3-(7-methyl-2,4-dioxo-3,4-dihydrobenzo[*g*]pteridin-10(2*H*)-yl)propyl)acrylamide (5f)**

88 mg (0.27 mmol, 87%), yellow solid. ^{1}H NMR (400 MHz, DMSO-d_6) δ 11.38 (s, 1H), 8.38 (t, J = 5.7 Hz, 1H), 7.99-7.82 (m, 2H), 7.76 (d, J = 8.9 Hz, 2H), 6.27 (dd, J = 17.1, 10.1 Hz, 1H), 6.17-6.00 (m, 1H), 5.64-5.53 (m, 1H), 4.61 (t, J = 7.6 Hz, 2H), 1.92 (p, J = 7.1 Hz, 2H), 3.30 (q, J = 6.6 Hz, 2H), 2.48 (s, 3H); ^{13}C NMR (101 MHz, DMSO) δ 164.70, 159.84, 155.67, 150.21, 136.54, 136.01, 135.01, 131.80, 130.98, 130.32, 125.08, 115.98, 48.61, 42.47, 40.15, 39.94, 39.73, 39.52, 39.31, 39.10, 38.90, 36.02, 26.75, 20.19; ESI-HRMS: Calcd for $C_{17}H_{18}N_5O_3Na^+$ $[M+Na]^+$: 362.1229; found: 362.1224.

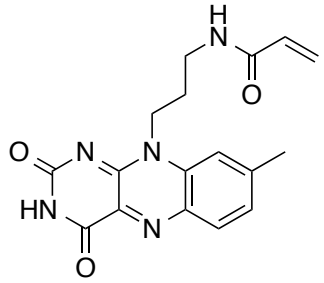

***N*-(3-(8-methyl-2,4-dioxo-3,4-dihydrobenzo[*g*]pteridin-10(2*H*)-yl)propyl)acrylamide (5g)**

24 mg (0.071 mmol, 23%), yellow solid. ^{1}H NMR (400 MHz, DMSO-d_6) δ 11.37 (s, 1H), 8.41 (s, 1H), 8.00 (d, J = 8.2 Hz, 1H), 7.76 (s, 1H), 7.48 (d, J = 8.3 Hz, 1H), 6.28 (dd, J = 17.1, 9.9 Hz, 1H), 6.10 (d, J = 17.2 Hz, 1H), 5.60 (d, J = 10.1 Hz, 1H), 4.61 (s, 2H), 3.35-3.21 (m, 2H), 2.57 (s, 3H), 2.07-1.81 (m, 2H); ^{13}C NMR (101 MHz, DMSO) δ 164.70, 159.91, 155.71, 150.53, 146.74, 137.38, 133.47, 132.33, 131.81, 131.58, 127.72, 125.10, 115.65, 42.30, 35.98, 26.62, 22.13; ESI-HRMS: Calcd for $C_{17}H_{18}N_5O_3Na^+$ $[M+Na]^+$: 362.1229; found: 362.1223.

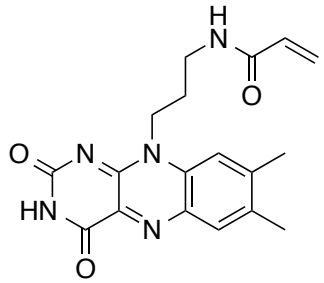

***N*-(3-(7,8-dimethyl-2,4-dioxo-3,4-dihydrobenzo[*g*]pteridin-10(2*H*)-yl)propyl)acrylamide (5h)**

22 mg (0.056 mmol, 37%), yellow solid. ^{1}H NMR (400 MHz, DMSO-d_6) δ 11.33 (s, 1H), 8.41 (t, J = 5.7 Hz, 1H), 7.87 (s, 1H), 7.75 (s, 1H), 6.29 (dd, J = 17.1, 10.2 Hz, 1H), 6.10 (dd, J = 17.1, 2.2 Hz, 1H), 5.60 (dd, J = 10.1, 2.2 Hz, 1H), 4.60 (t, J = 7.6 Hz, 2H), 3.30 (q, J = 6.5 Hz, 2H), 2.48 (s, 3H), 2.38 (s, 3H), 1.93 (p, J = 7.0 Hz, 2H); ^{13}C NMR (101 MHz, DMSO) δ 164.68, 159.96, 155.66, 150.15, 146.59, 137.15, 135.81, 133.80, 131.81, 131.05, 130.62, 125.08, 115.91, 42.33, 35.96, 26.69, 20.63, 18.78; ESI-HRMS: Calcd for $C_{18}H_{19}N_5O_3Na^+$ $[M+Na]^+$: 376.1380; found: 376.1379.

Plasmid Preparation

The N-terminal domain of Riboflavin synthase (*Escherichia coli*, strain K12, gene: ribC, accession no. P0AFU8 of the Universal Protein Resource UniProt, residue 1-97) was synthesized by Genewiz, Inc. with Nde1 and Xho1 restriction sites at the 5′ and 3′ ends and was subcloned into our pSKB3 vector that is based on Novagen's pET-28a vector, and where the thrombin site is replaced by a tobacco

etch virus (TEV) cleavage site. The gene insert is shown below in (A). All sequences were verified by primer-guided sequencing.

(A) Sequence synthesized by Genewiz with N-terminal Riboflavin synthase sequence (1-97) highlighted in green and Nde1/Xho1 sites underlined:
ATAATACATATGTTTACGGGGATTGTACAGGGCACCGCAAAACTGGTGTCG
ATTGACGAGAAACCAAATTTTCGTACGCATGTGGTGGAGTTACCCGACCAC
ATGCTGGACGGCCTGGAAACCGGTGCTTCCGTGGCGCATAACGGTTGCTG
CCTGACCGTGACGGAAATTAACGGCAACCATGTCAGTTTTGACCTGATGAA
AGAAACGTTACGCATTACCAATCTTGGCGATTTAAAAGTGGGGGATTGGGTA
AACGTTGAGCGTGCGGCGAAATTCAGTGATGAAATTGGCGGACACTGACTC
GAGATAATA

Mutations N72D and N83A were introduced to the N-terminal Riboflavin synthase construct by two consecutive site-directed mutagenesis steps using the KAPA HiFi HotStart ReadyMix PCR Kit (KAPA BioSystems). Mutation N72D: forward primer: 5′- GAA ACG TTA CGC ATT ACC GAT CTT GGC GAT TTA AAA GTG-3′, and its reverse complementary primer; Mutation N83A: 5′-GTG GGG GAT TGG GTA GCC GTT GAG CGT GCG GCG-3′ and reverse primer: 5′-CGC CGC ACG CTC AAC GGC TAC CCA ATC CCC CAC-3′). The final gene insert is shown below in (B).

(B) N72D/N83A mutations of N-terminal Riboflavin synthase sequence are highlighted in red:
ATGTTTACGGGGATTGTACAGGGCACCGCAAAACTGGTGTCGATTGACGAG
AAACCAAATTTTCGTACGCATGTGGTGGAGTTACCCGACCACATGCTGGAC
GGCCTGGAAACCGGTGCTTCCGTGGCGCATAACGGTTGCTGCCTGACCGT
GACGGAAATTAACGGCAACCATGTCAGTTTTGACCTGATGAAAGAAACGTTA
CGCATTACCGATCTTGGCGATTTAAAAGTGGGGGATTGGGTAGCCGTTGAG
CGTGCGGCGAAATTCAGTGATGAAATTGGCGGACACTGA

Mutations M64F and T67C were introduced to the above sequence by two consecutive site-directed mutagenesis steps using the KAPA HiFi HotStart ReadyMix PCR Kit (KAPA BioSystems) to create RS-B. Mutation M64F: forward primer: 5′-CAT GTC AGT TTT GAC CTG TTC AAA GAA ACG TTA CGC ATT-3′, and its reverse complementary primer; Mutation T67C: 5′-GTT TTG ACC TGT TCA AAG AAT GCT TAC GCA TTA CCG ATC TTG-3′, and its reverse complementary primer. The final gene insert is shown below in (C).

(C) RS-B (M64F/T67C mutation highlighted in red):
ATGTTTACGGGGATTGTACAGGGCACCGCAAAACTGGTGTCGATTGACGAG
AAACCAAATTTTCGTACGCATGTGGTGGAGTTACCCGACCACATGCTGGAC
GGCCTGGAAACCGGTGCTTCCGTGGCGCATAACGGTTGCTGCCTGACCGT
GACGGAAATTAACGGCAACCATGTCAGTTTTGACCTGTTCAAAGAATGCTTA
CGCATTACCGATCTTGGCGATTTAAAAGTGGGGGATTGGGTAGCCGTTGAG
CGTGCGGCGAAATTCAGTGATGAAATTGGCGGACACTGA

Mutations S41F was introduced to RS-B by site-directed mutagenesis using the KAPA HiFi HotStart ReadyMix PCR Kit (KAPA BioSystems) to create RS-A. Mutation S41F was introduced with following two 5'-phosphorylated primers. Forward primer: 5′-GGA CGG CCT GGA AAC CGG TGC T-3′; Reverse primer: 5′- P-TTT GTG GCG CAT AAC GGT TGC TGC -3. The final gene insert is shown below in (D).

(D) RS-A (S41F mutation highlighted in red):
ATGTTTACGGGGATTGTACAGGGCACCGCAAAACTGGTGTCGATTGACGAG
AAACCAAATTTTCGTACGCATGTGGTGGAGTTACCCGACCACATGCTGGAC
GGCCTGGAAACCGGTGCTTTTGTGGCGCATAACGGTTGCTGCCTGACCGTG
ACGGAAATTAACGGCAACCATGTCAGTTTTGACCTGTTCAAAGAATGCTTAC
GCATTACCGATCTTGGCGATTTAAAAGTGGGGGATTGGGTAGCCGTTGAGC
GTGCGGCGAAATTCAGTGATGAAATTGGCGGACACTGA

Protein Expression and Purification

Plasmids were transformed into *E. coli* BL21 (DE3). Starter cultures (lysogeny broth, 50 mg/L kanamycin) were inoculated from single colonies, grown at 37 °C and used for 1:50 inoculation of 1-L cultures (terrific broth, 50 mg/L kanamycin). Cultures were grown to an OD of around 0.5, cooled for 20 min at 16 °C, induced with 0.5 mM isopropyl-β-d-thiogalactopyranoside, and grown overnight at 16 °C. Cells were harvested by centrifugation for 15 min at 4,000 × *g* at 4 °C and either washed with PBS and stored as a pellet at −80 °C or directly resuspended in 20 mL of lysis buffer [20 mM Hepes (pH 7.9); 300 mM NaCl; 10 mM imidazole; half of a tablet of Pierce Protease Inhibitor Tablet, EDTA-free (ThermoScientific); 1 mM PMSF; 2 mg of lysozyme]. After incubation for 20 min at 4 °C, the cells were lysed with an Avestin C3 homogenizer, followed by 20 min of centrifugation at 24,000 × *g*. The supernatant was filtered through a 40-μm Steriflip filter (Millipore), loaded onto a 5-mL Ni-NTA column (Protino; Machery Nagel), and washed with buffer A [20 mM Hepes (pH 7.9), 300 mM NaCl]. The column was washed with 30 mL of washing buffer [20 mM Hepes (pH 7.9), 300 mM NaCl, 25 mM imidazole] and eluted with elution buffer [20 mM Hepes (pH 7.9), 300 mM NaCl, 250 mM imidazole]. Imidazole was removed by exchanging against buffer A with a 10DG desalting column (BioRad), followed by overnight incubation at 4 °C with 1:50 molar equivalents of TEV protease to remove the N-terminal His-tag. The sample was incubated with 0.5 mL of Ni-NTA agarose for 2 h, and the cleaved protein was eluted with 10 mM imidazole containing buffer A. After concentrating the protein with a centrifugal spin concentrator (Millipore), a final size exclusion chromatography run (Superdex 75 10/300 GL; GE Healthcare) with an Akta purifier against buffer B [20 mM Hepes, 150 mM NaCl, (pH 7.9)] yielded proteins of typically >95% purity, as characterized by SDS/PAGE and electrospray ionization (ESI) MS to validate the mass of all proteins. MS measurements of proteins and cofactors were performed using a Thermo LTQ-

Orbitrap-XL mass spectrometer equipped with an ESI source. This instrument is located in the QB3/Chemistry Mass Spectrometry Facility at the University of California, Berkeley. Purified proteins were stored on ice for up to 1 day or frozen in liquid nitrogen in small aliquots and stored at −80 °C.

Bioconjugation Studies

100 μM of purified riboflavin protein was treated with a 1 mM solution of the probe in aqueous buffer (300 mM NaCl, 20 mM HEPES, pH=7.9, 5 mM TCEP) at 37 °C for 2 hours The product was filtered and purified by size exclusion chromatography (Superdex 75, 10/300 GL) on an Akta Purifier (GE Healthcare) to remove any free probe.

Absorbance and Fluorescence Studies

Absorbance spectra were measured using a Cary 100 Bio UV-vis spectrophotometer (Varian). Fluorescence excitation and emission spectra of free probes and RS-conjugates were measured using a QuantaMaster 400 spectrofluorometer (Photon Technology International) and obtained in aqueous buffer (150 mM NaCl, 20 mM HEPES, pH=7.9) at 25 °C.

Fluorescence anisotropy properties of purified riboflavin proteins and its conjugates were characterized by using an SLM-AB2 fluorometer (Aminco). The excitation anisotropy spectrum was recorded in buffer (150 mM NaCl, 20 mM HEPES, pH=7.9) at 20 °C. The emission wavelength was set at 520 nm, and the excitation was set at 470 nm. FA measurements were recorded on dilute and clarified protein solutions at 20 °C in buffer at the indicated excitation and emission wavelengths.

Bioconjugation of Riboflavin Synthase in Human Cell Lysate

Cell lysate was prepared from the human prostate cancer cell line, PC3. PC3 cells were grown to confluence in 10 cm plates, lifted via cell scraper and resuspended in 2 mL lysis buffer (20 mM HEPES, 150 mM NaCl, 1% Triton-X100, 1X protease inhibitor) and lysed via sonication with a Misonix Sonicator 3000 (6 x 5 s pulse, 10 s interval, 2.5 power). The suspension was centrifuged (16,000 rcf, 30 min, 4 °C) and the supernatant isolated and analyzed by BCA assay to determine total protein concentration.

For dose-dependent labeling of F2pro, 10 μM RS-A or RS-B (1 μg protein) was incubated with 0 – 100 μM F2pro and PC3 cell lysate (10 μg protein) in 20 mM HEPES, 150 mM NaCl buffer at 37 °C for 1 h protected from light. SDS loading buffer was added and samples incubated at 95 °C for 5 min followed by electrophoresis on a precast 4-12% gradient polyacrylamide gel (Bio-Rad). Fluorescence gel imaging was performed using a Typhoon Trio variable mode scanner (GE Healthcare Life Sciences) using 488 nm excitation filter and 526 nm

emission filter settings. Coomassie staining was used to visualize total protein loading.

For titration of RS, 0 – 10 μM RS-A or RS-B was incubated with 100 μM F2pro and PC3 cell lysate (10 μg protein) in 20 mM HEPES, 150 mM NaCl buffer at 37 °C for 1 h protected from light. SDS loading buffer was added and samples incubated at 95 °C for 5 min followed by electrophoresis and imaging as described previously.

Fluorescence Anisotropy Imaging

Images were recorded with a laser scanning confocal microscope (Zeiss LSM 710, inverse AxioObserver) with a plan-apochromat M27 with a magnification of 20× (N.A. = 0.8) at room temperature. An anisotropy map was created on a pixel-by-pixel basis according to:

r=(S1−G×S2)/(S1+2G×S2),

where S1 and S2 are the P- and S-polarized images, respectively, and G is the G-factor that is determined by referencing the image anisotropy of RS to its known anisotropy (r = 0.21) as measured on the SLM-AB2 fluorometer. The LSM710 confocal microscope is equipped with polarization accessories (Carl Zeiss MicroImaging GmbH). Anisotropy images were calculated in Igor Pro (version 6.35, Wavemetrics) using a customized procedure as described previously.[8]

Supplementary Figures

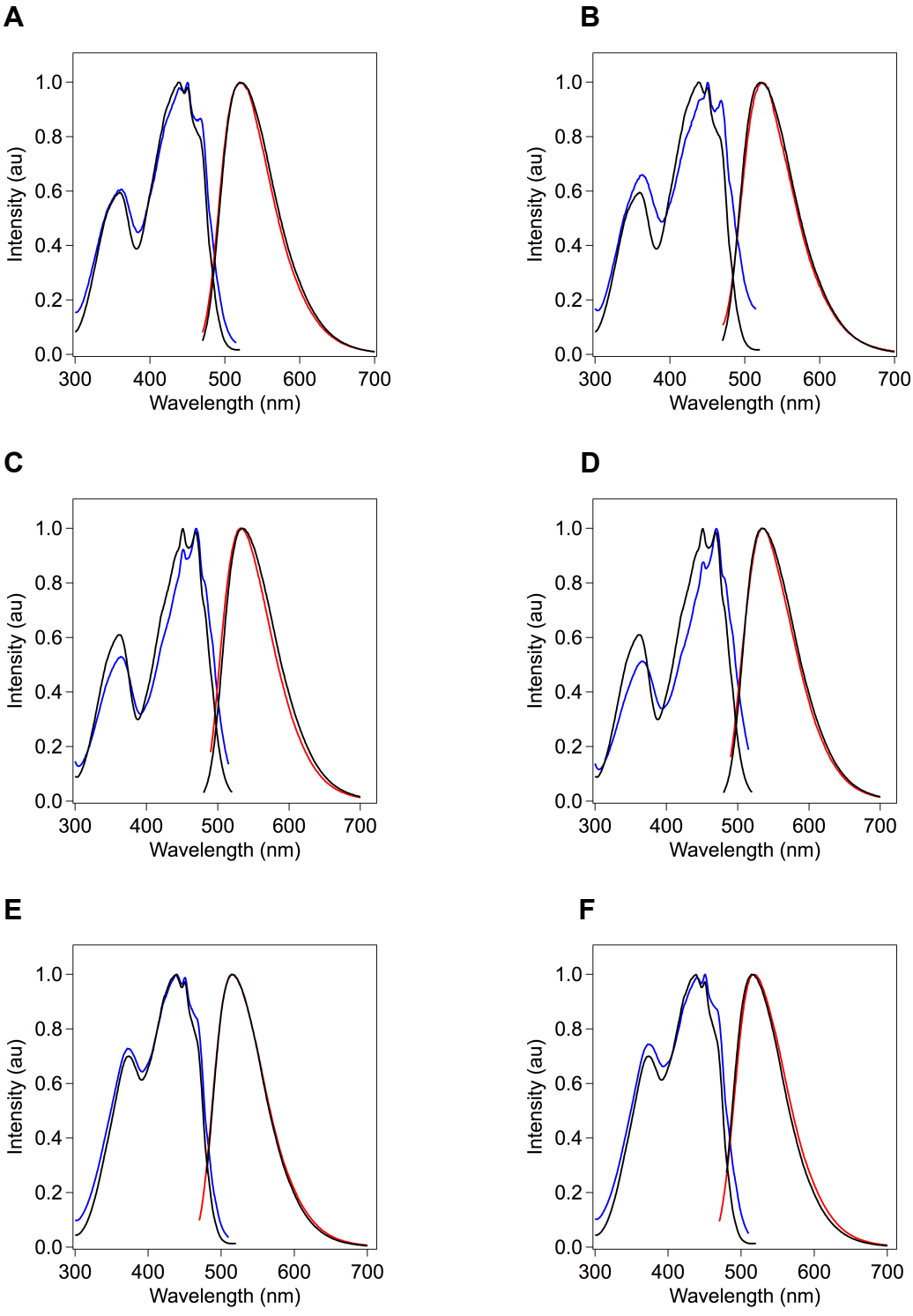

G

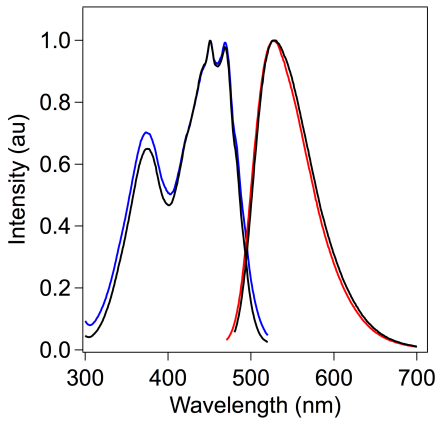
Intensity (au)
1.0
0.8
0.6
0.4
0.2
0.0
300
400
500
600
700
Wavelength (nm)

H

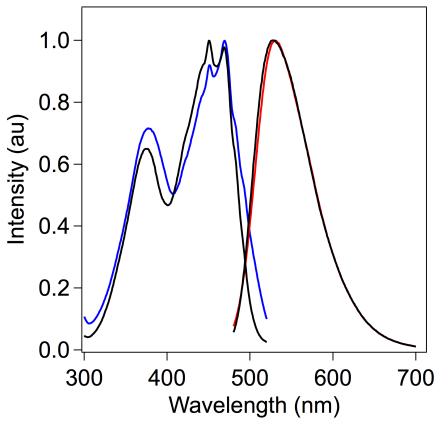
Intensity (au)
1.0
0.8
0.6
0.4
0.2
0.0
300
400
500
600
700
Wavelength (nm)

I

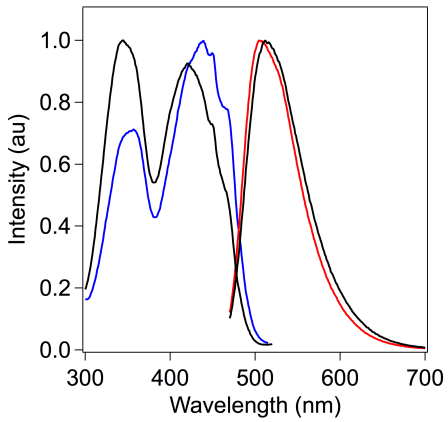
Intensity (au)
1.0
0.8
0.6
0.4
0.2
0.0
300
400
500
600
700
Wavelength (nm)

J

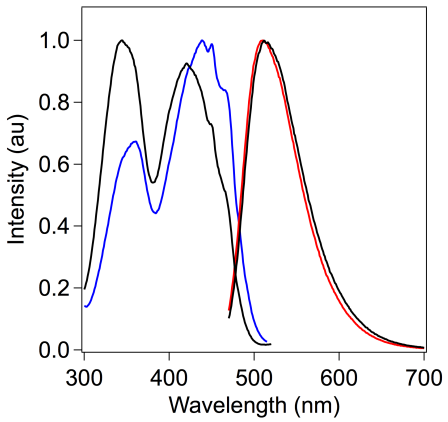
Intensity (au)
1.0
0.8
0.6
0.4
0.2
0.0
300
400
500
600
700
Wavelength (nm)

K

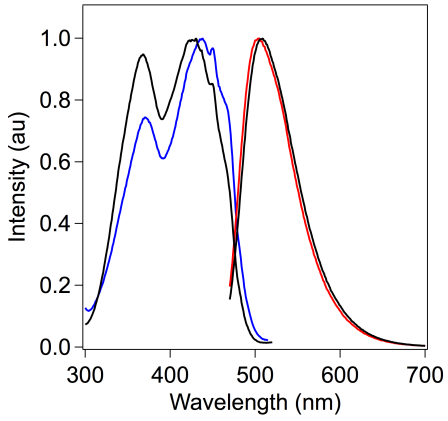
Intensity (au)
1.0
0.8
0.6
0.4
0.2
0.0
300
400
500
600
700
Wavelength (nm)

L

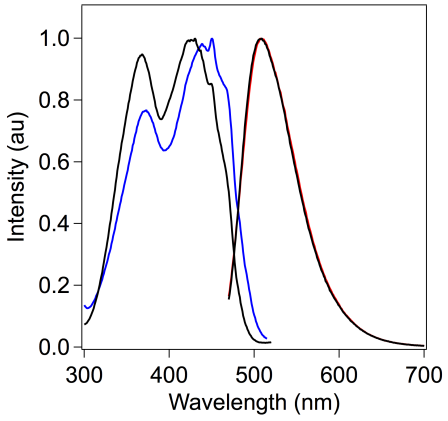
Intensity (au)
1.0
0.8
0.6
0.4
0.2
0.0
300
400
500
600
700
Wavelength (nm)

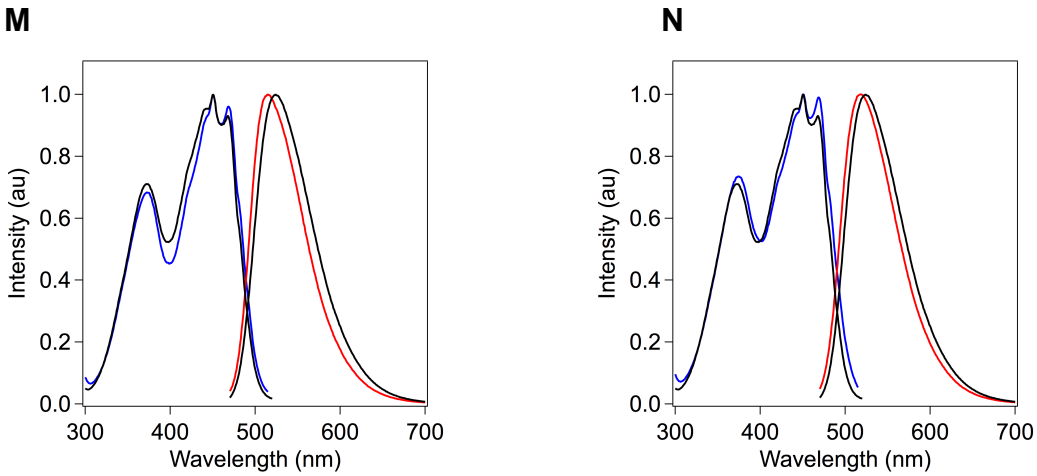

Figure S4.1. Fluorescence spectra of RS-flavin conjugates. Fluorescence excitation (blue) and emission spectra (red) of protein conjugate superimposed on excitation and emission spectra of free ligand (black) at 25 °C in aqueous buffer (150 mM NaCl, 20 mM HEPES, pH=7.9). (A) F1et, RS-A; (B) F1et, RS-B; (C) F2et, RS-A; (D) F2et, RS-B; (E) F3et, RS-A; (F) F3et, RS-B; (G) F4et, RS-A; (H) F4et, RS-B; (I) F1pro, RS-A; (J) F1pro, RS-B; (K) F3pro, RS-A; (L) F3pro, RS-B; (M) F4pro, RS-A; (N) F4pro, RS-B.

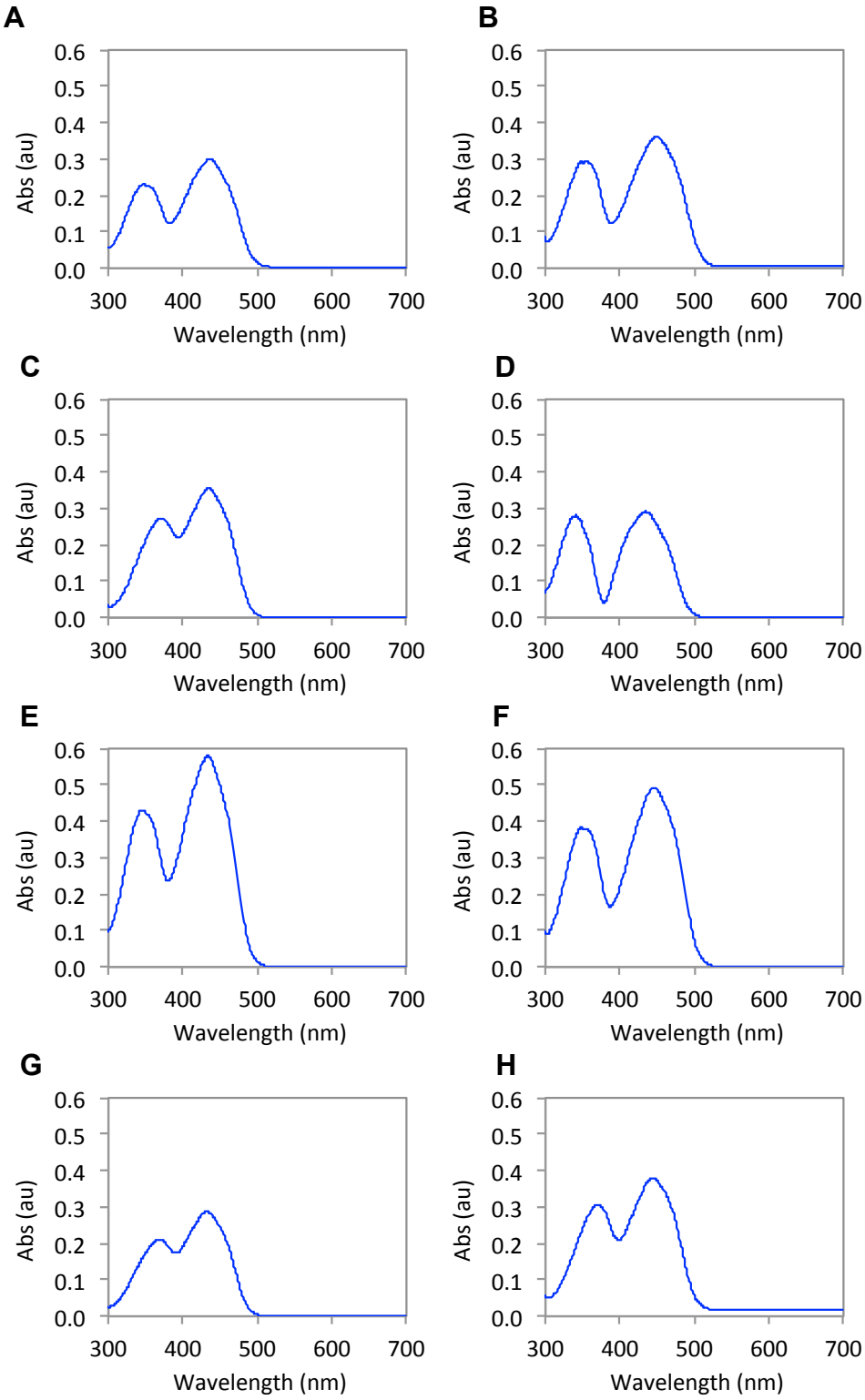

Figure S4.2. Absorption plots of free ligand. Data obtained at 25 °C in aqueous buffer (150 mM NaCl, 20 mM HEPES, pH=7.9). (A) F1et; (B) F2et; (C) F3et; (D) F4et; (E) F1pro; (F) F2pro; (G) F3pro; (H) F4pro.

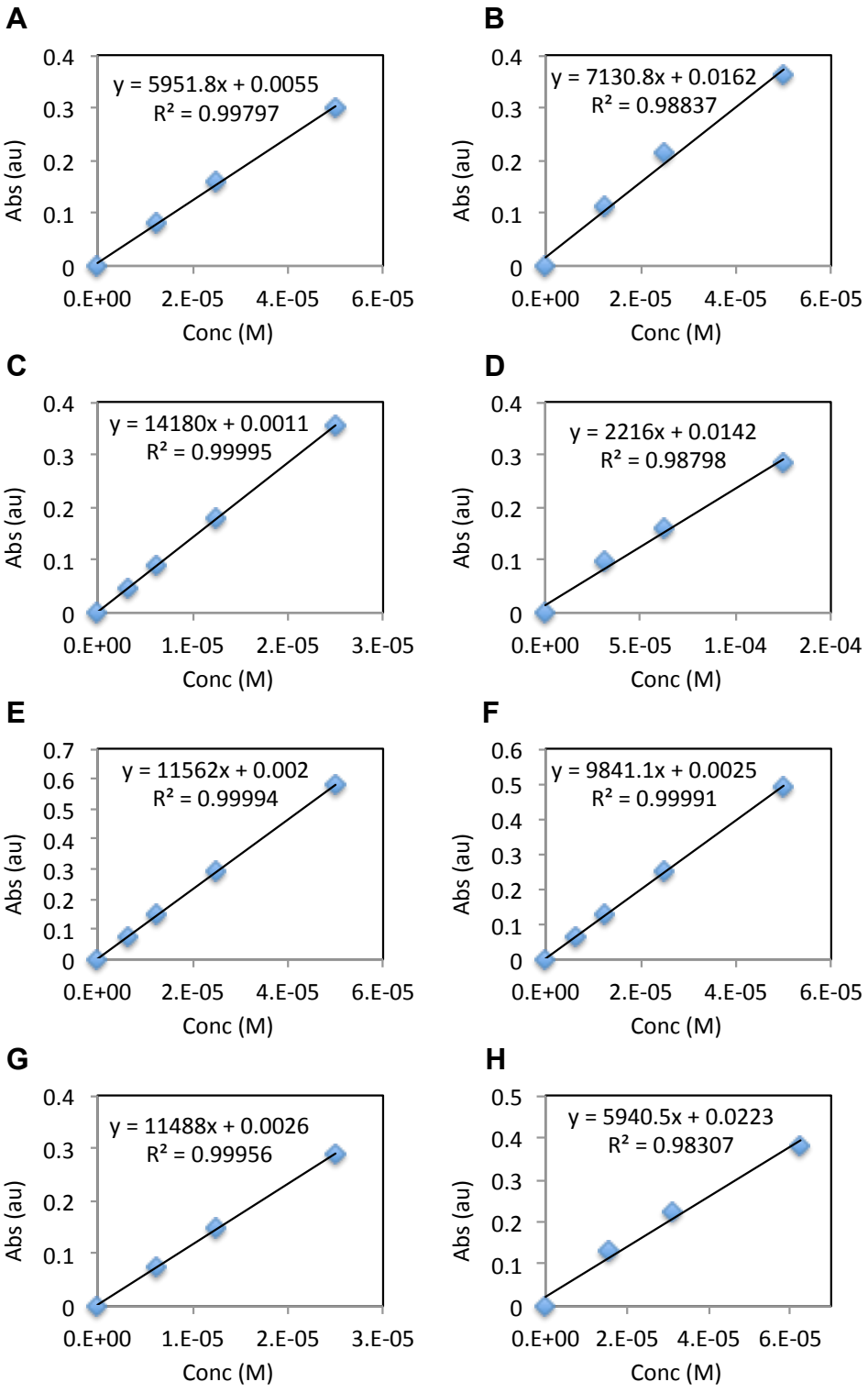

Figure S4.3. Molar extinction plots of free ligand. Data obtainedat 25 °C in aqueous buffer (150 mM NaCl, 20 mM HEPES, pH=7.9). (A) F1et; (B) F2et; (C) F3et; (D) F4et; (E) F1pro; (F) F2pro; (G) F3pro; (H) F4pro.

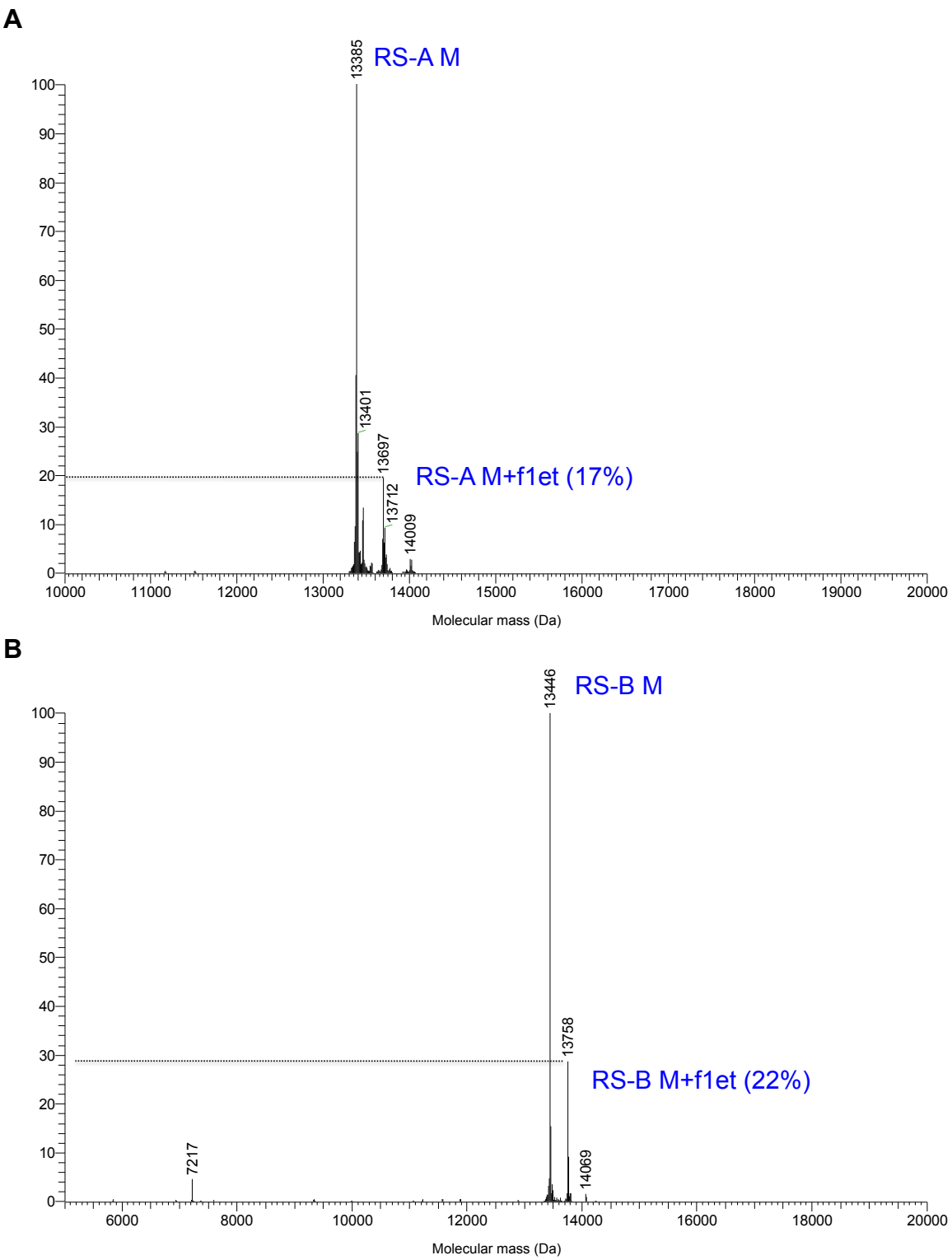

Figure S4.4. Deconvoluted mass spectra of RS conjugation with F1et. Percent labeling efficiency calculated from relative abundances (y-axis) of unbound to bound protein. (A) RS-A; (B) RS-B.

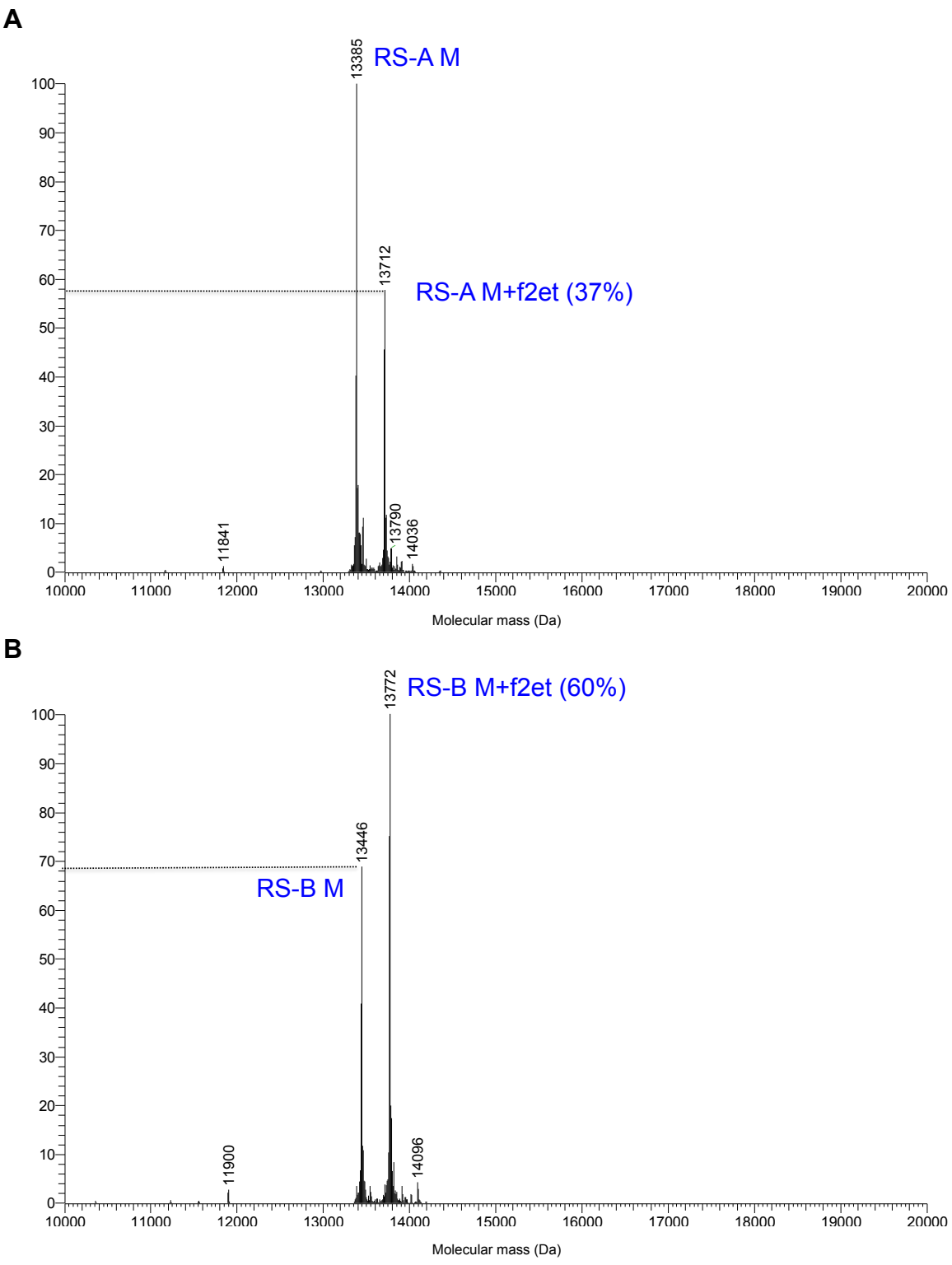

Figure S4.5. Deconvoluted mass spectra of RS conjugation with F2et. Percent labeling efficiency calculated from relative abundances (y-axis) of unbound to bound protein. (A) RS-A; (B) RS-B.

A

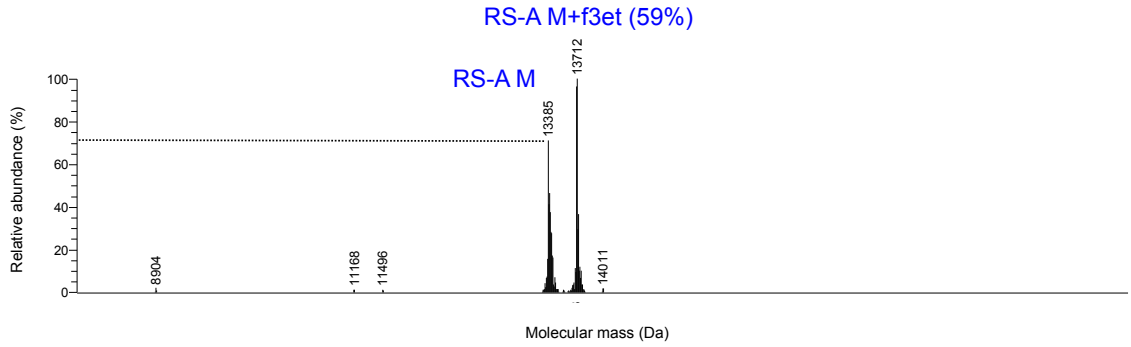

B

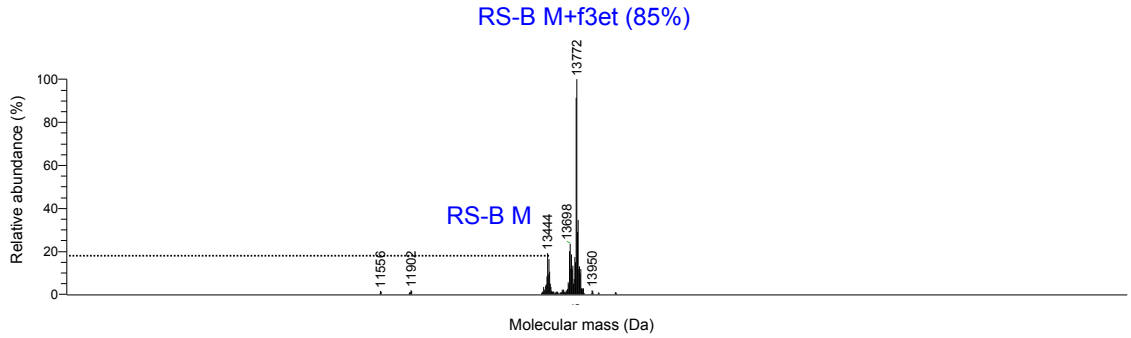

Figure S4.6. Deconvoluted mass spectra of RS conjugation with F3et. Percent labeling efficiency calculated from relative abundances of unbound to bound protein. (A) RS-A; (B) RS-B.

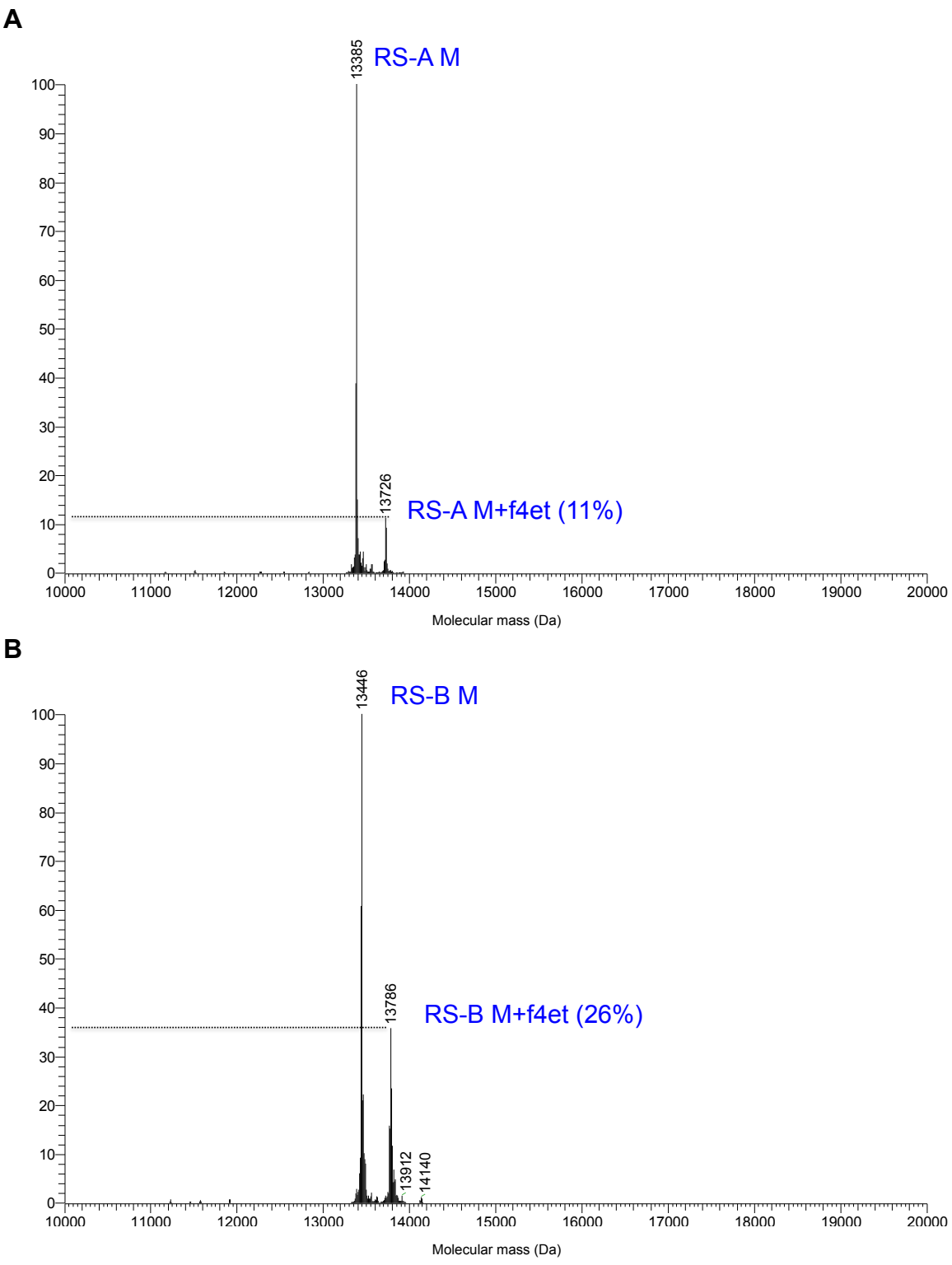

Figure S4.7. Deconvoluted mass spectra of RS conjugation with F4et. Percent labeling efficiency calculated from relative abundances (y-axis) of unbound to bound protein. (A) RS-A; (B) RS-B.

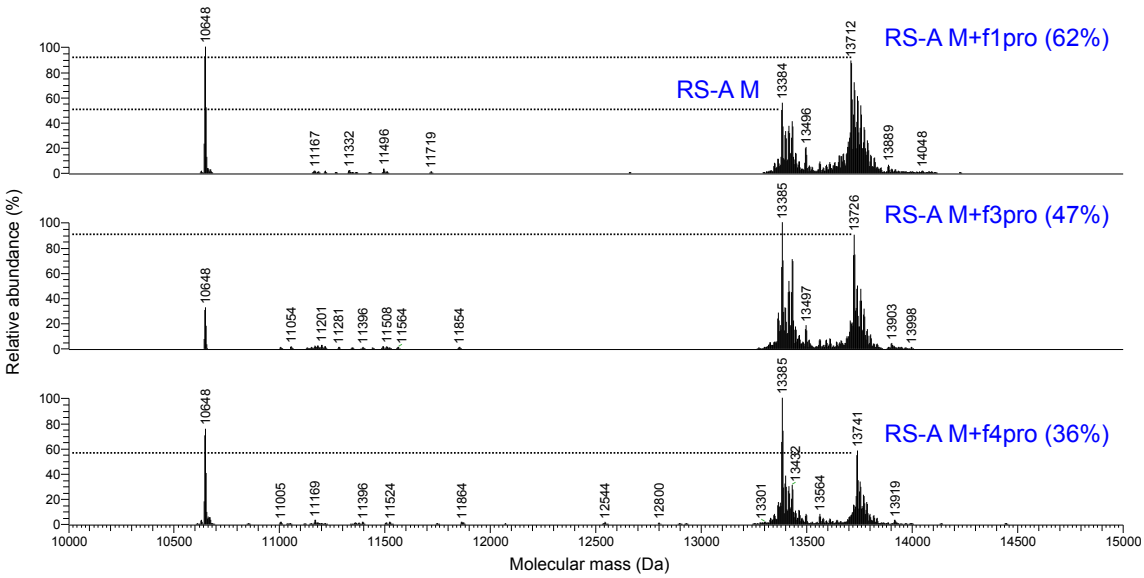

Figure S4.8. Deconvoluted mass spectra of RS-A conjugation with F1pro, F3pro, and F4pro. Percent labeling efficiency calculated from relative abundances of unbound to bound protein.

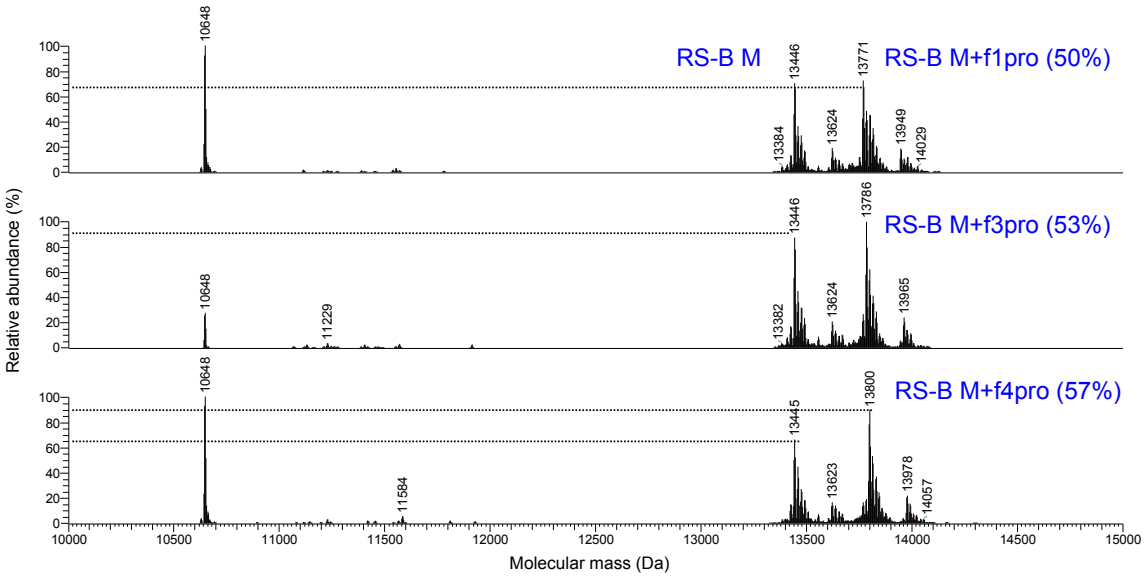

Figure S4.9. Deconvoluted mass spectra of RS-B conjugation with F1pro, F3pro, and F4pro. Percent labeling efficiency calculated from relative abundances of unbound to bound protein.

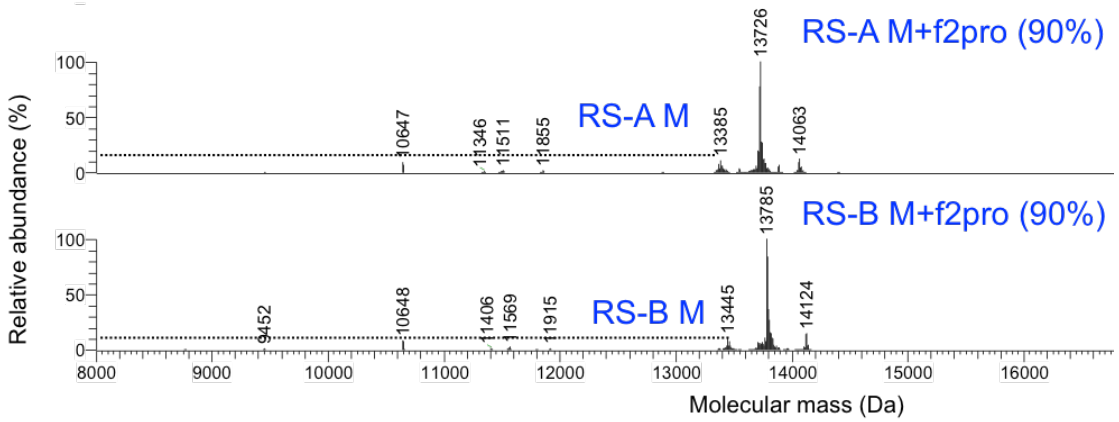

Figure S4.10. Deconvoluted mass spectra of RS conjugation with F2pro. Percent labeling efficiency calculated from relative abundances of unbound to bound protein.

A

RS-A-f2pro Glu-C digest

Sequence[a]	Modifications[b]	Relative Abundance[c]
cLRITD	C1(f2pro)	
EKPNFRTHVVE		
GSSHHHHHHDYDIPTTE		
INGNHVSFD		
INGNHVSFDLFKE		
KPNFRTHVVE		
LGDLKVGD		
LGDLKVGDWVAVE		
LKVGDWVAVE		
LPDHMLD		
LPDHMLDGLE		
NLYFQGHMFTGIVQGTAKLVSIDEKPNFRTHVVE		
RAAKFSDE		
TGASVAHNGccLTVTE	C10(Dehydro); C11(Dehydro)	98
TGASVAHNGccLTVTE	C10(f2pro); C11(f2pro)	2

B

RS-B-f2pro Glu-C digest

Sequence[a]	Modifications[b]	Relative Abundance[c]
cLRITD	C1(f2pro)	
EKPNFRTHVVE		
GSSHHHHHHDYDIPTTE		
INGNHVSFD		
INGNHVSFDLFKE		
KPNFRTHVVE		
LGDLKVGD		
LGDLKVGDWVAVE		
LKVGDWVAVE		
LPDHMLD		
LPDHmLDGLE	M5(Oxidation)	
LPDHMLDGLE		
NLYFQGHmFTGIVQGTAKLVSIDE	M8(Oxidation)	
NLYFQGHMFTGIVQGTAKLVSIDE		
NLYFQGHmFTGIVQGTAKLVSIDEKPNFRTHVVE	M8(Oxidation)	
NLYFQGHMFTGIVQGTAKLVSIDEKPNFRTHVVE		
NLYFQGHMFTGIVQGTAKLVSIDEKPNFRTHVVELP		
DHMLDGLE		
RAAKFSDE		
TGAFVAHNGccLTVTE	C10(Dehydro); C11(Dehydro)	96
TGAFVAHNGccLTVTE	C10(f2pro); C11(f2pro)	4

Figure S4.11. Tandem MS Glu-C digest peptide list for conjugation with F2pro. (A) RS-A-F2pro; (B) RS-B-F2pro. [a]The amino acid sequence of detected peptide. Modified residues are in lower case. [b]The modified residue (single letter code), followed by the position (within the peptide) of the modified residue, followed by the modification type (in parentheses). [c]Relative spectra abundances of C10, C11 dehydro,dehydro (intramolecular disulfide) peptide and F2pro-modified peptide.

References

(1) Germond, A.; Fujita, H.; Ichimura, T.; Watanabe, T. M. Design and Development of Genetically Encoded Fluorescent Sensors to Monitor Intracellular Chemical and Physical Parameters. *Biophys. Rev.* **2016**, *8*, 121–138.

(2) Crivat, G.; Taraska, J. W. Imaging Proteins inside Cells with Fluorescent Tags. *Trends Biotechnol.* **2012**, *30*, 8–16.

(3) Zhang, G.; Zheng, S.; Liu, H.; Chen, P. R. Illuminating Biological Processes through Site-Specific Protein Labeling. *Chem. Soc. Rev.* **2015**, *44*, 3405–3417.

(4) Juillerat, A.; Gronemeyer, T.; Keppler, A.; Gendreizig, S.; Pick, H.; Vogel, H.; Johnsson, K. Directed Evolution of O6 -Alkylguanine-DNA Alkyltransferase for Efficient Labeling of Fusion Proteins with Small Molecules In Vivo. *Chem. Biol.* **2003**, *10*, 313–317.

(5) Gautier, A.; Juillerat, A.; Heinis, C.; Corrêa, I. R.; Kindermann, M.; Beaufils, F.; Johnsson, K. An Engineered Protein Tag for Multiprotein Labeling in Living Cells. *Chem. Biol.* **2008**, *15* (2), 128–136.

(6) Los, G. V.; Encell, L. P.; McDougall, M. G.; Hartzell, D. D.; Karassina, N.; Zimprich, C.; Wood, M. G.; Learish, R.; Ohana, R. F.; Urh, M.; et al. HaloTag: A Novel Protein Labeling Technology for Cell Imaging and Protein Analysis. *ACS Chem. Biol.* **2008**, *3*, 373–382.

(7) Wiedenmann, J.; Oswald, F.; Nienhaus, G. U. Fluorescent Proteins for Live Cell Imaging: Opportunities, Limitations, and Challenges. *IUBMB Life* **2009**, *61*, 1029–1042.

(8) Alexander C. Hoepker, Ariel Wang, Alix Le Marois, Klaus Suhling, Yuling Yan, and G. M. Genetically Encoded Sensors of Protein Hydrodynamics and Molecular Proximity. *Proc. Natl. Acad. Sci.* **2015**, *112*, E2569–E2574.

(9) Fischer, M.; Bacher, A. Biosynthesis of Vitamin B2: Structure and Mechanism of Riboflavin Synthase. *Arch. Biochem. Biophys.* **2008**, *474*, 252–265.

(10) Herrou, J.; Crosson, S. Function, Structure and Mechanism of Bacterial Photosensory LOV Proteins. *Nat. Rev. Microbiol.* **2011**, *9*, 713–723.

(11) Müller, F. The Flavin Redox-System and Its Biological Function. *Top. Curr. Chem.* **1983**, *108*, 71–107.

(12) Mukherjee, A.; Schroeder, C. M. Flavin-Based Fluorescent Proteins: Emerging Paradigms in Biological Imaging. *Curr. Opin. Biotechnol.* **2015**, *31*, 16–23.

(13) Buckley, A. M.; Petersen, J.; Roe, A. J.; Douce, G. R.; Christie, J. M. LOV-Based Reporters for Fluorescence Imaging. *Curr. Opin. Chem. Biol.* **2015**, *27*, 39–45.

(14) Lee, Y. J.; Wu, B.; Raymond, J. E.; Zeng, Y.; Fang, X.; Wooley, K. L.; Liu, W. R. A Genetically Encoded Acrylamide Functionality. *ACS Chem. Biol.* **2013**, *8*, 1664–1670.

(15) Lee, Y. J.; Kurra, Y.; Liu, W. R. Phospha-Michael Addition as a New Click Reaction for Protein Functionalization. *ChemBioChem* **2016**, *17*, 456–461.

(16) Dadová, J.; Orság, P.; Pohl, R.; Brázdová, M.; Fojta, M.; Hocek, M. Vinylsulfonamide and Acrylamide Modification of DNA for Cross-Linking with Proteins. *Angew. Chemie Int. Ed.* **2013**, *52*, 10515–10518.
(17) Naven, R. T.; Kantesaria, S.; Nadanaciva, S.; Schroeter, T.; Leach, K. L. High Throughput Glutathione and Nrf2 Assays to Assess Chemical and Biological Reactivity of Cysteine-Reactive Compounds. *Toxicol Res* **2013**, *2*, 235–244.
(18) Sikorska, E.; Khmelinskii, I. V; Bednarek, A.; Williams, S. L.; Worrall, D. R.; Herance, J. R.; Bourdelande, J. L.; Nowacka, G.; Koput, J.; Sikorski, M. Spectroscopy and Photophysics of 6,8-Dimethylalloxazine. Experimental and Theoretical Study. *J. Fluoresc.* **2004**, *14*, 57–64.
(19) Valeur, B. Effect of Rotational Brownian Motion. In *Molecular Fluorescence Principles and Applications*; Wiley-VCH Verlag GmbH: Weinheim, 2001.
(20) Jameson, D. M. *Introduction to Fluorescence*; Taylor & Francis Group: Boca Raton, 2014.
(21) Stenzel, M. H. Bioconjugation Using Thiols: Old Chemistry Rediscovered to Connect Polymers with Nature's Building Blocks. *ACS Macro Lett.* **2013**, *2*, 14–18.
(22) Pangborn, A. B.; Giardello, M. a.; Grubbs, R. H.; Rosen, R. K.; Timmers, F. J. Safe and Convenient Procedure for Solvent Purification. *Organometallics* **1996**, *15*, 1518–1520.